



QUANTUM NETWORKS WITH SINGLE ATOMS, PHOTONS AND PHONONS

H Kimble
CALIFORNIA INSTITUTE OF TECHNOLOGY

10/04/2016
Final Report

DISTRIBUTION A: Distribution approved for public release.

Air Force Research Laboratory
AF Office Of Scientific Research (AFOSR)/ RTA1
Arlington, Virginia 22203
Air Force Materiel Command

REPORT DOCUMENTATION PAGE		Form Approved OMB No. 0704-0188
<p>The public reporting burden for this collection of information is estimated to average 1 hour per response, including the time for reviewing instructions, searching existing data sources, gathering and maintaining the data needed, and completing and reviewing the collection of information. Send comments regarding this burden estimate or any other aspect of this collection of information, including suggestions for reducing the burden, to Department of Defense, Executive Services, Directorate (0704-0188). Respondents should be aware that notwithstanding any other provision of law, no person shall be subject to any penalty for failing to comply with a collection of information if it does not display a currently valid OMB control number.</p> <p>PLEASE DO NOT RETURN YOUR FORM TO THE ABOVE ORGANIZATION.</p>		
1. REPORT DATE (DD-MM-YYYY) 12-04-2017	2. REPORT TYPE Final Performance	3. DATES COVERED (From - To) 01 May 2010 to 30 Jun 2016
4. TITLE AND SUBTITLE QUANTUM NETWORKS WITH SINGLE ATOMS, PHOTONS AND PHONONS		5a. CONTRACT NUMBER 5b. GRANT NUMBER FA9550-10-1-0197 5c. PROGRAM ELEMENT NUMBER 61102F
6. AUTHOR(S) H Kimble		5d. PROJECT NUMBER 5e. TASK NUMBER 5f. WORK UNIT NUMBER
7. PERFORMING ORGANIZATION NAME(S) AND ADDRESS(ES) CALIFORNIA INSTITUTE OF TECHNOLOGY 1200 E. CALIFORNIA BLVD PASADENA, CA 91125 US		8. PERFORMING ORGANIZATION REPORT NUMBER
9. SPONSORING/MONITORING AGENCY NAME(S) AND ADDRESS(ES) AF Office of Scientific Research 875 N. Randolph St. Room 3112 Arlington, VA 22203		10. SPONSOR/MONITOR'S ACRONYM(S) AFRL/AFOSR RTA1 11. SPONSOR/MONITOR'S REPORT NUMBER(S) AFRL-AFOSR-VA-TR-2017-0081
12. DISTRIBUTION/AVAILABILITY STATEMENT A DISTRIBUTION UNLIMITED: PB Public Release		
13. SUPPLEMENTARY NOTES		
<p>14. ABSTRACT</p> <p>The NSSEFF research program has been directed to create new paradigms for the strong interaction of light and matter. In general terms, the research has laid foundations for building complex quantum systems from 'simple' components of single atoms and photons. Theoretical investigations have predicted surprising quantum phenomena that have not heretofore existed in Nature. More specifically, the research investigated new quantum phases of matter with photon-mediated atom-atom interactions in one and two-dimensional nano-photonics lattices (e.g., self-organization of free-space atoms into crystals bound by light). In a complimentary fashion, exotic quantum phases for photons become possible by way of strong photon-photon interactions created by an underlying lattice of atoms (e.g., two propagating photons bonded to become a 'molecule').</p> <p>In terms of methodology, the NSSEFF research required an interdisciplinary 'toolkit' from atomic physics, quantum optics, and nano-photonics for the control, manipulation, and interaction of atoms and photons with a complexity and scalability well beyond the prior state-of-the-art. The NSSEFF research achieved important goals toward such integration across disciplines and utilized these tools to investigate novel phenomena in the physics of light-matter interactions.</p> <p>More specifically, with NSSEFF support, a technical infrastructure was created for 1) the advancement of the frontier for the design, fabrication, and characterization of new generations of 1D and 2D photonic crystals in low-loss dielectrics, and 2) the integration of these devices into the realm of ultra-cold atomic physics to produce nano-scopic lattices of trapped atoms that are strongly coupled to single photons within the photonic crystals.</p> <p>For operation in the dispersive regime of a one-dimensional photonic crystal waveguide (PCW), observations of cooperative atomic emis</p>		

15. SUBJECT TERMS
PHOTONS, ATOMS

16. SECURITY CLASSIFICATION OF: a. REPORT			17. LIMITATION OF ABSTRACT	18. NUMBER OF PAGES	19a. NAME OF RESPONSIBLE PERSON
Unclassified	b. ABSTRACT	c. THIS PAGE	UU		LAWAL, RAHEEM
					19b. TELEPHONE NUMBER (Include area code) 703-696-7313

QUANTUM NETWORKS WITH SINGLE ATOMS, PHOTONS AND PHONONS

National Security Science and Engineering Fellowship (NSSEFF) H. J. Kimble

NSSEFF Publications

1 May 2010 to 30 June 2016

[1.] A. Asenjo-Garcia, J. D. Hood, D. E. Chang, and H. J. Kimble, "Atom-Light Interactions in Quasi-1D Nanostructures: A Green's Function Perspective," *New J. Phys.* (in review, June 2016); available at <http://arxiv.org/abs/1606.04977>.

[2.] C.-L. Hung, A. González-Tudela, J. I. Cirac, and H. J. Kimble, "Quantum Spin Dynamics with Pairwise-Tunable, Long-Range Interactions," *PNAS* 2016 **113** (34) E4946-E4955; published ahead of print August 5, 2016; available at doi:10.1073/pnas.1603777113.

[3.] J. D. Hood, A. Goban, A. Asenjo-Garcia, M. Lu, S.-P. Yu, D. E. Chang, and H. J. Kimble, "Atom-atom interactions around the band edge of a photonic crystal waveguide," *PNAS* 2016 113 (38); published ahead of print August 31, 2016; available at doi:10.1073/pnas.1603788113.

Atom-light interactions in quasi-1D nanostructures: a Green's function perspective

A. Asenjo-Garcia^{1,2}‡, J. D. Hood^{1,2}‡, D. E. Chang³, and H. J. Kimble^{1,2}

¹ Norman Bridge Laboratory of Physics MC12-33

² Institute for Quantum Information and Matter, California Institute of Technology,
Pasadena, CA 91125, USA

³ ICFO-Institut de Ciencies Fotoniques, The Barcelona Institute of Science and
Technology, 08860 Castelldefels (Barcelona), Spain

E-mail: ana.asenjo@caltech.edu

17 June 2016

Abstract. Based on a formalism that describes atom-light interactions in terms of the classical electromagnetic Green's function, we study the optical response of atoms and other quantum emitters coupled to one-dimensional photonic structures, such as cavities, waveguides, and photonic crystals. We demonstrate a clear mapping between the transmission spectra and the local Green's function that allows to identify signatures of dispersive and dissipative interactions between atoms, gaining insight into recent experiments.

PACS numbers: 42.50.Ct, 42.50.Nn

Keywords: Quantum optics, nanophotonics, waveguide QED.

1. Introduction

As already noticed by Purcell in the first half of the past century, the decay rate of an atom can be either diminished or enhanced by tailoring its dielectric environment [1–3]. Likewise, by placing more than one atom in the vicinity of photonic nanostructures, one can curtail or accelerate their collective decay. In addition to modifying the radiative decay, nanophotonic structures can be employed to spatially and spectrally engineer atom-light interactions, thus obtaining fundamentally different atom dynamics to those observed in free-space [4].

In the past decade, atoms and other quantum emitters have been interfaced with the electromagnetic fields of a plethora of quasi-1D nanostructured reservoirs, ranging from high-quality optical [5–10] and microwave [11, 12] cavities to dielectric [13–18], metallic

‡ These authors contributed equally to this research.

[19–22], and superconducting [23, 24] waveguides. Photonic crystal waveguides, periodic dielectric structures that display a bandgap where light propagation is forbidden [25, 26], have been proposed as promising candidates to study long- and tunable-range coherent interactions between quantum emitters [27–30]. Due to the different character of the guided modes at various frequencies within the band structure of the photonic crystal, the interaction of the quantum emitters with the nanostructure can be remarkably distinct depending on the emitter resonance frequency. Far away from the bandgap, where light propagates, the guided modes resemble those of a conventional waveguide. Close to the bandgap, but still in the propagating region, the fields are similar to those of a quasi-1D cavity, whereas inside the bandgap the fields become evanescent, decaying exponentially.

All these regimes have been recently explored in the lab, where atoms [31–33] and quantum dots [4, 34, 35] have been interfaced with photonic crystal waveguides. Most of these experiments have been performed in conditions where the resonance frequency of the emitter lies outside the bandgap. However, very recently, the first experiments of atoms [36] and superconducting qubits [37] interacting with evanescent modes in the bandgap of photonic crystal waveguides have been reported.

Within this context, it has become a necessity to understand the rich spectral signatures of atom-like emitters interacting through the guided modes of quasi one-dimensional nanophotonic structures within a unified framework that extends beyond those of cavity [38] or waveguide QED [39]. In this work, we employ a formalism based on the classical electromagnetic Green's function [40–44] to characterize the response of atoms that interact by emitting and absorbing photons through the guided mode of the nanostructure. Since the fields in the vicinity of the structure might have complex spatial and polarization patterns, the full Green's function is only known analytically for a handful of systems (such as planar multilayer stacks [45], infinite nanofibers [46, 47], and a few more [42]) and beyond that one has to resort to numerical solvers of Maxwell's equations. However, in quasi-1D nanostructures, one can isolate the most relevant guided mode and build a simple prescription for the 1D Green's function that accounts for the behavior of this mode, greatly simplifying the problem.

In the first part of the article, we summarize the procedure to obtain an effective atom-atom Hamiltonian, in which the guided-mode fields are effectively eliminated and the atom interactions are written in terms of Green's functions [40–42]. We then apply this formalism to a collection of atoms in different quasi one-dimensional dielectric environments, and analyze the atomic transmission and reflection spectra in terms of the eigenvalues of the matrix consisting of the Green's functions between every pair of atoms. We show that, in the linear (low-saturation) regime, asymmetry in the transmission spectra and frequency shifts are signatures of coherent atom-light interactions, whereas symmetric lineshapes reveal dissipation. Finally, based on the rapid technical advances in fabrication of both photonic and microwave structures, we project observable signatures that can be made in the next generation of experiments of atoms and superconducting qubits interacting in the bandgap of photonic crystal

waveguides.

2. Atom-light interactions in terms of Green's functions

Much effort has gone into developing a quantum formalism to describe atoms coupled to radiation. A conventional technique is to express the field in terms of a set of eigenmodes of the system, with corresponding creation and annihilation operators a^\dagger and a [39]. This canonical quantization technique is well suited for approximately closed systems such as high-Q cavities and homogeneous structures such as waveguides, both of which have simple eigenmode decompositions. However, the application of this quantization scheme to more involved nanostructures is not straight forward. Further, the formalism is not suited for dispersive and absorbing media as the commutation relations for the field operators are not conserved [48].

Instead, here we describe atom-light interactions using a quantization scheme based on the classical electromagnetic Green's function, valid for any medium characterized by a linear and isotropic dielectric function $\epsilon(\mathbf{r}, \omega)$, closely following the work of Welsch and colleagues [40–42, 44]. In the following, we employ this formalism to derive an atom-atom Hamiltonian in which the field is effectively eliminated, yielding an expression that only depends on atomic operators. Moreover, once the dynamics of the atoms is solved, the electric field at every point along the quasi one-dimensional structure can be recovered through an expression that relates the field to the atomic operators.

Classically, the field $\mathbf{E}(\mathbf{r}, \omega)$ at a point \mathbf{r} due to a source current $\mathbf{j}(\mathbf{r}', \omega)$ at \mathbf{r}' is obtained by means of the propagator of the electromagnetic field, the dyadic Green's function (or Green's tensor), as $\mathbf{E}(\mathbf{r}, \omega) = i\mu_0\omega \int d\mathbf{r}' \mathbf{G}(\mathbf{r}, \mathbf{r}', \omega) \cdot \mathbf{j}(\mathbf{r}', \omega)$. In particular, for a dipole source \mathbf{p} located at \mathbf{r}_0 , the current is $\mathbf{j}(\mathbf{r}, \omega) = -i\omega\mathbf{p}\delta(\mathbf{r} - \mathbf{r}_0)$, and the field reads $\mathbf{E}(\mathbf{r}, \omega) = \mu_0\omega^2 \mathbf{G}(\mathbf{r}, \mathbf{r}_0, \omega) \cdot \mathbf{p}$. The tensorial structure of the Green's function accounts for the vectorial nature of the electromagnetic field, as a dipole directed along the \hat{x} -direction can create a field polarized not only along \hat{x} , but also along \hat{y} and \hat{z} §.

The Green's function $\mathbf{G}(\mathbf{r}, \mathbf{r}', \omega)$ is the fundamental solution of the electromagnetic wave equation, and obeys [49]:

$$\nabla \times \nabla \times \mathbf{G}(\mathbf{r}, \mathbf{r}', \omega) - \frac{\omega^2}{c^2} \epsilon(\mathbf{r}, \omega) \mathbf{G}(\mathbf{r}, \mathbf{r}', \omega) = \delta(\mathbf{r} - \mathbf{r}') \mathbb{1}, \quad (1)$$

where $\epsilon(\mathbf{r}, \omega)$ is the medium relative permittivity. For a scalar permittivity, Lorentz reciprocity holds and, then, $\mathbf{G}^T(\mathbf{r}, \mathbf{r}', \omega) = \mathbf{G}(\mathbf{r}', \mathbf{r}, \omega)$, where T stands for transpose (and operates on the polarization indexes). In analogy to its classical counterpart, the electric field operator can be written in terms of bosonic annihilation (creation) operators $\hat{\mathbf{f}}$ ($\hat{\mathbf{f}}^\dagger$) as [40]

$$\begin{aligned} \hat{\mathbf{E}}(\mathbf{r}, \omega) &= i\mu_0\omega^2 \sqrt{\frac{\hbar\epsilon_0}{\pi}} \int d\mathbf{r}' \sqrt{\text{Im}\{\epsilon(\mathbf{r}', \omega)\}} \mathbf{G}(\mathbf{r}, \mathbf{r}', \omega) \cdot \hat{\mathbf{f}}(\mathbf{r}', \omega) + \text{h.c.} \\ &= \hat{\mathbf{E}}^+(\mathbf{r}, \omega) + \hat{\mathbf{E}}^-(\mathbf{r}, \omega), \end{aligned} \quad (2)$$

§ Throughout this manuscript, the Green's tensor will be also denoted as Green's function.

where $\hat{\mathbf{E}}^{+(-)}(\mathbf{r}, \omega)$ is the positive (negative) frequency component of the field operator, and h.c. stands for Hermitian conjugate. Within this quantization framework, $\hat{\mathbf{f}}(\mathbf{r}, \omega)$ is associated with the degrees of freedom of local material polarization noise, which accompanies the material dissipation $\text{Im}\{\epsilon(\mathbf{r}, \omega)\}$ as required by the fluctuation-dissipation theorem [44]. This expression guarantees the fulfillment of the canonical field commutation relations, even in the presence of material loss. The appearance of the Green's function reveals that the *quantumness* of the system is encoded in either the correlations of the noise operators $\hat{\mathbf{f}}$ or in any other quantum sources (such as atoms), but the field propagation obeys the wave equation and as such the spatial profile of the photons is determined by the classical propagator.

We now want to investigate the evolution of N identical two-level atoms of resonance frequency ω_A that interact through a guided mode probe field of frequency ω_p . Within the Born-Markov approximation, we trace out the photonic degrees of freedom, obtaining an effective atom-atom Hamiltonian [41, 50, 51]. This approximation is valid when the atomic correlations decay much slower than the photon bath correlations, or, in other words, when the Green's function is characterized by a broad spectrum, which can be considered to be flat over the atomic linewidth. Then, the atomic density matrix $\hat{\rho}_A$ evolves according to $\dot{\hat{\rho}}_A = -(i/\hbar)[\mathcal{H}, \hat{\rho}_A] + \mathcal{L}[\hat{\rho}_A]$ [38]. Within the rotating wave approximation, and in the frame rotating with the probe field frequency, the Hamiltonian and Lindblad operators read

$$\mathcal{H} = -\hbar\Delta_A \sum_{i=1}^N \hat{\sigma}_{ee}^i - \hbar \sum_{i,j=1}^N J^{ij} \hat{\sigma}_{eg}^i \hat{\sigma}_{ge}^j - \sum_{i=1}^N \left(\mathbf{d} \cdot \hat{\mathbf{E}}_p^-(\mathbf{r}_i) \hat{\sigma}_{ge}^i + \mathbf{d}^* \cdot \hat{\mathbf{E}}_p^+(\mathbf{r}_i) \hat{\sigma}_{eg}^i \right), \quad (3a)$$

$$\mathcal{L}[\hat{\rho}_A] = \sum_{i,j=1}^N \frac{\Gamma^{ij}}{2} \left(2\hat{\sigma}_{ge}^i \hat{\rho}_A \hat{\sigma}_{eg}^j - \hat{\sigma}_{eg}^i \hat{\sigma}_{ge}^j \hat{\rho}_A - \hat{\rho}_A \hat{\sigma}_{eg}^i \hat{\sigma}_{ge}^j \right), \quad (3b)$$

where $\hat{\mathbf{E}}_p$ is the guided mode probe field, and $\Delta_A = \omega_p - \omega_A$ is the detuning between the guided mode probe field and the atom. The dipole moment operator is expressed in terms of the dipole matrix elements as $\hat{\mathbf{p}}_j = \mathbf{d}^* \hat{\sigma}_{eg}^j + \mathbf{d} \hat{\sigma}_{ge}^j$, where $\hat{\sigma}_{eg}^j = |e\rangle \langle g|$ is the atomic coherence operator between the ground and excited states of atom j , and $\mathbf{d} = \langle g | \hat{\mathbf{d}} | e \rangle$ is the dipole matrix element associated with that transition. The spin-exchange and decay rates are

$$J^{ij} = (\mu_0 \omega_p^2 / \hbar) \mathbf{d}^* \cdot \text{Re} \mathbf{G}(\mathbf{r}_i, \mathbf{r}_j, \omega_p) \cdot \mathbf{d}, \quad (4a)$$

$$\Gamma^{ij} = (2\mu_0 \omega_p^2 / \hbar) \mathbf{d}^* \cdot \text{Im} \mathbf{G}(\mathbf{r}_i, \mathbf{r}_j, \omega_p) \cdot \mathbf{d}. \quad (4b)$$

Note that the dispersive and dissipative atom-atom couplings are given in terms of the total Green's function of the medium. For a quasi-1D nanostructure, the Green's function can be expressed as $\mathbf{G}(\mathbf{r}_i, \mathbf{r}_j, \omega_p) = \mathbf{G}_{1D}(\mathbf{r}_i, \mathbf{r}_j, \omega_p) + \mathbf{G}'(\mathbf{r}_i, \mathbf{r}_j, \omega_p)$, where the first term corresponds to the guided mode that propagates along the structure mediating atom-atom interactions, and the second term accounts for all other field modes (e.g., emission into free space).

Due to the fast spatial decay of the non-guided Green's function, the interaction mediated by $\mathbf{G}'(\mathbf{r}_i, \mathbf{r}_j, \omega_p)$ is not collective in the low-density limit (i.e. when the atoms are far away from each other). We can then write $J^{ij} = J_{1D}^{ij} + J'\delta_{ij}$ and $\Gamma^{ij} = \Gamma_{1D}^{ij} + \Gamma'\delta_{ij}$, where δ_{ij} is the Kronecker delta. In particular, in free-space, Γ' is simply $\Gamma_0 = (2\mu_0\omega_p^2/\hbar)\mathbf{d}^* \cdot \text{Im } \mathbf{G}_0(\mathbf{r}_i, \mathbf{r}_i, \omega_p) \cdot \mathbf{d} = \omega_p^3|\mathbf{d}|^2/3\pi\hbar\epsilon_0c^3$, where \mathbf{G}_0 is the vacuum's Green's function [i.e. the solution to Eq. (1) when $\epsilon(\mathbf{r}, \omega) = 1$]. Depending on the geometry and dielectric response of the nanostructure, and on the atom position, Γ' can be larger or smaller than Γ_0 . J' accounts for frequency shifts due to other guided and non-guided modes, and is in general spatially dependent. In fact, the value of J' is dependent upon particular details of atom trapping and geometry of the nanostructure. We will for simplicity consider J' identical for every atom and assume that this constant value has been incorporated into the definition of ω_A .

Once the dynamics of the atomic coherences are solved for, one can reconstruct the field at any point in space. Generalizing Eq. (6.16) of Ref. [41] for more than a single atom, the evolution of the bosonic field operator is given by

$$\dot{\hat{\mathbf{f}}}(\mathbf{r}, \omega) = -i\omega\hat{\mathbf{f}}(\mathbf{r}, \omega) + \frac{\omega^2}{c^2}\sqrt{\frac{1}{\pi\hbar\epsilon_0}\text{Im}\{\epsilon(\mathbf{r}, \omega)\}}\sum_{j=1}^N \mathbf{G}^*(\mathbf{r}, \mathbf{r}_j, \omega) \cdot \mathbf{d} \hat{\sigma}_{ge}^j, \quad (5)$$

where the atoms act as sources for the bosonic fields. We can formally integrate this expression and plug it into the equation for the field [Eq. (2)]. After some algebra, and performing Markov's approximation, we arrive at the final expression for the field operator, which is simply

$$\hat{\mathbf{E}}^+(\mathbf{r}) = \hat{\mathbf{E}}_p^+(\mathbf{r}) + \mu_0\omega_p^2\sum_{j=1}^N \mathbf{G}(\mathbf{r}, \mathbf{r}_j, \omega_p) \cdot \mathbf{d} \hat{\sigma}_{ge}^j. \quad (6)$$

This expression can be understood as a generalized input-output equation, where the total guided mode field is the sum of the probe, i.e. free, field $\hat{\mathbf{E}}_p^+(\mathbf{r})$ and the field re-scattered by the atoms. The quantum nature of these equations has been treated before when deriving a generalized input-output formalism for unstructured waveguides [52,53].

3. Transmission and reflection in quasi-1D systems

3.1. Atomic coherences in the low saturation regime

We now explore the behavior of the atoms under a coherent, continuous-wave probe field. In the single-excitation manifold and low saturation (linear) regime ($\langle\hat{\sigma}_{ee}\rangle = 0$), the atoms behave as classical dipoles. Then, the Heisenberg equations for the expectation value of the atomic coherences ($\langle\hat{\sigma}_{eg}\rangle = \sigma_{eg}$) are linear on the atomic operators, and read

$$\dot{\sigma}_{ge}^i = i\left(\Delta_A + i\frac{\Gamma'}{2}\right)\sigma_{ge}^i + i\Omega_i + i\sum_{j=1}^N g_{ij}\sigma_{ge}^j, \quad (7)$$

where $\Omega_i = \mathbf{d}^* \cdot \mathbf{E}_p^+(\mathbf{r}_i)/\hbar$ is the guided mode Rabi frequency (with $\mathbf{E}_p = \langle\hat{\mathbf{E}}_p\rangle$), and

$$g_{ij} = J_{1D}^{ij} + i\Gamma_{1D}^{ij}/2 = (\mu_0\omega_p^2/\hbar)\mathbf{d}^* \cdot \mathbf{G}_{1D}(\mathbf{r}_i, \mathbf{r}_j, \omega_p) \cdot \mathbf{d}$$

DISTRIBUTION A: Distribution approved for public release.

depends only on the Green's function of the guided mode. For long times, the coherences will damp out to a steady state ($\dot{\sigma}_{ge}^i = 0$). The solution for the atomic coherences is then

$$\vec{\sigma}_{ge} = -\mathcal{M}^{-1}\Omega \text{ with } \mathcal{M} = (\Delta_A + i\Gamma'/2)\mathbb{1} + \mathbf{g}. \quad (8)$$

In the above equation, $\vec{\sigma}_{ge} = (\sigma_{ge}^1, \dots, \sigma_{ge}^N)$ and $\Omega = (\Omega_1, \dots, \Omega_N)$ are vectors of N components, and \mathcal{M} is a $N \times N$ matrix that includes the dipole-projected matrix \mathbf{g} of elements g_{ij} . Significantly, the matrix is not Hermitian, as there is radiation loss. However, due to reciprocity, the Green's function matrix is complex symmetric [$\mathbf{G}^T(\mathbf{r}, \mathbf{r}', \omega) = \mathbf{G}(\mathbf{r}', \mathbf{r}, \omega)$], and \mathbf{g} inherits this property if the dipole matrix elements are real, which will be a condition enforced from now on. Complex symmetric matrices can be diagonalized, $\mathbf{g}\mathbf{v}_\xi = \lambda_\xi \mathbf{v}_\xi$ with $\xi = 1 \dots N$, where λ_ξ and \mathbf{v}_ξ are the eigenvalues and eigenvectors of \mathbf{g} , respectively. Since the first term of \mathcal{M} is proportional to the identity, \mathcal{M} and \mathbf{g} share the same set of eigenvectors.

The eigenmodes represent the spatial profile of the collective atomic excitation, i.e., the dipole amplitude and phase at each atom. However, as the matrix \mathbf{g} is non-Hermitian, the eigenmodes are not orthonormal in the regular sense, but instead follow different orthogonality and completeness prescriptions, namely $\mathbf{v}_\xi^T \cdot \mathbf{v}_{\xi'} = \delta_{\xi, \xi'}$ and $\sum_{\xi=1}^N \mathbf{v}_\xi \otimes \mathbf{v}_\xi^T = \mathbb{1}$, where T indicates transpose instead of the customary conjugate transpose [54]. After inserting the completeness relation into Eq. (8), we find that the expected value of the atomic coherences in the steady state in terms of the eigenvalues and eigenvectors of the quasi-1D Green's function is

$$\vec{\sigma}_{ge} = - \sum_{\xi \in \text{mode}} \frac{(\mathbf{v}_\xi^T \cdot \Omega)}{(\Delta_A + J_{\xi,1D}) + i(\Gamma' + \Gamma_{\xi,1D})/2} \mathbf{v}_\xi, \quad (9)$$

where $J_{\xi,1D} = \text{Re } \lambda_\xi$ and $\Gamma_{\xi,1D} = 2 \text{Im } \lambda_\xi$ are the frequency shifts and decay rates corresponding to mode ξ , and the sum is performed over mode number from 1 to N . The scalar product in the numerator $\mathbf{v}_\xi^T \cdot \vec{\Omega} = \sum_{j=1}^N v_{\xi,j} \Omega_j$ describes the coupling between the probe field and a particular collective atomic mode.

Therefore, the dynamics of the atoms can be understood in terms of the eigenmodes of \mathbf{g} , where the real and imaginary parts of the eigenvalues correspond to cooperative frequency shifts and decay rates of the collective atomic modes $\{\xi\}$. As the modes are non-normal, the observables cannot be expressed as the sum over all different mode contributions but, instead, any measurable quantity will show signatures of interference between different modes. Although it could be considered a mathematical detail, the fact that the modes of a system are non-normal has deep physical consequences. For instance, non-normal dynamics is responsible of phenomena as different as the Petermann excess-noise factor observed in lasers [55–57] or the transient growth of the shaking of a building after an earthquake [58].

3.2. Transmission and reflection coefficients

Having previously calculated the linear response of an ensemble of atoms to an input field, we now relate the response to observable outputs, i.e. the reflected and transmitted fields. One can calculate the total field from Eq. (6), by substituting in the solution of Eq. (9) for the atomic coherences σ_{ge} . For the sake of simplicity, we now assume that the atomic chain and the main axis of the nanostructure are oriented along \hat{x} , and the atoms have all the same radial position and thus the same 'transversal' coupling into the nanostructure. The field is considered to be polarized along \hat{y} , and reads

$$E^+(x) \equiv E_y^+(x) = E_p^+(x) - \sum_{\xi=1}^N \frac{(\mathbf{g}^T(x) \cdot \mathbf{v}_\xi) (\mathbf{v}_\xi^T \cdot \mathbf{E}_p^+)}{(\Delta_A + J_{\xi,1D}) + i(\Gamma' + \Gamma_{\xi,1D})/2}, \quad (10)$$

where the j -component of vector $\mathbf{g}(x)$ is $g_j(x) = g(x, x_j) = (\mu_0 \omega_p d^2 / \hbar) G_{1D,yy}(x, x_j, \omega_p)$, and $\mathbf{g}^T(x) \cdot \mathbf{v}_\xi = \sum_{i=j}^N g_j(x) v_{\xi,j}$ represents how much the mode ξ contributes to the field emitted by the atoms. Note that now the electric field vector \mathbf{E}_p^+ in Eq. (10) no longer represents different polarization components, but a single polarization at different atom positions.

In order to connect the above expression to the transmission and reflection coefficients, we evaluate the field $E^+(x)$ at the positions $x = x_{\text{right}}$ and $x = x_{\text{left}}$, which are considered to be immediately outside the atomic chain. The details of the derivation are provided in Appendix A. The normalized transmission and reflection coefficients are

$$t(\Delta_A)/t_0(\Delta_A) = 1 - \frac{1}{g(x_{\text{right}}, x_{\text{left}})} \sum_{\xi=1}^N \frac{(\mathbf{g}^T(x_{\text{right}}) \cdot \mathbf{v}_\xi) (\mathbf{v}_\xi^T \cdot \mathbf{g}(x_{\text{left}}))}{(\Delta_A + J_{\xi,1D}) + i(\Gamma' + \Gamma_{\xi,1D})/2}, \quad (11a)$$

$$r(\Delta_A) = r_0(\Delta_A) - \frac{1}{g(x_{\text{left}}, x_{\text{left}})} \sum_{\xi=1}^N \frac{(\mathbf{g}^T(x_{\text{left}}) \cdot \mathbf{v}_\xi) (\mathbf{v}_\xi^T \cdot \mathbf{g}(x_{\text{left}}))}{(\Delta_A + J_{\xi,1D}) + i(\Gamma' + \Gamma_{\xi,1D})/2}, \quad (11b)$$

where $t_0(\Delta_A)$ and $r_0(\Delta_A)$ are the transmission and reflection coefficients for the 1D photonic structure when no atoms are present. One can further simplify the expression for the transmission so that the resulting equation only depends on the eigenvalues, and not the eigenfunctions, of the Green's function matrix \mathbf{g} (as shown in Appendix B). Then,

$$t(\Delta_A)/t_0(\Delta_A) = \prod_{\xi=1}^N \frac{\Delta_A + i\Gamma'/2}{(\Delta_A + J_{\xi,1D}) + i(\Gamma' + \Gamma_{\xi,1D})/2} \equiv \prod_{\xi=1}^N t_\xi(\Delta_A). \quad (12)$$

The total transmission coefficient can thus be written as the product of the transmission coefficients of each of the collective atomic modes. Noticeably, when looking at the transmission spectrum of atoms that interact through the guided mode of a quasi-1D nanostructure, there is a redundancy between the eigenfunctions and eigenvalues, and one is able to obtain an expression that does not depend on the former (i.e. all the relevant information about the geometry is contained in the collective frequency shifts

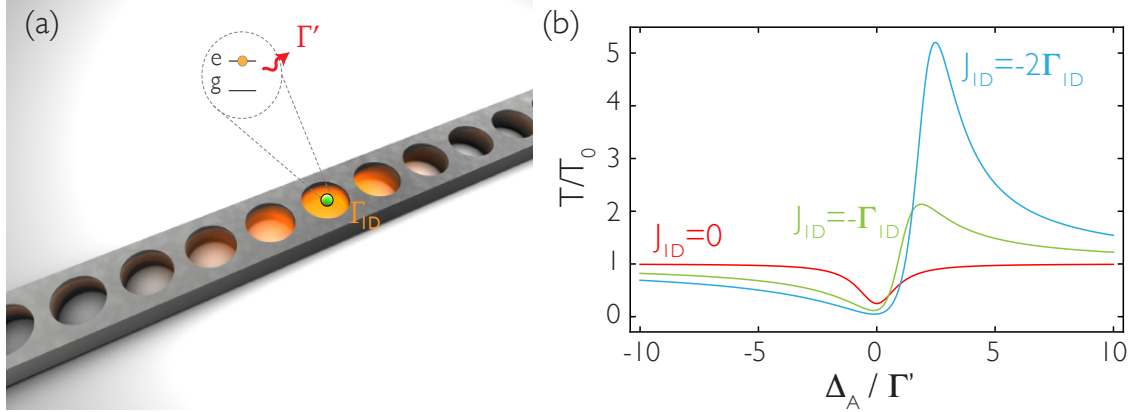


Figure 1. (a) Sketch of an atom interacting with the guided mode of a structured 1D nanostructure. The single-atom decay rate is Γ_{1D} , and the decay into non-guided modes is characterized by Γ' . (b) Normalized transmission spectra ($|t/t_0|^2$) for a single atom for different values of the ratio between the real and imaginary parts of the guided mode Green's function, following Eq. (13). The decay rate into the guided modes is taken to be $\Gamma_{1D} = \Gamma'$ for all cases.

and decay rates). In particular, for a single atom located at x_j with $J_{1D}^{jj} \equiv J_{1D}$ and $\Gamma_{1D}^{jj} \equiv \Gamma_{1D}$, the eigenvalues are directly proportional to the local Green's function, and

$$t(\Delta_A)/t_0(\Delta_A) = \frac{\Delta_A + i\Gamma'/2}{(\Delta_A + J_{1D}) + i(\Gamma' + \Gamma_{1D})/2}. \quad (13)$$

The transmittance $T = |t|^2$ can be recast into a Fano-like lineshape [59] as

$$T/T_0 = \frac{(q + \chi)^2}{1 + \chi^2} + \left(\frac{\Gamma'}{\Gamma' + \Gamma_{1D}} \right)^2 \frac{1}{1 + \chi^2}, \quad (14)$$

where $\chi = 2(\Delta_A + J_{1D})/(\Gamma_{1D} + \Gamma')$ and $q = -2J_{1D}/(\Gamma_{1D} + \Gamma')$ is the so-called asymmetry parameter. For $\Gamma' \ll \Gamma_{1D}$, the second term is negligible and T/T_0 is a pure Fano resonance, with $q = -\text{Re}\{G_{1D}(\mathbf{r}_j, \mathbf{r}_j, \omega_p)\}/\text{Im}\{G_{1D}(\mathbf{r}_j, \mathbf{r}_j, \omega_p)\}$. Fano resonances arise whenever there is interference between two different transport channels. For instance, in a cavity far from resonance, there is interference arising from all the possible optical paths that contribute to the transmission signal due to reflections at the mirrors, whereas in an unstructured waveguide there is no such interference and thus the lineshape is Lorentzian.

For a single atom, there is a clear mapping between the spectrum lineshape and the local 1D Green's function. For a nanostructure with a purely imaginary self Green's function $\mathbf{G}(x_i, x_i)$ (such as a wave-guide or a cavity at resonance), the spectrum is Lorentzian, and centered around the atomic frequency. However, if the real part is finite, one would observe a frequency shift of the spectrum, which becomes asymmetric. Figure 1(b) shows how the normalized transmission spectrum for a single atom becomes more and more asymmetric for higher ratios J_{1D}/Γ_{1D} . Also, there is an appreciable blueshift of the spectral features.

We would like to remark that the Markov approximation has thus far been employed in our analysis, as every Green's function is considered to be a complex constant over frequency ranges larger than the linewidth of the atoms. If that is not the case, it is not possible to find simple expressions for the Hamiltonian and Lindblad terms for the atomic density matrix. However, the expressions for the transmission and reflection coefficients are valid even when the spectral variation of the Green's function occurs within frequency intervals comparable to and smaller than the atomic linewidth. This fact might not be surprising as, in the low saturation limit, atoms behave as classical dipoles, and an equation for the transmission coefficient identical to Eq. (12) can be found for classical emitters, without resorting to Markov's approximation.

4. Application to several one-dimensional photonic structures

In this section, we analyze the transmission spectra of atoms placed along common quasi-1D nanostructures, such as cavities, waveguides, and photonic crystals.

4.1. Standing-wave cavities

To begin with, we want to illustrate the connection between the Green's function formalism and the well-known Jaynes Cummings (JC) model [38]. For N atoms in a driven cavity of length L and effective area A , the JC Hamiltonian, and its corresponding Lindblad operator read

$$\mathcal{H} = -\hbar\Delta_c \hat{a}^\dagger \hat{a} - \hbar\Delta_A \sum_{i=1}^N \hat{\sigma}_{ee}^i + \hbar \sum_{i=1}^N \mathbf{q}_i \left(\hat{a}^\dagger \hat{\sigma}_{ge}^i + \hat{\sigma}_{eg}^i \hat{a} \right) + \hbar\eta (\hat{a} + \hat{a}^\dagger), \quad (15a)$$

$$\mathcal{L}[\hat{\rho}] = \frac{\Gamma'}{2} \sum_{i,j=1}^N \left(2\hat{\sigma}_{ge}^i \hat{\rho} \hat{\sigma}_{eg}^j - \hat{\sigma}_{eg}^i \hat{\sigma}_{ge}^j \hat{\rho} - \hat{\rho} \hat{\sigma}_{eg}^i \hat{\sigma}_{ge}^j \right) + \frac{\kappa_c}{2} \left(2\hat{a} \hat{\rho} \hat{a}^\dagger - \hat{a}^\dagger \hat{\rho} \hat{a} - \hat{\rho} \hat{a}^\dagger \hat{a} \right), \quad (15b)$$

where \hat{a} is the cavity-field annihilation operator, $\hat{\rho}$ is the density matrix for the atoms and the cavity field, η is a frequency that represents the amplitude of the classical driving field, $\Delta_c = \omega_p - \omega_c$ is the detuning between the driving (probe) and the cavity fields, and κ_c is the cavity-field decay. The atom cavity coupling is $\mathbf{q}_i = \mathbf{q} \cos(k_c x_i)$, where $\mathbf{q} = d\sqrt{\omega_c}/(\hbar\epsilon_0 LA)$ is modulated by a function that depends on the atoms' positions and the cavity wave-vector k_c . The Heisenberg equations of motion for the field and atomic operators are

$$\begin{aligned} \dot{\hat{a}} &= \left(i\Delta_c - \frac{\kappa_c}{2} \right) \hat{a} - i \sum_{i=1}^N \mathbf{q}_i \hat{\sigma}_{ge}^i - i\eta, \\ \dot{\hat{\sigma}}_{ge}^i &= \left(i\Delta_A - \frac{\Gamma'}{2} \right) \hat{\sigma}_{ge}^i + i\mathbf{q}_i \left(\hat{\sigma}_{ee}^i - \hat{\sigma}_{gg}^i \right) \hat{a}. \end{aligned}$$

When $\Gamma' \ll \kappa_c$ and $\mathbf{q} < \min\{\Delta_c, \kappa_c\}$, the cavity field can be adiabatically eliminated, and the field operator re-expressed in terms of the atomic ones, i.e.,

$$\dot{\hat{a}} = 0 \quad \rightarrow \quad \hat{a} = \frac{1}{(\Delta_c + i\frac{\kappa_c}{2})} \left(\eta + \sum_{i=1}^N \mathbf{q}_i \hat{\sigma}_{ge}^i \right).$$

Introducing this expression back into the equation for the atomic operator, one can deduce a master equation for the atomic density matrix $\hat{\rho}_A$. The new Hamiltonian and Lindblad operators read just as those of Eqs. (3a) and (3b), but for a classical driving field, and with spin exchange and decay rates into the cavity mode given by $J_{1D}^{ij}(\Gamma_{1D}^{ij}) = J_{1D}(\Gamma_{1D}) \cos(k_c x_i) \cos(k_c x_j)$, with $J_{1D} = -\mathbf{q}^2 \Delta_c / (\Delta_c^2 + \kappa_c^2/4)$, and $\Gamma_{1D} = \mathbf{q}^2 \kappa_c / (\Delta_c^2 + \kappa_c^2/4)$. It can thus be seen that the Markovian approximation to arrive at these equations is equivalent to the absence of strong coupling effects within the JC model.

The last step for connecting this simple model with our formalism is to calculate the Green's function of a cavity and confirm that J_{1D}^{ij} and Γ_{1D}^{ij} are precisely those obtained within the JC framework. The Green's function of a quasi-1D cavity formed by partially transmitting mirrors of reflection coefficient r (chosen to be real) is [60]

$$G_{1D}(x_i, x_j, \omega_p) \simeq \frac{ic^2}{2v_g \omega_p A} \frac{e^{ik_p|x_i-x_j|} + r e^{ik_p(L+x_i+x_j)} + r e^{ik_p[L-(x_i+x_j)]} + r^2 e^{ik_p(2L-|x_i-x_j|)}}{1 - r^2 e^{2ik_p L}},$$

where v_g is the group velocity. For high-Q standing-wave cavities, i.e. with $r \simeq 1$, and choosing $v_g = c$, the Green's function can be approximated as

$$G_{1D}(x_i, x_j, \omega_p) \simeq \left(\frac{2ic}{\omega_p A} \right) \frac{1}{1 - r^2 e^{2ik_p L}} \cos(k_p x_i) \cos(k_p x_j).$$

The cavity is resonant at a frequency ω_c with corresponding wave-vector k_c , chosen to be such that $k_c L = 2\pi m$, with m being an integer. Close to resonance, one can write $k_p = k_c + \delta k$, and assume that $\delta k L \ll 1$. Then $1 - r^2 e^{2ik_p L} \simeq 1 - r^2 - 2ir^2 \delta k L$, and the Green's function is simply

$$G_{1D}(x_i, x_j, \omega_p) \simeq - \left(\frac{c^2}{\omega_p L A} \right) \frac{1}{\Delta_c + i\kappa_c/2} \cos(k_c x_i) \cos(k_c x_j),$$

where $\kappa_c = (1 - r^2)c/L$ is the cavity linewidth. Therefore, the atoms' spin-exchange and decay rates are given by

$$J_{1D}^{ij} = (\mu_0 \omega_p^2 d^2 / \hbar) \operatorname{Re} G_{1D}(x_i, x_j, \omega_p) = -\mathbf{q}_i \mathbf{q}_j \frac{\Delta_c}{(\Delta_c^2 + \kappa_c^2/4)} \equiv J_{1D} \cos(k_c x_i) \cos(k_c x_j),$$

$$\Gamma_{1D}^{ij} = (2\mu_0 \omega_p^2 d^2 / \hbar) \operatorname{Im} G_{1D}(x_i, x_j, \omega_p) = -\mathbf{q}_i \mathbf{q}_j \frac{\kappa_c}{(\Delta_c^2 + \kappa_c^2/4)} \equiv \Gamma_{1D} \cos(k_c x_i) \cos(k_c x_j),$$

which is precisely what is obtained within the Jaynes Cummings model.

Let's now look at the transmission spectrum of N atoms in a cavity. As we have just demonstrated, coefficients of the dipole-projected Green's function matrix \mathbf{g} read

$$g_{ij} = g(\omega_p) \cos(k_c x_i) \cos(k_c x_j), \quad (17)$$

where $g(\omega_p) = J_{1D} + i\Gamma_{1D}/2$. Depending on the detuning between the probe field and the cavity resonance, $g(\omega_p)$ can be purely imaginary, yielding dissipative atom-atom interactions, or can have both real and imaginary parts, resulting in both dissipative and dispersive couplings.

The matrix \mathbf{g} is separable (has rank one) as it can be written as the tensor product of just one vector by itself. The matrix has one eigenstate describing a superposition of atomic coherences that couples to the cavity (a "bright mode"), with eigenvalue $\lambda_B = \sum_{i=1}^N g^{ii} = (J_{1D} + i\Gamma_{1D}/2) \sum_{i=1}^N \cos^2(k_c x_i)$. This atomic collective excitation follows spatially the mode profile of the cavity, i.e. $\sigma_{ge}^i \propto \cos(k_c x_i)$. The matrix \mathbf{g} has also $N-1$ decoupled ("dark") modes of eigenvalue 0. Because these dark modes have a zero decay rate into the cavity mode, it is also impossible to excite them employing the cavity field. The optical response is thus entirely controlled by the bright mode, and the transmission is simply

$$t(\Delta_A)/t_0(\Delta_A) = \frac{\Delta_A + i\Gamma'/2}{(\Delta_A + \sum_{i=1}^N J_{1D}^{ii}) + i(\Gamma' + \sum_{i=1}^N \Gamma_{1D}^{ii})/2}. \quad (18)$$

Remarkably, this expression is valid no matter the separation between the atoms or whether they form an ordered or disordered chain. The transmission spectrum corresponds to that of a 'super-atom', where the decay rates and the frequency shifts are enhanced (N-fold if all the diagonal components of \mathbf{g} are equal) compared to those of a single atom. This result replicates the well-known expressions for conventional cavity QED.

4.2. Waveguides

Another paradigm that has been investigated frequently is that of "waveguide QED" [39]. The simple model of such a system consists of a single guided mode with translational invariance, and where the dispersion relation is well-approximated as linear around the atomic resonance frequency. In a 1D translationally invariant system, a source simply emits a plane wave whose phase at the detection point is proportional to the distance of separation. Therefore, the elements of the Green's function matrix \mathbf{g} depend on the distance between the atoms, and read

$$g_{ij} = i \frac{\Gamma_{1D}}{2} e^{ik_p |x_i - x_j|}. \quad (19)$$

Remarkably, the self Green's function in a waveguide is purely imaginary. The coherent interactions between atom i and atom j are dictated by the Hamiltonian [given by Eq. (3a)], and are proportional to $\text{Re}\{g_{ij}\} = -(\Gamma_{1D}/2) \sin k_p |x_i - x_j|$, whereas the

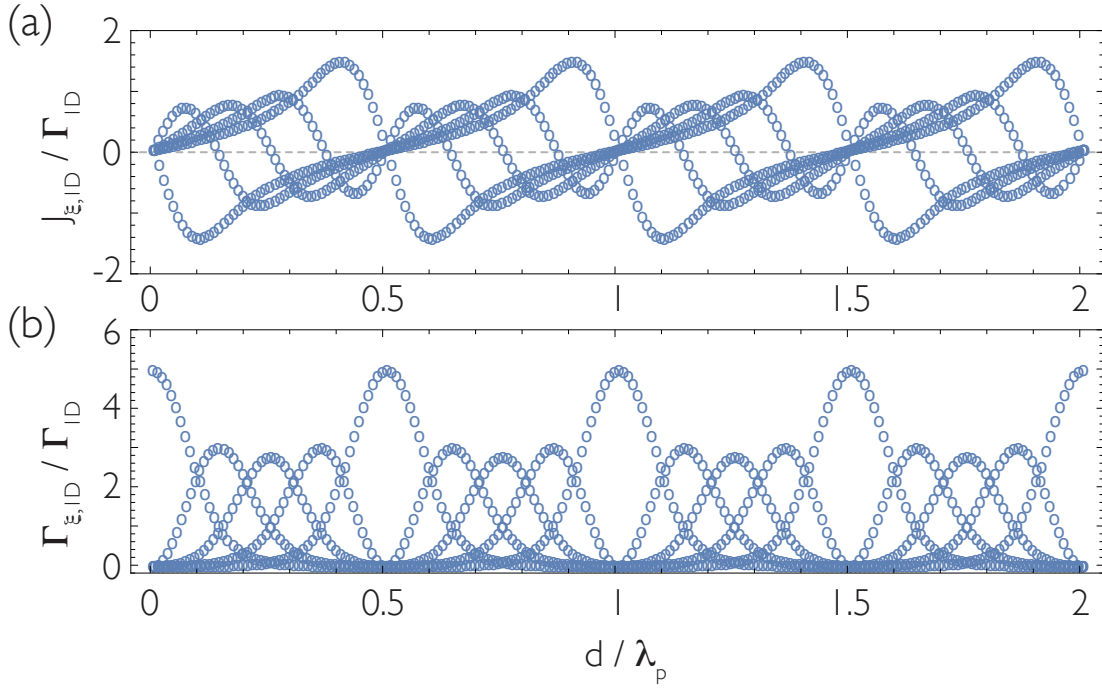


Figure 2. (a) Frequency shifts and (b) decay rates of the collective modes of a regular chain of 5 atoms placed along a waveguide normalized to the single-atom decay rate into the guided mode Γ_{1D} , as a function of the distance d between the atoms in units of the probe wavelength.

dissipation is given by the Lindblad operator [given by Eq. (3b)], which is proportional to $\text{Im}\{g_{ij}\} = (\Gamma_{1D}/2) \cos k_p(x_i - x_j)$ [22, 50]. It is thus clear that by carefully tuning the distance between the emitters, one can engineer fully dissipative interactions. If the atoms form a regular chain and are spaced by a distance d such that $k_p d = n\pi$, where n is an integer number, the matrix \mathbf{g} has only one non-zero eigenvalue $\lambda_B = iN\Gamma_{1D}/2$ associated with the bright atomic mode. This situation is analogous to the case of atoms interacting in an on-resonance cavity. Therefore, there will not be any collective frequency shift, and the lineshape will be a Lorentzian of width $\Gamma_B + \Gamma'$. For n even, the phases of the dipole moments of the atoms are all identical, whereas for odd n the dipole moments of adjacent atoms are π out of phase.

For a regular chain with lattice constant different from $k_p d = n\pi$, or for atoms placed randomly along the waveguide, the coefficients of matrix \mathbf{g} have both a real and imaginary part, and, to the best of our knowledge, there is no analytic expression for the eigenvalues of \mathbf{g} . Figure 2 shows the frequency shifts and decay rates of the collective modes of a $N = 5$ atom chain as a function of the separation between the atoms. For separations where $k_p d = n\pi$, the real part of the Green's function is zero and the imaginary part of all modes but one goes to zero, whereas for other spacings one generically gets a zoo of coherent and dissipative couplings of comparable strength. This occurs because the real and imaginary parts of g_{ij} are generically of similar magnitude. Figure 3 shows the transmission and reflection spectra for $N = 20$ atoms separated by

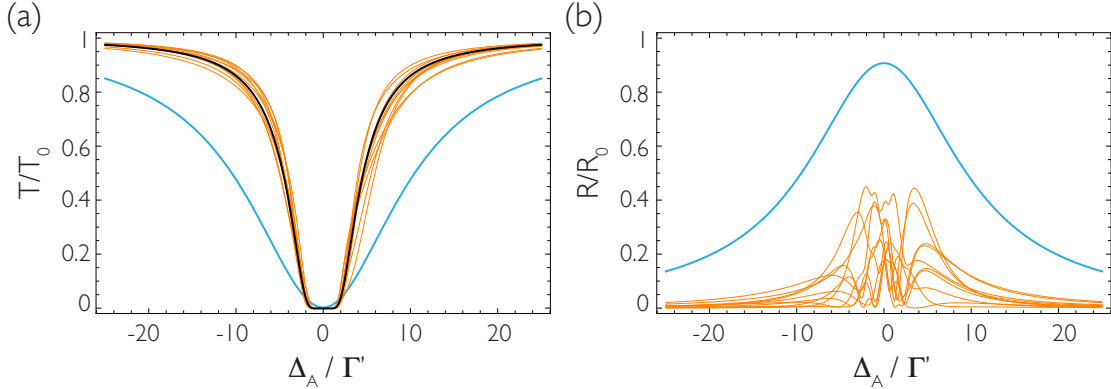


Figure 3. (a) Normalized transmission spectra for 20 atoms interacting through the guided modes of an unstructured waveguide. The blue line represents a regular separation between the atoms of $d = \lambda_p/2$. The orange curves show 10 different spectra obtained by randomly placing the atoms along the nanostructure. The black curve represents the "non-interacting" case of Eq. (20). (b) Normalized reflection spectra for the same situations as in (a). We have chosen $\Gamma_{1D} = \Gamma'$.

$k_p d = \pi$ (blue curve), and for several random realizations where each atomic position is chosen randomly from a distribution $k_p x_i \in [0, 2\pi]$ (orange curves). The black line represents the non-interacting case, which is obtained by setting the non-diagonal terms of \mathbf{g} to zero, yielding a transmission spectrum

$$t(\Delta_A)/t_0(\Delta_A) = \left(\frac{\Delta_A + i\Gamma'/2}{\Delta_A + i(\Gamma' + \Gamma_{1D})/2} \right)^N, \quad (20)$$

where the transmission coefficient is a product of the transmission coefficient of each single atom, and the frequency shifts and decay rates are not collective quantities but, instead, single-atom parameters.

Figure 3(a) also shows that, for random filling, although the atoms interact with each other ($\mathbf{g}_{ij \neq i} \neq 0$), the transmission spectra follow closely that of a non-interacting system, for which all the off-diagonal elements are zero ($\mathbf{g}_{ij \neq i} = 0$), and the eigenvalues of matrix \mathbf{g} are proportional to the self Green's functions $[\mathbf{G}(x_i, x_i)]$ at the atoms' positions. In this case, the behavior of the emitters cannot be understood in terms of the 'super-atom' picture, as the transmission spectrum of the system is significantly different from a Lorentzian. In particular, for the non-interacting scenario, one can recast Eq. (20) into an exponential, and the transmittance recovers the well-known form of a Beer-Lambert law, reading

$$T(\Delta_A)/T_0(\Delta_A) = \exp \left[-N \ln \frac{\Delta_A^2 + (\Gamma' + \Gamma_{1D})^2/4}{\Delta_A^2 + \Gamma'^2/4} \right] \simeq \exp \left[-\frac{\text{OD}}{1 + (2\Delta_A/\Gamma')^2} \right], \quad (21)$$

where $\text{OD} \equiv 2N\Gamma_{1D}/\Gamma'$ is the optical depth and the last equality holds for $\Gamma_{1D} \ll \Gamma'$. This is exactly the same behavior that an atomic ensemble in free space would exhibit. This occurs only for non-negligible Γ' , which suppresses multiple reflections. Otherwise one would see huge fluctuations associated with Anderson localization in the spectra.

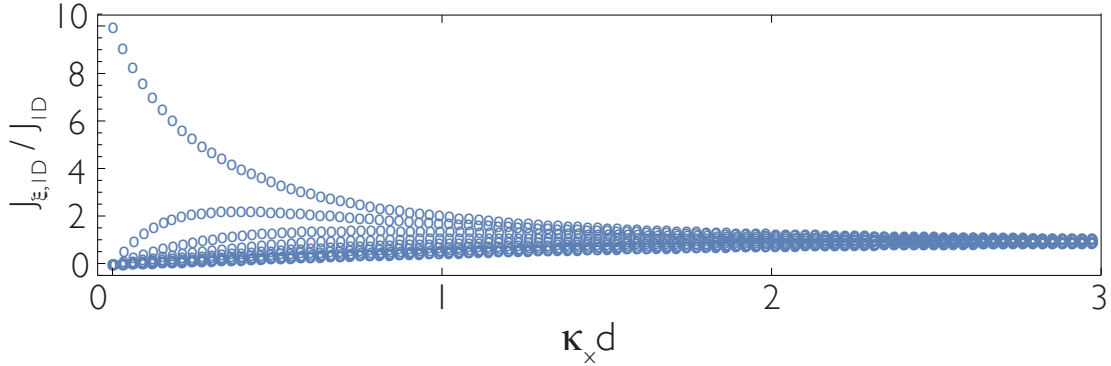


Figure 4. Collective frequency shifts of the modes of a regular chain of $N=10$ atoms in the bandgap of an infinite photonic crystal as a function of $\kappa_x d$, where κ_x^{-1} is the spatial range of the interaction and d is the distance between atoms. The atoms are placed at even antinodes of the Bloch modes.

The reflectance spectrum, on the other hand, is more complex and carries more information than the transmittance, as shown in Fig. 3(b). In contrast to the case of the transmission coefficient, the reflection does not admit a simple formula in terms of the eigenvalues of the system. This is only possible when the Green's function is separable, namely, when the distance between the atoms is $d = n\lambda_p/2$.

4.3. Photonic crystal bandgaps

The band-gap region of a photonic crystal waveguide (PCW) is a very appealing scenario to explore coherent atom-atom interactions, as light cannot propagate, and atoms interact with each other through evanescent fields [30]. For a photonic crystal waveguide of lattice constant a the elements of matrix \mathbf{g} are well approximated by

$$g_{ij} = J_{1D} \cos(\pi x_i/a) \cos(\pi x_j/a) e^{-\kappa_x |x_i - x_j|}, \quad (22)$$

where the cosine terms account for the spatial profile of the Bloch modes, and κ_x^{-1} is the finite range of interaction due to the evanescent decay of the guided mode field in the bandgap, which is controlled by detuning the band-edge frequency from the atomic resonance. It should be noted that in this idealized picture, g_{ij} is purely real, indicating the absence of collective emission into the PCW. This is naturally expected, due to the absence of guided modes at the atomic frequency. In practice, residual decay might still exist to the extent that the mediating photon has a decay channel. This could be either due to the finite length of the PCW, which can cause the photon to leak out the ends and is suppressed when $\kappa_x L \gg 1$, or through scattering and absorption losses of the PCW. Given that these photonic decay processes can be made small, for conceptual simplicity here we treat the idealized case.

For a chain of periodically spaced atoms placed in even antinodes of the Bloch

modes, the dipole-projected Green's function matrix reads

$$\mathbf{g} = J_{1D} \begin{pmatrix} 1 & \chi & \chi^2 & \cdots & \chi^{N-1} \\ \chi & 1 & \chi & \cdots & \chi^{N-2} \\ \vdots & \vdots & \vdots & \ddots & \vdots \\ \chi^{N-1} & \chi^{N-2} & \chi^{N-3} & \cdots & 1 \end{pmatrix}, \quad (23)$$

where we have defined $\chi \equiv e^{-\kappa_x d}$, with d being the distance between nearest-neighbor atoms. The matrix \mathbf{g} is a real symmetric Toeplitz matrix (or bisymmetric matrix). Neglecting higher order contributions besides first-neighbor, an approximation valid for $\kappa_x d \gg 1$, \mathbf{g} becomes a tridiagonal Toeplitz matrix whose eigenvalues and eigenvectors are [61]:

$$\lambda_\xi \equiv J_{1D,\xi} = 1 + 2e^{-\kappa_x d} \cos \left(\frac{\xi\pi}{N+1} \right), \quad (24a)$$

$$v_{\xi,j} = \sqrt{\frac{2}{N+1}} \sin \left(\frac{\xi j \pi}{N+1} \right). \quad (24b)$$

In this simple tight binding model, the frequency shifts of the collective atomic modes are distributed around J_{1D} with a frequency spread controlled by κ_x (i.e., for larger κ_x , the modes are closer in frequency). However, if the interaction length is very large compared to the distance between the atoms, the approximation of neglecting higher order neighbors falls apart, and the eigenvalues start to show a different behavior. Eventually, when the interaction length becomes infinite (or much larger than the length of the atomic cloud), there is only one bright mode, of eigenvalue $\lambda_B = NJ_{1D}$. This is analogous to the cavity case, where the interaction range is also infinite, except now the eigenvalue is purely real. This can be observed in Fig. 4, which shows how the collective frequency shifts coalesce towards J_{1D} for large $\kappa_x d$. The band-edge of a photonic crystal is thus a cross-over region in which the single bright mode approximation holds and then transitions to another regime where it breaks down, as the guided mode becomes evanescent and decays substantially within the length of the PCW. Importantly, the bandgap of a photonic crystal provides a tunable interaction range, a feature which is unique to this kind of nanostructure, and makes PCWs remarkably different reservoirs from either cavities or unstructured waveguides.

In the following section, we present some predictions for the transmission spectrum of two atoms coupled to a PCW for Γ_{1D} and J_{1D} values that can be achieved experimentally in the coming years. We hope that the foreseen large coherent couplings between the atoms combined with low dissipation through the guided mode help to stimulate a new generation of experiments that go beyond the current state of the art.

5. Experimental perspectives

In a recent experiment [36], the authors have observed signatures of collective atom-light interactions in the transmission spectra of atoms coupled to an alligator photonic

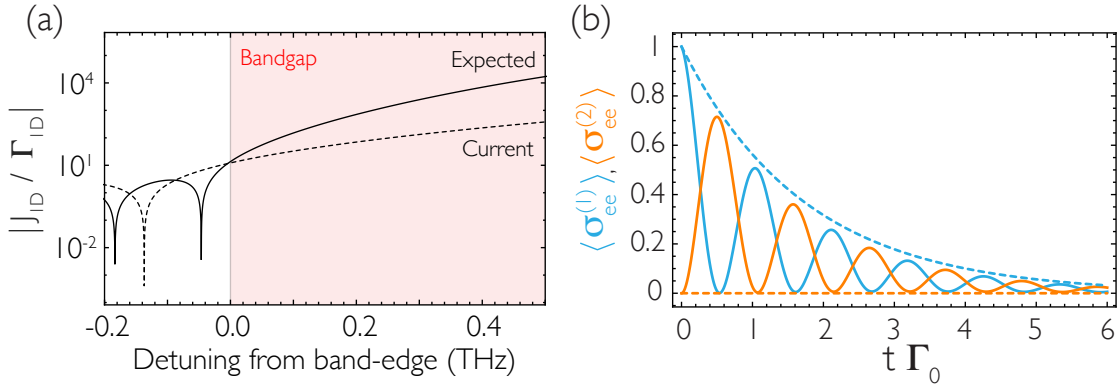


Figure 5. (a) Magnitude of the ratio between the coherent and dissipative couplings through the guided mode of an alligator PCW [36]. The dashed line shows the ratio as given in Fig.4 of Ref. [36], and the continuous curve represents the expected ratio that could be achieved within the next years (see text for more details). (b) Evolution of the excited state population of atom 1 (blue curve) and 2 (orange curve) after fully inverting atom 1 at the initial time. The resonance frequency of the atoms lies in the bandgap of the photonic crystal, with the atoms placed at successive even antinodes (continuous curve). The dashed line represents the non-interacting scenario, where the off-diagonal terms of \mathbf{g} are zero. The spin exchange and decay rates are chosen to be $J_{1D} = -3\Gamma_0$, $\Gamma_{1D} = 0.15\Gamma_0$, and $\Gamma' = 0.5\Gamma_0$. The lattice constant is $a = 370$ nm and the range of interaction is $\kappa_x^{-1} = 80a$.

crystal waveguide. They have recorded these spectra for various frequencies around the band edge of the PCW, exploring different physical regimes. Outside the bandgap, due to the finite size of the PCW, they observe the formation of a low-finesse cavity mode [as shown in Fig. 3(a) of Ref. [36], at a frequency ν_1]. At resonance with this cavity mode, the dissipative single-atom coupling to the structure is $\Gamma_{1D}(\nu_1) \simeq 1.5\Gamma_0$, as obtained from steady-state transmission lineshape measurements. The decay rate into leaky modes is $\Gamma'/\Gamma_0 \simeq 1.1$, estimated from finite-difference time-domain (FDTD) numerical calculations.

After tuning the spectral features of the PCW so that the resonance frequency of the atoms moves into the bandgap, they observe asymmetric lineshapes, revealing significant coherent coupling. Specifically at $\nu_{BG} = 60$ GHz inside the bandgap, the spin exchange and decay rates are $J_{1D}(\nu_{BG})/\Gamma_0 \simeq -0.2$ and $\Gamma_{1D}(\nu_{BG})/\Gamma_0 \simeq 0.01$, respectively. Due to the evanescent character of the field in the bandgap, the interaction range is finite, and at ν_{BG} its value is $\kappa_x^{-1} \simeq 80a$, being $a = 370$ nm the lattice constant of the alligator PCW. While this experiment constitutes the first observation of more than one emitter interacting through the guided modes around the band edge of a PCW, the values of J_{1D} and Γ_{1D} are not yet good enough to observe *direct* signatures of atom-atom interactions such as time-dependent spin exchange. Nevertheless, we expect that near-term advances of the current set up will yield dramatic improvements on these rates, opening the door to exploring exciting collective atomic phenomena.

In particular, instead of using an alligator PCW, one can employ a slot photonic

crystal waveguide [4, 62], i.e. a quasi-1D waveguide embedded in a 2D photonic crystal. This structure would be advantageous due to several reasons. First of all, it inhibits atomic emission into non-guided modes due to the surrounding 2D photonic bandgap that reduces the modes into which the atom can radiate. Absent inhomogeneous broadening, early simulations demonstrate that it is possible to achieve a very small non-guided decay rate, i.e. $\Gamma' \simeq 0.5\Gamma_0$. Moreover, one can engineer flatter bands, which leads to an increase of the group index of $n_g \simeq 30$ near the band-edge (three times larger than that of the current alligator), according to FDTD simulations. Then, both J_{1D} and Γ_{1D} would experience a three-fold increase. Finally, by trapping the atoms at the center of the nanostructure, in between the two slots and not above as it is currently done, we have estimated that J_{1D} and Γ_{1D} would be five times larger. Summarizing, we project $\Gamma_{1D}(\nu_1)/\Gamma_0 \simeq 22$ at the first cavity resonance. This yields the values of $J_{1D}(\nu_{BG})/\Gamma_0 \simeq -3$ and $\Gamma_{1D}(\nu_{BG})/\Gamma_0 \simeq 0.15$ for a detuning from the band edge $\nu_{BG} = 20$ GHz, where the range of interaction is $\kappa_x^{-1} \simeq 80a$.

Figure 5(a) compares the ratio $|J_{1D}/\Gamma_{1D}|$ between the coherent and dissipative guided-mode rates for the current alligator PCW (dashed line) and the described slot PCW (continuous line). The improved ratio for the later structure can already be observed at frequencies just beyond the band-edge, and becomes $|J_{1D}/\Gamma_{1D}| \simeq 10^4$ at a detuning of 0.5 THz from the band-edge. An indisputable signature of collective behavior is represented in Fig. 5(b), which shows the evolution of the excited state populations of two atoms placed at successive even antinodes (continuous curve), after initially inverting one of them. The atoms interact through the guided modes of the already described slot PCW, and their resonance frequency lies inside the bandgap, at the frequency for which the interaction range is $\kappa_x^{-1} \simeq 80a$. The dashed lines show the expected result for non interacting atoms, where the off-diagonal terms of \mathbf{g} are zero, a situation that occurs when the atoms are separated by a distance $d \gg \kappa_x^{-1}$.

To summarize, we believe that there is a bright future for experiments involving not only atoms, but also superconducting qubits interacting through the guided modes of a microwave photonic crystal. In a recent experiment, a ratio of $\Gamma_{1D}/\Gamma' = 50$ has already been achieved for transmon qubits connected to a 1D coplanar microwave transmission line [23]. Combined with the exciting recent advances in microwave photonic crystal fabrication [37], we expect a next generation of experiments where many qubits interact with each other in a mostly coherent manner.

6. Conclusion

We have analyzed the optical response of a chain of atoms placed along a quasi-1D nanophotonic structure in terms of the classical electromagnetic Green's function. This formalism is valid in the presence of absorptive and dispersive media.

We find that the linear response of the atoms can be understood in terms of collective atomic eigenstates of the Green's function matrix $\mathbf{g}(x_i, x_j)$ for all pairs of atoms. In particular, we have derived a closed expression for the transmission spectra

that only depends on the cooperative frequency shifts and decay rates of these modes. We have shown that the transmission coefficient is a direct probe of the Green's function of the nanostructure, enabling us to determine whether the atom-light interactions are fundamentally dispersive or dissipative in character as well as to quantify the degree of cooperative interaction. We have gained insight into the interactions between atoms and quasi-1D cavities, waveguides, and photonic crystals, structures of relevance in recent experiments, as well as provided estimations of what can be observed in the near future.

The Green's function formalism provides a natural language that unifies nanophotonics and quantum optics, and our results apply not only to atoms [36], but to many other quantum emitters, such as superconducting qubits [37], NV centers [63], rare earth ions [64] or quantum dots [4], interacting with any kind of quasi-1D photonic structures or circuits.

Appendix A. Transmission and reflection coefficients in terms of Green's functions

We begin by recalling Eq. (10),

$$E^+(x) \equiv E_y^+(x) = E_p^+(x) - \sum_{\xi=1}^N \frac{(\mathbf{g}^T(x) \cdot \mathbf{v}_\xi) (\mathbf{v}_\xi^T \cdot \mathbf{E}_p^+)}{(\Delta_A + J_{\xi,1D}) + i(\Gamma' + \Gamma_{\xi,1D})/2},$$

which relates the field along any point of the structure with the collective atomic modes. In order to calculate the transmission spectra, we need an expression that connects the output and the input fields. To do so, let's consider that we have a dipole p_{left} placed to the left of the first atom of the chain, at position x_{left} , which is the source of the probe field E_p^+ . For the sake of simplicity, p_{left} is polarized along \hat{y} , the same polarization of the guided mode field. To obtain the transmission coefficient, we evaluate the field at position x_{right} , immediately to the right of the last atom of the chain. When the atoms are not present, the probe field at the left and right positions of the quasi-1D nanostructure are

$$E_p^+(x_{\text{left}}) = \mu_0 \omega_p^2 G_{1D}(x_{\text{left}}, x_{\text{left}}) p_{\text{left}}, \quad (\text{A.1a})$$

$$E_p^+(x_{\text{right}}) = \mu_0 \omega_p^2 G_{1D}(x_{\text{right}}, x_{\text{left}}) p_{\text{left}}. \quad (\text{A.1b})$$

Then, the transmission for the system without the atoms is simply

$$t_0(\Delta_A) = \frac{E_p^+(x_{\text{right}})}{E_p^+(x_{\text{left}})} = \frac{G_{1D}(x_{\text{right}}, x_{\text{left}})}{G_{1D}(x_{\text{left}}, x_{\text{left}})}. \quad (\text{A.2})$$

When N atoms are placed in the vicinity of the nanostructure, the field at position x_{right} is

$$\begin{aligned} E^+(x_{\text{right}}) &= E_p^+(x_{\text{right}}) - \frac{1}{g(x_{\text{left}}, x_{\text{left}})} \sum_{\xi=1}^N \frac{(\mathbf{g}^T(x_{\text{right}}) \cdot \mathbf{v}_\xi) (\mathbf{v}_\xi^T \cdot \mathbf{g}(x_{\text{left}}))}{(\Delta_A + J_{\xi,1D}) + i(\Gamma' + \Gamma_{\xi,1D})/2} E_p^+(x_{\text{left}}) \\ &= \left(t_0(\Delta_A) - \frac{1}{g(x_{\text{left}}, x_{\text{left}})} \sum_{\xi=1}^N \frac{(\mathbf{g}^T(x_{\text{right}}) \cdot \mathbf{v}_\xi) (\mathbf{v}_\xi^T \cdot \mathbf{g}(x_{\text{left}}))}{(\Delta_A + J_{\xi,1D}) + i(\Gamma' + \Gamma_{\xi,1D})/2} \right) E_p^+(x_{\text{left}}), \end{aligned}$$

where we have employed that the probe field at atom x_j can be related to $E_p^+(x_{\text{left}})$ as $E_p^+(x_j) = \mu_0 \omega_p^2 G_{1D}(x_j, x_{\text{left}}) p_{\text{left}} = \frac{G_{1D}(x_j, x_{\text{left}})}{G_{1D}(x_{\text{left}}, x_{\text{left}})} E_p^+(x_{\text{left}})$. Then, the normalized transmission coefficient is

$$t(\Delta_A)/t_0(\Delta_A) = 1 - \frac{1}{g(x_{\text{right}}, x_{\text{left}})} \sum_{\xi=1}^N \frac{(\mathbf{g}^T(x_{\text{right}}) \cdot \mathbf{v}_\xi)(\mathbf{v}_\xi^T \cdot \mathbf{g}(x_{\text{left}}))}{(\Delta_A + J_{\xi,1D}) + i(\Gamma' + \Gamma_{\xi,1D})/2}, \quad (\text{A.3})$$

as shown in the main text. Let's now calculate the reflection coefficient. Without the atoms, the field at x_{left} is $E^+(x_{\text{left}}) = [1 + r_0(\Delta_A)] E_p^+(x_{\text{left}})$. When the atoms are present, the field reads

$$E^+(x_{\text{left}}) = [1 + r_0(\Delta_A)] E_p^+(x_{\text{left}}) - \frac{1}{g(x_{\text{left}}, x_{\text{left}})} \sum_{\xi=1}^N \frac{(\mathbf{g}^T(x_{\text{left}}) \cdot \mathbf{v}_\xi)(\mathbf{v}_\xi^T \cdot \mathbf{g}(x_{\text{left}}))}{(\Delta_A + J_{\xi,1D}) + i(\Gamma' + \Gamma_{\xi,1D})/2} E_p^+(x_{\text{left}}).$$

Following similar steps as those above, we find

$$r(\Delta_A) = r_0(\Delta_A) - \frac{1}{g(x_{\text{left}}, x_{\text{left}})} \sum_{\xi=1}^N \frac{(\mathbf{g}^T(x_{\text{left}}) \cdot \mathbf{v}_\xi)(\mathbf{v}_\xi^T \cdot \mathbf{g}(x_{\text{left}}))}{(\Delta_A + J_{\xi,1D}) + i(\Gamma' + \Gamma_{\xi,1D})/2}, \quad (\text{A.4})$$

the equation in the main text.

Appendix B. Derivation of Equation (12) for the transmission

We can exploit some properties of 1D systems to arrive to the closed expression for the transmission shown in Eq. (12), which only depends of the decay rates and frequency shifts of the modes, not on their spatial structure (i.e. the eigenfunctions). We first show how to derive the 1D Green's function wave equation, and how the solution is related to the full quasi-1D solution. We start with the 3D Green's function \mathbf{G}_{1D} for the guided mode, which follows Eq. (1). We assume that the guided modes are transverse waves that travel in the $\pm \hat{x}$ direction and are polarized along \hat{y} , and that the field is approximately uniform in the transverse directions. From 3D, one can in principle construct the guided modes and their dispersion relations $\omega(k)$, from which one can identify an effective dielectric constant $\epsilon_{\text{eff}}(x, \omega)$ which produces the same behavior (at least within some bandwidth). The final answer that we are trying to achieve does not depend on explicit construction of $\epsilon_{\text{eff}}(x, \omega)$. The result is a Helmholtz equation for the Green's function that reads

$$\left[\frac{d^2}{dx^2} + \frac{\omega^2}{c^2} \epsilon_{\text{eff}}(x, \omega) \right] \tilde{G}_{1D}(x, x', \omega) = -\delta(x - x'), \quad (\text{B.1})$$

where $\tilde{G}_{1D} = A G_{1D}$, being A the effective mode area. The solution for this second order linear ordinary differential equation can be expressed as the sum of the two homogeneous solutions. The Green's function can then be written in terms of the auxiliary fields $\tilde{\phi}_{L,R}(x)$, which are solutions of the homogeneous equation, as

$$\tilde{G}_{1D}(x, x') = \frac{\Theta(x' - x) \tilde{\phi}_L(x') \tilde{\phi}_R(x) + \Theta(x - x') \tilde{\phi}_R(x') \tilde{\phi}_L(x)}{\text{DISTRIBUTION A: Distribution approved for public release.}}, \quad (\text{B.2})$$

where W is the Wronskian, which does not depend on the position, and is given by

$$W = \tilde{\phi}_R(x') \frac{d\tilde{\phi}_L(x')}{dx'} - \frac{d\tilde{\phi}_R(x')}{dx'} \tilde{\phi}_L(x'). \quad (\text{B.3})$$

We can then recover the full Green's function between atom i and atom j as

$$G_{1D}(x_i, x_j, \omega) = \frac{1}{A} \tilde{G}_{1D}(x_i, x_j, \omega) = [\Theta(x_j - x_i)\phi_L(x_j)\phi_R(x_i) + \Theta(x_i - x_j)\phi_L(x_i)\phi_R(x_j)], \quad (\text{B.4})$$

where $\phi_{R,L} \equiv \tilde{\phi}_{R,L}/\sqrt{AW}$. Then, the dipole-projected Green's function is

$$g_{ij} = \Theta(x_j - x_i)s_{ji} + \Theta(x_i - x_j)s_{ij},$$

where $s_{ij} = \varphi_L(x_i)\varphi_R(x_j)$, with $\varphi_{L,i} = \sqrt{\mu_0\omega_p d^2/\hbar} \phi_L(x_i)$ and $\varphi_{R,j} = \sqrt{\mu_0\omega_p d^2/\hbar} \phi_R(x_j)$. It is convenient to define the rank-one matrix $\mathfrak{s} = \boldsymbol{\varphi}_L \otimes \boldsymbol{\varphi}_R^T$, where $\boldsymbol{\varphi}_{\{R,L\}} = (\varphi_{\{R,L\}}(x_1), \dots, \varphi_{\{R,L\}}(x_N))$ is a vector of N components. Let's now proceed to demonstrate Eq. (12). In terms of the eigenfunctions of \mathfrak{g} , the transmission is

$$\begin{aligned} t(\Delta_A)/t_0(\Delta_A) &= 1 - \frac{1}{g(x_{\text{right}}, x_{\text{left}})} \sum_{\xi=1}^N \frac{(\mathbf{g}^T(x_{\text{right}}) \cdot \mathbf{v}_\xi) (\mathbf{v}_\xi^T \cdot \mathbf{g}(x_{\text{left}}))}{(\Delta_A + J_{\xi,1D}) + i(\Gamma' + \Gamma_{\xi,1D})/2} \\ &= 1 - \frac{1}{g(x_{\text{right}}, x_{\text{left}})} (\mathbf{g}^T(x_{\text{right}}) \cdot \mathcal{M}^{-1} \cdot \mathbf{g}(x_{\text{left}})), \end{aligned}$$

where \mathcal{M} is given in Eq. (8). Since $\mathbf{g} \propto G_{1D}$, and using the expression for the Green's function in terms of the right-going and left-going field solutions [Eq. (B.4)], we find

$$t(\Delta_A)/t_0(\Delta_A) = 1 - \boldsymbol{\varphi}_R^T \cdot \frac{1}{\Delta_A + i\Gamma'/2 + \mathfrak{g}} \cdot \boldsymbol{\varphi}_L = 1 - \mathbf{v}^T \cdot \frac{1}{\mathbb{1} + \tilde{\mathfrak{g}}} \cdot \mathbf{u},$$

where we have defined $\mathbf{v} \equiv \boldsymbol{\varphi}_R/\sqrt{\Delta_A + i\Gamma'/2}$, $\mathbf{u} \equiv \boldsymbol{\varphi}_L/\sqrt{\Delta_A + i\Gamma'/2}$, and $\tilde{\mathfrak{g}} \equiv \mathfrak{g}/(\Delta_A + i\Gamma'/2)$. By the matrix determinant lemma [54], we know that for a invertible matrix \mathbf{A} and a pair of vectors \mathbf{u}, \mathbf{v} , we can write $\det(\mathbf{A} + \mathbf{u} \otimes \mathbf{v}^T) = \det(\mathbf{A}) (1 + \mathbf{v}^T \cdot \mathbf{A}^{-1} \cdot \mathbf{u})$. Choosing $\mathbf{A} = -(\mathbb{1} + \tilde{\mathfrak{g}})$, we find

$$t(\Delta_A)/t_0(\Delta_A) = \frac{\det(\mathbb{1} + \tilde{\mathfrak{g}} - \mathbf{u} \otimes \mathbf{v}^T)}{\det(\mathbb{1} + \tilde{\mathfrak{g}})} = \frac{\det((\Delta_A + i\Gamma'/2)\mathbb{1} + \mathfrak{g} - \mathfrak{s})}{\det((\Delta_A + i\Gamma'/2)\mathbb{1} + \mathfrak{g})}.$$

Since $(\Delta_A + i\Gamma'/2)\mathbb{1} + \mathfrak{g} - \mathfrak{s}$ is a triangular matrix with $(\Delta_A + i\Gamma'/2)$ in the diagonal entries, and the determinant of a triangular matrix is the product of the diagonal entries, we find $\det((\Delta_A + i\Gamma'/2)\mathbb{1} + \mathfrak{g} - \mathfrak{s}) = (\Delta_A + i\Gamma'/2)^N$, which yields

$$t(\Delta_A)/t_0(\Delta_A) = \frac{(\Delta_A + i\Gamma'/2)^N}{\det((\Delta_A + i\Gamma'/2)\mathbb{1} + \mathfrak{g})} = \prod_{\xi=1}^N \frac{\Delta_A + i\Gamma'/2}{(\Delta_A + J_{\xi,1D}) + i(\Gamma' + \Gamma_{\xi,1D})/2},$$

as the determinant of a matrix is the product of its eigenvalues. The above expression is precisely Eq. (12). To the best of our knowledge, it is not possible to obtain a simplified expression for the reflection coefficient.

Acknowledgments

We thank S.-P. Yu for sharing his insight on slot photonic waveguides. We are also grateful to O. J. Painter, A. Keller, M. Fang, and P. Dieterle for stimulating discussions about superconducting qubits. Funding is provided by the AFOSR QuMPASS MURI, NSF Grant PHY-1205729, the ONR QOMAND MURI, the DOD NSSEFF program, and the IQIM, an NSF Physics Frontiers Center with support of the Moore Foundation. A. A.-G. was supported by the IQIM Postdoctoral Fellowship and the Global Marie Curie Fellowship LANTERN (655701). DEC acknowledges support from Fundacio Privada Cellex Barcelona, Marie Curie CIG ATOMNANO, MINECO Severo Ochoa Grant SEV-2015-0522, and ERC Starting Grant FoQAL.

References

- [1] E. M. Purcell. Spontaneous emission probabilities at radio frequencies. *Phys. Rev.*, 69:681, 1946.
- [2] D. Kleppner. Inhibited spontaneous emission. *Phys. Rev. Lett.*, 47:233–236, 1981.
- [3] S. Haroche and D. Kleppner. Cavity quantum electrodynamics. *Phys. Today*, 42(1):24, 1989.
- [4] P. Lodahl, S. Mahmoodian, and S. Stobbe. Interfacing single photons and single quantum dots with photonic nanostructures. *Rev. Mod. Phys.*, 87:347, 2015.
- [5] J. Vuckovic and Y. Yamamoto. Photonic crystal microcavities for cavity quantum electrodynamics with a single quantum dot. *App. Phys. Lett.*, 82:2374–2376, 2003.
- [6] T. Yoshie, A. Scherer, J. Hendrickson, G. Khitrova, H. M. Gibbs, G. Rupper, C. Ell, O. B. Shchekin, and D. G. Deppe. Vacuum Rabi splitting with a single quantum dot in a photonic crystal nanocavity. *Nature*, 432:200–203, 2004.
- [7] T. Aoki, B. Dayan, E. Wilcut, W. P. Bowen, A. S. Parkins, H. J. Kimble, T. J. Kippenberg, and K. J. Vahala. Observation of strong coupling between one atom and a monolithic microresonator. *Nature*, 443:671, 2006.
- [8] K. Hennessy, A. Badolato, M. Winger, D. Gerace, M. Atatüre, S. Gulde, S. Fält, E. L. Hu, and A. Imamoglu. Quantum nature of a strongly coupled single quantum dot-cavity system. *Nature*, 445:896–899, 2007.
- [9] D. Hunger, T. Steinmetz, Y. Colombe, C. Deutsch, T. W. Hansch, and J. Reichel. A fiber Fabry-Perot cavity with high finesse. *New J. Phys.*, 12:065038, 2010.
- [10] J. D. Thompson, T. G. Tiecke, N. P. de Leon, J. Feist, A. V. Akimov, M. Gullans, A. S. Zibrov, V. Vuletic, and M. D. Lukin. Coupling a single trapped atom to a nanoscale optical cavity. *Science*, 6137:1202–1205, 2013.
- [11] H. Paik, D. I. Schuster, L. S. Bishop, G. Kirchmair, G. Catelani, A. P. Sears, B. R. Johnson, M. J. Reagor, L. Frunzio, L. I. Glazman, S. M. Girvin, M. H. Devoret, and R. J. Schoelkopf. Observation of high coherence in Josephson junction qubits measured in a three-dimensional circuit QED architecture. *Phys. Rev. Lett.*, 107:240501, 2011.
- [12] C. Rigetti, J. M. Gambetta, S. Poletto, B. L. T. Plourde, J. M. Chow, A. D. Corcoles, J. A. Smolin, S. T. Merkel, J. R. Rozen, G. A. Keefe, M. B. Rothwell, M. B. Ketchen, and M. Steffen. Superconducting qubit in a waveguide cavity with a coherence time approaching 0.1 ms. *Phys. Rev. B*, 86:100506, 2012.
- [13] M. Bajcsy, S. Hofferberth, V. Balic, T. Peyronel, M. Hafezi, A. S. Zibrov, V. Vuletic, and M. D. Lukin. Efficient all-optical switching using slow light within a hollow fiber. *Phys. Rev. Lett.*, 102:203902, 2009.
- [14] V. I. Balykin, K. Hakuta, F. Le Kien, J. Q. Liang, and M. Morinaga. Atom trapping and guiding with a subwavelength-diameter optical fiber. *Phys. Rev. A*, 70:011401, 2004.
- [15] P. Londero, V. Venkataraman, A. R. Bhagwat, A. D. Slepkov, and A. L. Gaeta. Ultralow-power

four-wave mixing with Rb in a hollow-core photonic band-gap fiber. *Phys. Rev. Lett.*, 103:043602, 2009.

[16] E. Vetsch, D. Reitz, G. Sagué, R. Schmidt, S. Dawkins, and A. Rauschenbeutel. Optical interface created by laser-cooled atoms trapped in the evanescent field surrounding an optical nanofiber. *Phys. Rev. Lett.*, 104:203603, 2010.

[17] A. Goban, K. S. Choi, D. J. Alton, C. Ding, C. Lacroix, M. Pototschnig, T. Thiele, N. P. Stern, and H. J. Kimble. Demonstration of a state-insensitive, compensated nanofiber trap. *Phys. Rev. Lett.*, 109:033603, 2012.

[18] H. L. Sørensen, J.B. Béguin, K. W. Kluge, I. Iakourov, A. S. Sørensen, J. J. Müller, E. S. Polzik, and J. Appel, arXiv:1601.04869.

[19] D. E. Chang, A. S. Sørensen, E. A. Demler, and M. D. Lukin. A single-photon transistor using nanoscale surface plasmons. *Nat. Phys.*, 3:807–812, 2007.

[20] A. V. Akimov, A. Mukherjee, C. L. Yu, D. E. Chang, A. S. Zibrov, P. R. Hemmer, H. Park, and M. D. Lukin. Generation of single optical plasmons in metallic nanowires coupled to quantum dots. *Nature*, 450:402–406, 2007.

[21] A. Huck, S. Kumar, A. Shakoor, and U. L. Andersen. Controlled coupling of a single nitrogen-vacancy center to a silver nanowire. *Phys. Rev. Lett.*, 106:096801, 2011.

[22] A. Gonzalez-Tudela, D. Martin-Cano, E. Moreno, L. Martín-Moreno, C. Tejedor, and F. J. Garcia-Vidal. Entanglement of two qubits mediated by one-dimensional plasmonic waveguides. *Phys. Rev. Lett.*, 106:020501, 2011.

[23] A. F. van Loo, A. Fedorov, K. Lalumiere, B. C. Sanders, A. Blais, and A. Wallraff. Photon-mediated interactions between distant artificial atoms. *Science*, 342:1494–1496, 2013.

[24] M. H. Devoret and R. J. Schoelkopf. Superconducting circuits for quantum information: An outlook. *Science*, 339:1169–1174, 2013.

[25] J. D. Joannopoulos, R. D. Meade, and J. N. Winn. *Photonic Crystals: Molding the Flow of Light*. Princeton University Press, Singapore, 1995.

[26] E. Yablonovitch. Inhibited spontaneous emission in solid-state physics and electronics. *Phys. Rev. Lett.*, 58:2059, 1987.

[27] S. John. Strong localization of photons in certain disordered dielectric superlattices. *Phys. Rev. Lett.*, 58:2486, 1987.

[28] S. John and J. Wang. Quantum electrodynamics near a photonic band gap: photon bound states and dressed atoms. *Phys. Rev. Lett.*, 64:2418, 1990.

[29] G. Kurizki. Two-atom resonant radiative coupling in photonic band structures. *Phys. Rev. A*, 42:2915, 1990.

[30] J. S. Douglas, H. H. Habibian, C.-L. Hung, A. V. Gorshkov, H. J. Kimble, and D. E. Chang. Quantum many-body models with cold atoms coupled to photonic crystals. *Nat. Photon.*, 9:326–331, 2015.

[31] A. Goban, C.-L. Hung, J. D. Hood, S.-P. Yu, J. A. Muniz, O. Painter, and H. J. Kimble. Superradiance for atoms trapped along a photonic crystal waveguide. *Phys. Rev. Lett.*, 115:063601, 2015.

[32] A. Goban, C.-L. Hung, S.-P. Yu, J. D. Hood, J. A. Muniz, J. H. Lee, M. J. Martin, A. C. McClung, K. S. Choi, D. E. Chang, O. Painter, and H. J. Kimble. Atom-light interactions in photonic crystals. *Nat. Comm.*, 5:3808, 2014.

[33] S.-P. Yu, J. D. Hood, J. A. Muniz, M. J. Martin, R. Norte, C.-L. Hung, S. M. Meenehan, J. D. Cohen, O. Painter, and H. J. Kimble. Nanowire photonic crystal waveguides for single-atom trapping and strong light-matter interactions. *App. Phys. Lett.*, 104:111103, 2014.

[34] T. Lund-Hansen, S. Stobbe, B. Julsgaard, H. Thyrrstrup, T. Sünder, M. Kamp, A. Forchel, and P. Lodahl. Experimental realization of highly efficient broadband coupling of single quantum dots to a photonic crystal waveguide. *Phys. Rev. Lett.*, 101:113903, 2008.

[35] A. B. Young, A. C. T. Thijssen, D. M. Beggs, P. Androvitsaneas, L. Kuipers, J. G. Rarity, S. Hughes, and R. Oulton. Polarization engineering in photonic crystal waveguides for spin-

photon entanglers. *Phys. Rev. Lett.*, 115:153901, 2015.

[36] J. D. Hood, A. Goban, A. Asenjo-Garcia, M. Lu, S.-P. Yu, D. E. Chang, and H. J. Kimble, arXiv:1603.02771.

[37] Y. Liu and A. A. Houck, arXiv:1603.02998.

[38] P. Meystre and M. Sargent. *Elements of Quantum Optics*. Springer-Verlag, Berlin, 2007.

[39] J.-T. Shen and S. Fan. Coherent photon transport from spontaneous emission in one-dimensional waveguides. *Opt. Lett.*, 30:2001, 2005.

[40] T. Gruner and D.-G. Welsch. Green-function approach to the radiation-field quantization for homogeneous and inhomogeneous Kramers-Kronig dielectrics. *Phys. Rev. A*, 53:1818, 1996.

[41] H. T. Dung, L. Knöll, and D.-G. Welsch. Resonant dipole-dipole interaction in the presence of dispersing and absorbing surroundings. *Phys. Rev. A*, 66:063810, 2002.

[42] S. Y. Buhmann and D.-G. Welsch. Dispersion forces in macroscopic quantum electrodynamics. *Prog. Quantum Electron.*, 31:51, 2007.

[43] D. Dzotsjan, A. S. Sørensen, and M. Fleischhauer. Quantum emitters coupled to surface plasmons of a nanowire: A Green's function approach. *Phys. Rev. B*, 82:075427, 2010.

[44] S. Y. Buhmann. *Dispersion forces I*. Springer-Verlag, Berlin, 2012.

[45] M. S. Tomaš. Green function for multilayers: light scattering in planar cavities. *Phys. Rev. A*, 51:2545–2559, 1995.

[46] V. V. Klimov and M. Ducloy. Spontaneous emission rate of an excited atom placed near a nanofiber. *Phys. Rev. A*, 69:013812, 2004.

[47] F. Le Kien, S. D. Gupta, V. I. Balykin, and K. Hakuta. Spontaneous emission of a cesium atom near a nanofiber: efficient coupling of light to guided modes. *Phys. Rev. A*, 72:032509, 2005.

[48] N. A. R. Bhat and J. E. Sipe. Hamiltonian treatment of the electromagnetic field in dispersive and absorptive structured media. *Phys. Rev. A*, 73:063808, 2006.

[49] L. Novotny and B. Hecht. *Principles of Nano-Optics*. Cambridge University Press, New York, 2006.

[50] D. E. Chang, L. Jiang, A. V. Gorshkov, and H. J. Kimble. Cavity QED with atomic mirrors. *New J. Phys.*, 14:063003, 2012.

[51] D. E. Chang, K. Sinha, J. M. Taylor, and H. J. Kimble. Trapping atoms using nanoscale quantum vacuum forces. *Nat. Comm.*, 5:4343, 2014.

[52] T. Caneva, M. T. Manzoni, T. Shi, J. S. Douglas, J. I. Cirac, and D. E. Chang. Quantum dynamics of propagating photons with strong interactions: a generalized input-output formalism. *New J. Phys.*, 17:113001, 2015.

[53] S. Xu and S. Fan. Input-output formalism for few-photon transport: A systematic treatment beyond two photons. *Phys. Rev. A*, 91:043845, 2015.

[54] R. A. Horn and C. R. Johnson. *Matrix analysis*. Cambridge University Press, New York, 2013.

[55] A. E. Siegman. *Lasers*. University Science Books, Sausalito, CA, 1986.

[56] M. V. Berry. Physics of nonhermitian degeneracies. *Czech. J. Phys.*, 54:1039, 2004.

[57] M. V. Berry. Mode degeneracies and the petermann excess-noise factor for unstable lasers. *J. Mod. Opt.*, 50:63–81, 2003.

[58] D. Politzer. The plucked string: An example of non-normal dynamics. *Am. J. Phys.*, 83:395, 2015.

[59] U. Fano. Some theoretical considerations on anomalous diffraction gratings. *Phys. Rev.*, 50:573–573, 1936.

[60] T. Hümmer, F. J. García-Vidal, L. Martín-Moreno, and D. Zueco. Weak and strong coupling regimes in plasmonic QED. *Phys. Rev. B*, 87:115419, 2013.

[61] S. Noschese, L. Pasquini, and L. Reichel. Tridiagonal Toeplitz matrices: properties and novel applications. *Numer. Linear Algebra Appl.*, 20:302, 2013.

[62] T. K. Paraíso, M. Kalae, L. Zang, H. Pfeiffer, F. Marquardt, and O. Painter. Position-squared coupling in a tunable photonic crystal optomechanical cavity. *Phys. Rev. X*, 5:041024, 2015.

[63] I. Aharonovich, A. D. Greentree, and S. Prawer. Diamond photonics. *Nat. Photon.*, 5:397, 2011.

[64] T. Zhong, J. M. Kinder, E. Miyazono, and A. Faraon. Nanophotonic coherent light-matter interfaces based on rare-earth-doped crystals. *Nat. Commun.*, 6:8206, 2015.

Quantum spin dynamics with pairwise-tunable, long-range interactions

C.-L. Hung^{a,b,1,2}, Alejandro González-Tudela^{c,1,2}, J. Ignacio Cirac^c, and H. J. Kimble^{c,d,e,2}

^aDepartment of Physics and Astronomy, Purdue University, West Lafayette, IN 47907; ^bPurdue Quantum Center, Purdue University, West Lafayette, IN 47907;

^cMax-Planck-Institut für Quantenoptik, 85748 Garching, Germany; ^dNorman Bridge Laboratory of Physics, California Institute of Technology, Pasadena, CA 91125; and ^eInstitute for Quantum Information and Matter, California Institute of Technology, Pasadena, CA 91125

Contributed by H. Jeffrey Kimble, June 19, 2016 (sent for review March 6, 2016; reviewed by Nathan Goldman and Ana Maria Rey)

We present a platform for the simulation of quantum magnetism with full control of interactions between pairs of spins at arbitrary distances in 1D and 2D lattices. In our scheme, two internal atomic states represent a pseudospin for atoms trapped within a photonic crystal waveguide (PCW). With the atomic transition frequency aligned inside a band gap of the PCW, virtual photons mediate coherent spin–spin interactions between lattice sites. To obtain full control of interaction coefficients at arbitrary atom–atom separations, ground-state energy shifts are introduced as a function of distance across the PCW. In conjunction with auxiliary pump fields, spin–exchange versus atom–atom separation can be engineered with arbitrary magnitude and phase, and arranged to introduce nontrivial Berry phases in the spin lattice, thus opening new avenues for realizing topological spin models. We illustrate the broad applicability of our scheme by explicit construction for several well-known spin models.

nanophotonics | quantum matter | cold atoms | quantum many-body | quantum spin

Quantum simulation has become an important theme for research in contemporary physics (1). A quantum simulator consists of quantum particles (e.g., neutral atoms) that interact by way of a variety of processes, such as atomic collisions. Such processes typically lead to short-range, nearest-neighbor interactions (2–6). Alternative approaches for quantum simulation use dipolar quantum gases (7, 8), polar molecules (9–11), and Rydberg atoms (12–15), leading to interactions that typically scale as $1/r^3$, where r is the interparticle separation. For trapped ion quantum simulators (16–20), tunability in a power law scaling of $r^{-\eta}$ with $0 < \eta < 3$ can in principle be achieved. Beyond simple power law scaling, it is also possible to engineer arbitrary long-range interactions mediated by the collective phonon modes, which can be achieved by independent Raman addressing on individual ions (21).

Using photons to mediate controllable long-range interactions between isolated quantum systems presents yet another approach for assembling quantum simulators (22). Recent successful approaches include coupling ultracold atoms to a driven photonic mode in a conventional mirror cavity, thereby creating quantum many-body models (using atomic external degrees of freedom) with cavity-field-mediated infinite-range interactions (23). Finite-range and spatially disordered interactions can be realized by using multimode cavities (24). Recent demonstrations on coupling cold atoms to guided mode photons in photonic crystal waveguides (25, 26) and cavities (27, 28) present promising avenues (using atomic internal degrees of freedom) due to unprecedented strong atom–photon coupling rate and scalability. Related efforts also exist for coupling solid-state quantum emitters, such as quantum dots (29, 30) and diamond nitrogen-vacancy centers (31, 32), to photonic crystals. Scaling to a many-body quantum simulator based on solid-state systems, however, still remains elusive. Successful implementations can be found in the microwave domain, where superconducting qubits behave as artificial atoms strongly coupled to microwave photons propagating in a network formed by superconducting resonators and transmission lines (33–35).

Here, we propose and analyze a physical platform for simulating long-range quantum magnetism in which full control is achieved for the spin–exchange coefficient between a pair of spins at arbitrary distances in 1D and 2D lattices. The enabling platform, as described in refs. 36 and 37, is trapped atoms within photonic crystal waveguides (PCWs), with atom–atom interactions mediated by photons of the guided modes (GMs) in the PCWs. As illustrated in Fig. 1A and B, single atoms are localized within unit cells of the PCWs in 1D and 2D periodic dielectric structures. At each site, two internal atomic states are treated as pseudospin states, with spin-1/2 considered here for definiteness (e.g., states $|g\rangle$ and $|s\rangle$ in Fig. 1C).

Our scheme uses strong, and coherent atom–photon interactions inside a photonic band gap (36–40), and long-range transport property of GM photons for the exploration of a large class of quantum magnetism. This is contrary to conventional hybrid schemes based on, for example, arrays of high finesse cavities (41–44) in which the pseudospin acquires only the nearest (or at most the next-nearest) neighbor interactions due to strong exponential suppression of photonic wave packet beyond single cavities.

In its original form (36–40), the localization of pseudospin is effectively controlled by single-atom defect cavities (36). The cavity mode function can be adjusted to extend over long distances within the PCWs, thereby permitting long-range spin exchange interactions. The interaction can also be tuned dynamically, via external addressing beams, to induce complex long-range spin transport, which we describe in the following (36, 37).

To engineer tunable, long-range spin Hamiltonians, we use an atomic Λ scheme and two-photon Raman transitions, where an atom flips its spin state by scattering one photon from an external pump field into the GMs of a PCW. The GM photon then propagates within the waveguide, inducing spin flip in an atom located at a

Significance

Cold atoms trapped along a photonic crystal waveguide can be used to simulate long-range quantum magnetism with pairwise-tunable spin–spin interactions mediated by guided virtual photons in a photonic band gap. Using a two-photon Raman addressing scheme, the proposed atom-nanophotonic system can achieve arbitrary and dynamic control on the strength, phase, and length scale of spin interactions. This promises new avenues for engineering a large class of spin Hamiltonians, including those exhibiting topological order or frustrated long-range magnetism.

Author contributions: C.-L.H. developed concept and analytical calculations; C.-L.H., A.G.-T., J.I.C., and H.J.K. performed research; C.-L.H., A.G.-T., J.I.C., and H.J.K. contributed materials; A.G.-T. performed analytical and numerical analysis; and C.-L.H., A.G.-T., and H.J.K. wrote the paper.

Reviewers: N.G., Université libre de Bruxelles; and A.M.R., JILA, University of Colorado. The authors declare no conflict of interest.

Freely available online through the PNAS open access option.

¹C.-L.H. and A.G.-T. contributed equally to this work.

²To whom correspondence may be addressed. Email: hjkimble@caltech.edu, chhung@purdue.edu, or alejandro.gonzalez-tudela@mpq.mpg.de.

This article contains supporting information online at www.pnas.org/lookup/suppl/doi:10.1073/pnas.1603777113/DCSupplemental.

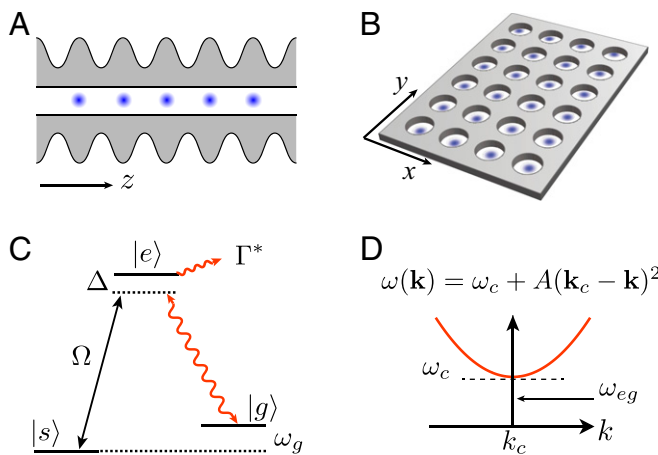


Fig. 1. Photon-mediated atom-atom interactions in (A) 1D and (B) 2D PCWs. (C) Atomic-level scheme: atomic dipole $|s\rangle \leftrightarrow |e\rangle$ is coupled to an external pump, $|g\rangle \leftrightarrow |e\rangle$ coupled to a GM photon, and Γ^* , the excited state decay rate to free space and leaky modes.[†] (D) Simplified band structure $\omega(\mathbf{k})$ near the band edge $\mathbf{k} = \mathbf{k}_c$ and $\omega(\mathbf{k}_c) = \omega_c$. Atomic transition frequency $\omega_{eg} = \omega_e - \omega_g$ lies within the band gap.

distant site via the reverse two-photon Raman process. When we align the atomic resonant frequency inside the photonic band gap, as depicted in Fig. 1D, only virtual photons can mediate this remote spin exchange and the GM dynamics are fully coherent, effectively creating a spin Hamiltonian with long-range interactions. As discussed in refs. 36 and 37, the overall strength and length scale of the spin-exchange coefficients can be tuned by an external pump field, albeit within the constraints set by a functional form that depends on the dimensionality and the photonic band structure. These constraints may limit our ability to explore novel quantum phases and nonequilibrium dynamics in various spin models, because many effects display strong dependencies on the functional form of long-range interactions (45–50). It is therefore highly desirable to obtain full control of interactions without the need to investigate over a wide range of PCW designs with different photonic band structures.

To fully control spin-exchange coefficients at arbitrary separations, here we adopt a Raman-addressing scheme similarly discussed for cold atoms and trapped ions (51–55). We introduce atomic ground-state energy shifts as a function of distance across the PCW. Due to conservation of energy, these shifts suppress reverse two-photon Raman processes in the original scheme (36, 37), forbidding spin exchange within the entire PCW. However, we can selectively activate certain spin-exchange interactions $J(r_{m,n})$ between atom pairs (m, n) separated by $r_{m,n}$, by applying an auxiliary sideband whose frequency matches that of the original pump plus the ground-state energy shift between the atom pairs. This allows us to build a prescribed spin Hamiltonian with interaction terms “one by one.” Note that each sideband in a Raman-addressing beam can be easily introduced, for example, by an electro-optical modulator. By introducing multiple sidebands and by controlling their frequencies, amplitudes, and relative phases, we can engineer spin Hamiltonians with arbitrary, complex interaction coefficients $J(r_{m,n})$. Depending on the dimensionality and the type of spin Hamiltonians, our scheme requires only one or a few Raman beams to generate the desired interactions. Furthermore, by properly choosing the propagation phases of the Raman beams, we can imprint geometric phases in the spin system, thus providing unique opportunities for realizing topological spin models.

We substantiate the broad applicability of our methods by explicit elaboration of the set of pump fields required to realize well-known spin Hamiltonians. For 1D spin chains, we consider the implementation of the Haldane–Shastry model (56, 57). For 2D spin lattices, we elaborate the configurations for realizing topological flat bands (58, 59) in Haldane’s spin model (56), as well as a “checkerboard” chiral-flux lattice (58, 59). We also consider a 2D XXZ spin Hamiltonian with $J(r_{m,n}) \propto 1/r_{m,n}^\eta$ and

$\eta = 1, 2, 3$ (60). In addition, we report numerical results on the η dependence of its magnetization diagram.

Controlling Spin–Spin Interaction Through Multifrequency Driving

In the following, we discuss how to achieve full control of interactions by multifrequency pump fields. We assume (i) N atoms trapped in either a 1D or 2D PCW, as depicted in Fig. 1A and B, with a spatially dependent ground-state energy shift ω_g . For simplicity, we assume one atom per unit cell of the PCW, although this assumption can be relaxed afterward; (ii) the structure is engineered (22–28) such that the GM polarization is coupled to the atomic dipole, $|g\rangle \leftrightarrow |e\rangle$, as shown in Fig. 1C, and, under rotating wave approximation, is described by the following Hamiltonian (using $\hbar = 1$):

$$H_{\text{Im}} = \sum_{\mathbf{k}, n} g_{\mathbf{k}}(\mathbf{r}_n) a_{\mathbf{k}} \sigma_{eg}^n + \text{h.c.}, \quad [1]$$

where $g_{\mathbf{k}}(\mathbf{r}_n) = g_{\mathbf{k}} e^{i\mathbf{k} \cdot \mathbf{r}_n}$ is the single-photon coupling constant at site location \mathbf{r}_n , with n being the site index; $a_{\mathbf{k}}$, the GM field operator; and $\sigma_{ab}^n \equiv |a\rangle_n \langle b|$, the atomic operators with a, b being one of the g, s, e states. Moreover, as in refs. 36 and 37, we assume (iii) there is another hyperfine level $|s\rangle$, addressed by a Raman field with coupling strength Ω as follows:

$$H_{\text{d}}(t) = \sum_n \left(\frac{\Omega(t)}{2} \sigma_{se}^n e^{i\omega_L t} + \text{h.c.} \right), \quad [2]$$

where ω_L is the main driving frequency. The Raman field $\Omega(t)$ contains m_p frequency components that are introduced to achieve full control of the final effective spin Hamiltonian. Full dependence of $\Omega(t)$ can be written as follows:

$$\Omega(t) \equiv \sum_{\alpha=0}^{m_p-1} \Omega_{\alpha} e^{i\tilde{\omega}_{\alpha} t}, \quad [3]$$

where $\tilde{\omega}_{\alpha}$ are the detunings of the sidebands from the main frequency ω_L such that $\tilde{\omega}_0 = 0$, and Ω_{α} , the complex amplitudes.

We can adiabatically eliminate the excited states $|e\rangle$ and the photonic GMs under the condition that (iv) $\max\{|\Omega|, |\tilde{\omega}_{\alpha} - \tilde{\omega}_{\beta}|\} \ll |\Delta| = |\omega_e - \omega_L|$. This condition guarantees that, first, the excited state is only virtually populated, and that, second, the time dependence induced by the sideband driving is approximately constant over the timescale Δ^{-1} . As discussed in refs. 36 and 37, if $\omega_L - \omega_g$ lies in the photonic band gap, photon-mediated interactions by GMs are purely coherent.[†] Under the Born–Markov approximation, we then arrive at an effective XY Hamiltonian (*SI Appendix A: Complete Derivation of Final Time-Dependent Hamiltonian*):

$$H_{XY}(t) = \sum_{m, n \neq m}^N \sum_{\alpha, \beta=0}^{m_p-1} X_{\alpha} X_{\beta} \tilde{J}(\mathbf{r}_{m,n}) e^{i(\omega_{g,m} - \omega_{g,n} + \tilde{\omega}_{\alpha} - \tilde{\omega}_{\beta})t} \sigma_{gs}^m \sigma_{sg}^n, \quad [4]$$

where we have defined $X_{\alpha} = \Omega_{\alpha}/(2\Delta)$; $\omega_{g,n} = \omega_g(\mathbf{r}_n)$ is the site-dependent ground-state energy shift, and $\tilde{J}(\mathbf{r}_{m,n})$ is the atom–GM photon coupling strength (36, 37) that typically depends on atomic separation $\mathbf{r}_{m,n} = \mathbf{r}_m - \mathbf{r}_n$.

We focus on “sideband engineering” and treat $\tilde{J}(\mathbf{r}_{m,n})$ as approximately constant over atomic separations considered.[‡] This is valid as long as the farthest atomic separation with nonzero engineered interaction is much smaller than the decay length

[†]To simplify the discussion, in this paper, we neglect decoherence effects caused by atomic emission into free space and leaky modes as well as photon loss due to imperfections in the PCW. These effects were both carefully discussed in refs. 36 and 37, suggesting the number of spin-exchange cycles in the presence of decoherence can realistically reach $\mathcal{N} \approx 35 \sim 100$ using ultra-high Q PCWs.

[‡]One may also replace a PCW with a single-mode nanophotonic cavity, operating in the strong dispersive regime (61, 62), to achieve constant GM coupling \tilde{J} independent of $|\mathbf{r}_{m,n}|$. Realistic nanophotonic cavity implementations will be considered elsewhere.

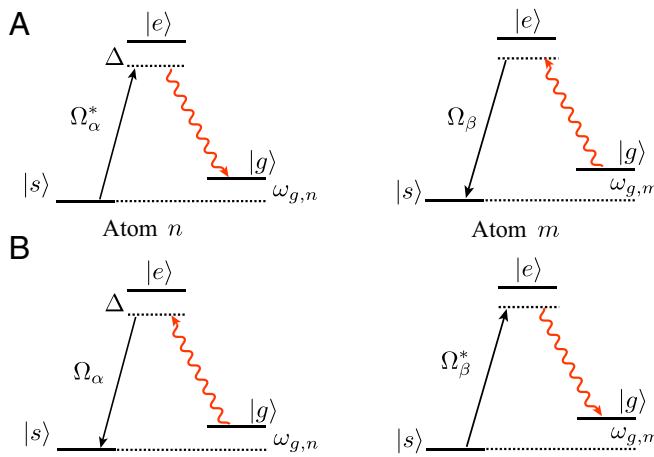


Fig. 2. Schematics to engineer long-range spin exchange interactions via resonant Raman-scattering processes. Spin exchanges (A) $|s_n, g_m\rangle \rightarrow |g_n, s_m\rangle$ and (B) $|g_n, s_m\rangle \rightarrow |s_n, g_m\rangle$ are allowed only when the condition $\omega_{g,m} - \omega_{g,n} = \tilde{\omega}_\beta - \tilde{\omega}_\alpha$ is satisfied. Ω_α/Δ and Ω_β/Δ control the exchange rate.

scale $\xi = \sqrt{|A/\Delta_c|}$ of the coupling strength $\tilde{J}(\mathbf{r}_{m,n})$. Here, A is the band curvature (Fig. 1D), $\Delta_c = \max\{\omega_c - (\omega_L - \omega_{g,n})\}$ is the maximal detuning of the band edge to the frequency of coupled virtual photons that mediate interactions (Fig. 1C), and we have assumed that the variation of ground-state energies $\omega_{g,n}$ are small compared with Δ_c . Exact functional form of $\tilde{J}(\mathbf{r}_{m,n})$ can be found in refs. 36 and 37, and in *SI Appendix A: Complete Derivation of Final Time-Dependent Hamiltonian*.

The time dependence in Eq. 4 can be further engineered and simplified. We note that the interaction between two atoms n and m will be highly dependent on the resonant condition $\omega_{g,m} - \omega_{g,n} = \tilde{\omega}_\beta - \tilde{\omega}_\alpha$, provided the ground-state energy difference $|\omega_{g,n} - \omega_{g,m}|$ is much larger than the characteristic timescale of interactions $|X_\alpha X_\beta^* \tilde{J}|$. The intuitive picture is depicted in Fig. 2A: the atom n scatters from sideband α a photon with energy $\omega_L + \tilde{\omega}_\alpha - \omega_{g,n}$ into the GMs. When this GM photon propagates to the atom m , it will only be rescattered into a sideband β that satisfies $\omega_L + \tilde{\omega}_\alpha - \omega_{g,n} = \omega_L + \tilde{\omega}_\beta - \omega_{g,m}$, whereas the rest of the sidebands remain off-resonant. Fig. 2B depicts a reversed process.

For concreteness, we discuss a 1D case where we assume (v) a linear gradient in the ground-state energy $\omega_{g,n} \equiv n\delta$, with δ being the energy difference between adjacent sites. The sidebands will be chosen accordingly such that $\tilde{\omega}_\alpha = \alpha\delta$, with $\alpha \in \mathbb{Z}$.

Summing up, with all these assumptions (i–v), the resulting effective Hamiltonian Eq. 4 can finally be rewritten as follows:

$$H_{XY}(t) = \sum_p H_{XY,p} e^{ip\delta t}, \quad [5]$$

where $H_{XY,p}$ is the contribution that oscillates with frequency $p\delta$. Written explicitly,

$$H_{XY,p} = \sum_{m,n \neq m} \sum_{\alpha,\beta=0}^{m_p-1} X_\alpha X_\beta^* \tilde{J} \delta_{n-m,\beta-\alpha-p} \sigma_{gs}^m \sigma_{sg}^n. \quad [6]$$

In an ideal situation, the gradient per site satisfies $\delta \gg |X_\alpha X_\beta^* \tilde{J}|$ such that the contributions from $H_{XY,p} \forall p \neq 0$ can be neglected. Under these assumptions, we arrive at an effective time-independent Hamiltonian:

$$H_{XY}(t) \approx H_{XY,0} = \sum_{m,n \neq m}^N J_{m,n} \sigma_{gs}^m \sigma_{sg}^n, \quad [7]$$

where couplings $J_{m,n}$ can be tuned by adjusting the amplitudes and phases of the sidebands X_α as they are given by the following:

$$J_{m,n} = \sum_{\alpha,\beta=0}^{m_p-1} X_\alpha X_\beta^* \tilde{J} \delta_{n-m,\beta-\alpha}. \quad [8]$$

It can be shown that the set of equations defined by Eq. 8 has at least one solution for any arbitrary choice of $J_{m,n}$, that is, by choosing $\Omega_0 \gg \Omega_{\alpha \neq 0}$ and $J_{m,n} \approx (X_0 X_{n-m}^* + X_0^* X_{m-n}) \tilde{J}$. More solutions can be found by directly solving the set of nonlinear equations Eq. 8.

It is important to highlight that multifrequency driving also enables the possibility to engineer geometrical phases and, therefore, topological spin models. If the pump field propagation is not perfectly transverse, that is, $\mathbf{k}_L \cdot \mathbf{r}_{m(n)} \neq 0$ (\mathbf{k}_L being the wave vector of the Raman field), the effective Hamiltonian Eq. 7 acquires spatial-dependent, complex spin-exchange coefficients via the phase of $X_\alpha X_\beta^*$ in Eq. 8; see later discussions.

Beyond an ideal setting, we now stress a few potential error sources. First, for practical situations, the gradient per site δ will be a limited resource, making Eq. 7 not an ideal approximation. Careful Floquet analysis on time-dependent Hamiltonian in Eqs. 5 and 6 is required, to be discussed later. Second, there is an additional Stark shift on state $|s\rangle$ due to the Raman fields:

$$\delta\omega_s(t) = - \sum_{\alpha=0}^{m_p-1} \frac{|\Omega_\alpha|^2}{4\Delta} - \sum_{\alpha>\beta}^{m_p-1} \Re \left[\frac{\Omega_\alpha \Omega_\beta^*}{2\Delta} e^{i(\tilde{\omega}_\alpha - \tilde{\omega}_\beta)t} \right], \quad [9]$$

where $\Re[\cdot]$ indicates real part. We note that the time-independent contribution in Eq. 9 can be absorbed into the energy of ω_s without significant contribution to the dynamics, whereas the time-dependent terms may be averaged out over the atomic timescales that we are interested in. We will present strategies for optimizing the choice of δ , and minimizing detrimental effects due to undesired time-dependent terms in Eqs. 5 and 9 in later discussions.

Independent Control of XX and YY Interactions. So far, we can fully engineer an XY Hamiltonian with equal weight between XX and YY terms by defining the Pauli operators $(\sigma_x, \sigma_y, \sigma_z) = (\sigma_{sg} + \sigma_{gs}, i(\sigma_{sg} - \sigma_{gs}), \sigma_{gg} - \sigma_{ss})$. We now show flexible control of XX and YY interactions with slight modifications in the atomic level structure and the Raman-addressing scheme. In particular, we use a butterfly-like level structure where there are two transitions, $|g\rangle \leftrightarrow |e\rangle$ and $|s\rangle \leftrightarrow |\tilde{e}\rangle$, coupled to the same GM, as depicted in Fig. 3. We will use two multifrequency Raman pump fields, $\Omega_g(t)$ and $\Omega_s(t)$, to induce $|g\rangle \leftrightarrow |\tilde{e}\rangle \leftrightarrow |s\rangle$ and $|s\rangle \leftrightarrow |e\rangle \leftrightarrow |g\rangle$ two-photon Raman transitions, respectively.

For example, to control XX or YY interactions, we require that the two pump fields induce spin flips with equal amplitude, that is, $\sigma_{gs} \pm \sigma_{sg}$. This is possible if we choose the main frequencies of the pumps ($\omega_{L,g}$ and $\omega_{L,s}$) such that $\omega_{L,s} = \omega_{L,g} + 2\omega_g$, and match their amplitudes such that $|\Omega_{g,a}|/\Delta_g = |\Omega_{s,a}|/\Delta_s$, where $\Delta_s = \omega_e - \omega_{L,s}$, $\Delta_g = \omega_e - (\omega_{L,g} + \omega_g)$, and $|\Delta_{s,g}| \gg |\Delta_{s,g}|$.

Adiabatically eliminating the excited states as well as the GMs, we arrive at the following Hamiltonian:

$$H_{XX,YY,0} = \sum_{m,n>m}^N \left[J_{m,n} \left(\sigma_{gs}^m + e^{i\phi_{gs}} \sigma_{sg}^m \right) \left(\sigma_{sg}^n + e^{-i\phi_{gs}} \sigma_{gs}^n \right) + \text{h.c.} \right], \quad [10]$$

where ϕ_{gs} is the relative phase between the pumps fields $\Omega_{g,s}$. Assuming the laser beams that generate the Raman fields are copropagating or are both illuminating the atoms transversely, that is, $\mathbf{k}_L \cdot \mathbf{r}_{m,n} = 0$, we can generate either X or Y components, $(\sigma_{sg}^m \pm \sigma_{gs}^m)$, by setting the phase $\phi_{gs} = 0$ or π ; more exotic combinations are available with generic choice of ϕ_{gs} . Moreover, if the laser beams are not copropagating, they create spatially dependent phases $\phi_{gs,m}$. This can create site-dependent XX , YY , or XY terms.

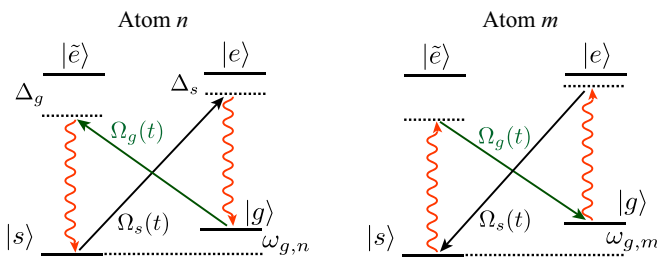


Fig. 3. Atomic “butterfly” level structure. Two pump fields Ω_s and Ω_g , tuned to couple to the same GM photon, are introduced to control XX and YY interactions independently.

Independent Control of ZZ Interactions. An independently controlled ZZ Hamiltonian, in combination with arbitrary XY terms, would allow us to engineer SU(2)-invariant spin models as well as a large class of XXZ models, that is, the following:

$$H_{XXZ} = H_{XY} + H_{ZZ} = \sum_{m,n>m}^N \left[\left(2J_{m,n}^{xy} \sigma_{gs}^m \sigma_{sg}^n + \text{h.c.} \right) + J_{m,n}^z \sigma_z^m \sigma_z^n \right]. \quad [11]$$

In refs. 36 and 37, it was shown that ZZ interaction can be created by adding an extra pump field to the $|g\rangle \leftrightarrow |e\rangle$ transition in Fig. 1C. However, as ZZ terms in this scheme (36, 37) do not involve flipping atomic states, it is not directly applicable to our multifrequency pump method. Nonetheless, because we can generate XX and YY interactions independently, a straightforward scheme to engineer H_{ZZ} is to use single qubit rotations to rotate the spin coordinates $X \leftrightarrow Z$ or $Y \leftrightarrow Z$, followed by stroboscopic evolutions (63) to engineer the full-spin Hamiltonian. Spin-rotation can be realized, for example, with a collective microwave driving $H_{\text{mw}} = \sum_n ((\Omega_{\text{mw}}/2) \sigma_{sg}^n + \text{h.c.})$, in

which a $\pi/2$ -microwave pulse rotates the basis $\{|g\rangle_n, |s\rangle_n\} \rightarrow \{(|g\rangle_n + |s\rangle_n)/\sqrt{2}, (|g\rangle_n - |s\rangle_n)/\sqrt{2}\}$.

Thus, an H_{XXZ} Hamiltonian can be simulated using the following stroboscopic evolution: $\{H_{XY}, H_{ZZ}, H_{XY}, H_{ZZ}, \dots\}$ in N_t steps as schematically depicted in Fig. 4. As shown in *SI Appendix A: Complete Derivation of Final Time-Dependent Hamiltonian*, the error accumulated in these N_t steps can be bounded by the following:

$$E_2 \leq \frac{N(RIt)^2}{N_t}, \quad [12]$$

where $J = \max[J_{m,n}]$ is the largest energy scale of the Hamiltonian we want to simulate, and R is the approximate number of atoms coupled through the interaction. For example, if $J_{m,n}$ is a nearest-neighbor interaction, $R = 1$. If $J_{m,n} \propto 1/|m-n|^\eta$, then $R \propto \sum_{n=1}^N 1/|n|^\eta$, which typically grows much slower than N . Because $E_2 \propto 1/N_t$, the Trotter error in N_t steps can in principle be decreased to a given accuracy ε by using enough steps, that is, $N_t \geq (N(RIt)^2)/\varepsilon$.

More complicated stroboscopic evolutions may lead to a more favorable error scaling (64–66), although in real experiments there will be a trade-off between minimizing the Trotter error and the fidelity of the individual operations to achieve H_{XY} and H_{ZZ} . As this will depend on the particular experimental setup, we will leave such analysis out of current discussions. For illustration, we will only consider the simplest kind of stroboscopic evolution that we depicted in Fig. 4.

Engineering Spin Hamiltonians for 1D Systems: The Haldane–Shastry $S=1/2$ Spin Chain

In the first example, we engineer a Haldane–Shastry spin Hamiltonian in one dimension (56, 57):

$$H_{\text{HS}} = \sum_{m=1}^{N-1} \sum_{n=1}^{N-m} J_n \left[2 \left(\sigma_{sg}^m \sigma_{gs}^{m+n} + \text{h.c.} \right) + \sigma_z^m \sigma_z^{m+n} \right], \quad [13]$$

where $J_n = J_0 / \sin^2(n\pi/N)$, $J_0 = J\pi^2/N^2$, and N is the number of spins. The interaction strength decays slowly with approximately a $1/r^2$ dependence while satisfying a periodic boundary condition. Such a spin Hamiltonian is difficult to realize in most physical setups that interact, for example, via dipolar interactions.

We can engineer the periodic boundary condition and the long-range interaction J_n directly using a linear array of trapped atoms coupled to a PCW. To achieve this, we induce atomic ground-state energy shift $m\delta$ according to the spin index m , and then uniformly illuminate the trapped atoms with an external pump consisting of N frequency components $\tilde{\omega}_\alpha = \alpha\delta$, each with an amplitude denoted by Ω_α and $\alpha = 0, 1, \dots, N-1$. Regardless of the position of atoms, all pump pairs with frequency difference $n\delta$ contribute to the spin interaction J_n . Considering first the XY terms, and according to Eq. 7, we demand the following:

$$J_n \approx \tilde{J} \sum_{\alpha=0}^{N-n-1} X_\alpha X_{\alpha+n}^* = \frac{J_0}{\sin^2(n\pi/N)}, \quad [14]$$

where \tilde{J} is the GM photon coupling rate (Eq. 8) that we will assume to be a constant for the simplicity of discussions. This requires that the physical size of the spin chain be small compared with the decay length of \tilde{J} . That is, $Nd \ll \xi$, where d is the atomic separation. It is then straightforward to find the required pump amplitudes Ω_α (or equivalently X_α) by solving Eq. 14 for all n . Notice that the system of equations Eq. 14 is overdetermined, and therefore one can find several solutions of it. However, we choose the solution that minimizes the total intensity $\sum |\Omega_\alpha|^2$. Fig. 5 shows that the total intensity converges to a constant value for large N , as a result of decreasing sideband amplitudes for decreasing $1/r^2$ interaction strengths. This is confirmed in Fig. 5 as we see the growth of the ratio between maximum and minimum sideband amplitudes when N increases. The same external pump configuration can also be used to induce the ZZ terms by applying stroboscopic procedures as discussed in the previous section.

Engineering Spin Hamiltonians for 2D Systems: Topological and Frustrated Hamiltonians

In the following, we discuss specific examples for engineering 2D spin Hamiltonians that are topologically nontrivial. In particular, we discuss two chiral-flux lattice models that require long-range

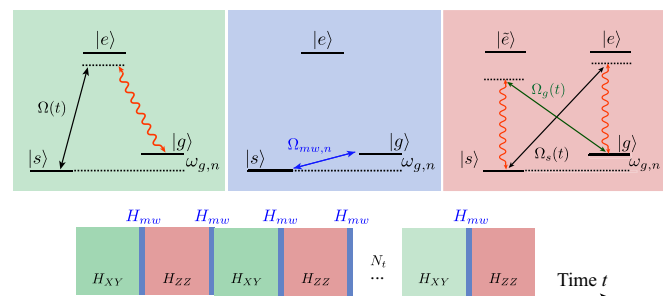


Fig. 4. Scheme for generating an XXZ spin Hamiltonian using a stroboscopic evolution. The scheme contains periodic applications of a multifrequency Raman field to induce the H_{XY} interaction (in green), two fast microwave pulses (or optical two-photon transition) forming H_{mw} that uniformly rotate the spin basis $\{|g\rangle_n, |s\rangle_n\} \rightarrow \{(|g\rangle_n + |s\rangle_n)/\sqrt{2}, (|g\rangle_n - |s\rangle_n)/\sqrt{2}\}$ back and forth (in blue), and a butterfly-like pumping scheme that applies H_{ZZ} in the rotated basis.

hopping terms to engineer single particle flat-bands with nonzero Chern numbers, which are key ingredients to realizing fractional quantum Hall effects (FQHEs) without Landau levels (58, 59).

In recent years, the field of ultracold atoms has made remarkable progress in engineering topological quantum matter. An artificial gauge field (67) has been realized using cold atoms loaded into shaken optical lattices (68, 69) as well as in lattices with laser-induced tunneling (55, 54, 70–72). Various topological models, including Haldane's honeycomb lattice (73, 74), have been successfully implemented. Berry curvature and topological invariants such as the Chern number (74–80) can be measured. Chiral edge currents in synthetic quantum Hall lattices are also observed (81, 82). Most of the demonstrations so far focus on probing topological band structures and single-particle physics. Realizing strongly interacting topological phases such as FQH states, however, still remains elusive. This in part is due to limited topological bandwidth-to-gap ratio, but a number of improved schemes (e.g., refs. 83 and 84) have been proposed.

Coupling cold atoms to mobile PCW photons also allows topological band engineering and band flattening. Moreover, the pseudo spin-1/2 system already interacts like hard-core bosons because individual atoms that participate in the spin-exchange process cannot be doubly excited. With the addition of tunable long-range ZZ interactions, we can readily build many-body systems that should exhibit, for example, FQH and supersolid phases (85), providing a powerful route toward realizing strongly interacting topological phases.

Chiral-Flux Square Lattice Model. The first example discussed here can be mapped to a topological flat-band model similarly described in refs. 58, 59, and 85. The topological spin Hamiltonian is written as follows:

$$\begin{aligned} H_{\text{flat}} &= H_0 + H' \\ H_0 &= t_1 \sum_{\langle m, n \rangle} e^{i\phi_{mn}} \sigma_m^\dagger \sigma_n \pm t_2 \sum_{\langle\langle m, n \rangle\rangle} \sigma_m^\dagger \sigma_n + \text{h.c.} \\ H' &= t_3 \sum_{\langle\langle\langle m, n \rangle\rangle\rangle} \sigma_m^\dagger \sigma_n + \text{h.c.} \end{aligned} \quad [15]$$

in which we define $\sigma_n^\dagger \equiv \sigma_{ng}^m$ and $\sigma_m \equiv \sigma_{gg}^m$, $\langle \cdot \rangle$ denotes nearest neighbors (NN), and t_1 is the coupling coefficient, $\langle \langle \cdot \rangle \rangle$ [$\langle \langle \langle \cdot \rangle \rangle \rangle$] denotes [next]-next-nearest neighbors (NNN) [and NNNN, respectively] with t_2 [t_3] being the respective coupling coefficients. The NN coupling phases $\phi_{mn} = \pm\phi$ are staggered across lattice sites, where the phase factor ϕ is the one that breaks time reversal symmetry for $\phi \neq 0, \pi$ (with $n \in \mathbb{Z}$). Spin exchange between next-nearest neighbors (NNN) has real coefficients $\pm t_2$ with alternating sign along the lattice checkerboard (Fig. 6). One can show that

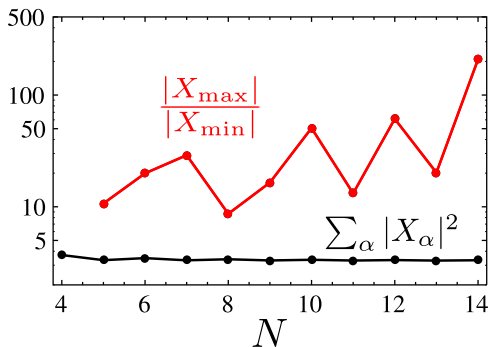


Fig. 5. Sideband amplitude for Haldane-Shastry model: total intensity (black) $\sum_{\alpha} |X_{\alpha}|^2$ and maximum/minimum ratio (red) of sideband amplitudes $|X_{\alpha}|$ as a function of N .

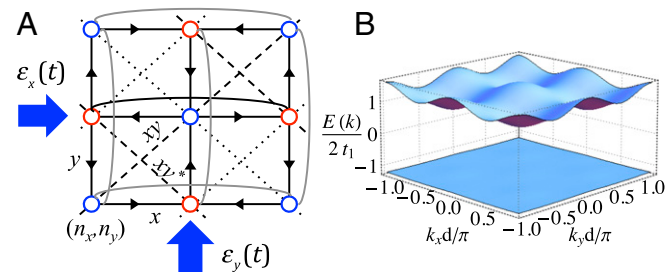


Fig. 6. Engineering a chiral-flux square lattice. (A) Two sublattices ($n_x + n_y$ odd or even) are marked by blue and red circles, respectively. Solid lines mark the NN hopping with phase gain ϕ (arbitrarily tuned) along the direction of the arrows. Dashed (dotted) lines mark the NNN hopping terms (coefficients $\pm t_2$). NNNN long-range hopping along curved lines are included to assist band flattening. Filled arrows indicate the propagation of pump electric fields ε_y and ε_x , respectively; see text. (B) Resulting two-band structure with $(t_2, t_3, \phi) = (t_1/\sqrt{2}, t_1/4\sqrt{6}, \pi/4)$.

already H_0 has a small bandwidth with nontrivial Chern number that, choosing $t_2 = t_1/\sqrt{2}$ and $\phi = \pi/4$, results in a simple band dispersion $E_0(\mathbf{k}) = \pm\sqrt{2t_1\sqrt{3} + \cos(k_x + k_y)\cos(k_x - k_y)}$. Adding H' to H_0 with, for example, $t_3 = 1/4\sqrt{6}t_1$ allows us to engineer an even flatter lower band whose bandwidth is $\sim 1\%$ of the band gap.

We can use an array of atoms trapped within a 2D PCW, as in Fig. 1B, to engineer the Hamiltonian H_{flat} of Eq. 15. For simplicity, we assume that there is one atom per site although this is not a fundamental assumption.[§] As shown in Fig. 6A, we need to engineer spin exchange in four different directions, namely, $\hat{x}, \hat{y}, \hat{x} \pm \hat{y}$. We first introduce linear Zeeman shifts by properly choosing a magnetic field gradient ∇B (*SI Appendix B: Proper Choice of Ground-State Energy Shifts in 2D Models*) such that $\delta_{\alpha} = |\mu_B \nabla B \cdot \Delta \mathbf{r}_{\alpha}|$, where μ_B is the magnetic moment, $\Delta \mathbf{r}_{\alpha}$ are vectors associated with the directions of spin exchange:

$\{\Delta \mathbf{r}_{\alpha}\}_{\alpha=x,y,\hat{x},\hat{y}} = \{d\hat{x}, d\hat{y}, d(\hat{x} + \hat{y}), d(\hat{x} - \hat{y})\}$, and d is the lattice constant. To activate spin exchange along these directions while suppressing all other processes, we consider a simplest case by applying a strong pump field of amplitude Ω_0 (frequency ω_L) to pair with sidebands $|\Omega_{\alpha}| \ll |\Omega_0|$ of detunings $\tilde{\omega}_{\alpha} = \delta_{\alpha}$ to satisfy the resonant conditions. To generate the desired chiral-flux lattice, we need to carefully consider the propagation phases $\mathbf{k}_0 \cdot \mathbf{r}_n$ ($\mathbf{k}_a \cdot \mathbf{r}_n$) of the pump field (and sidebands), where $\mathbf{r}_n = d(n_x \hat{x} + n_y \hat{y})$ is the site coordinate and $n_{x,y} \in \mathbb{Z}$. In the following, we pick $k = k_a = \pi/d$.

We can generate the couplings in H_{flat} , term by term, as follows. **Staggered NN coupling along $\Delta \mathbf{r}_{\alpha=x,y}$.** We consider the strong pump field to be propagating along \hat{y} , that is, $X_0(\mathbf{r}_n) = (|\Omega_0|/2\Delta)e^{-i\eta_y \pi}$. At the NN site $\mathbf{r}_m = \mathbf{r}_n + \Delta \mathbf{r}_x$, it can pair with an auxiliary sideband of detuning $\tilde{\omega}_x = \delta_x = |\mu_B \nabla B \cdot \Delta \mathbf{r}_x|$ with $X_x(\mathbf{r}_m) = (|\Omega_1|/2\Delta)[e^{-i\eta_y \pi} - i\zeta e^{-i(\tilde{n}_x + 1)\pi}]$ to generate coupling along $\Delta \mathbf{r}_x$. The sideband is formed by two field components in $\varepsilon_y(t)$ and $\varepsilon_x(t)$, propagating along \hat{y} and \hat{x} , respectively (Fig. 6), with an amplitude ratio of ζ and with an initial $\pi/2$ phase difference. These two fields are used to independently control real and imaginary parts of the spin-exchange coefficients. Using Eq. 8 under the condition $|\Omega_0| \gg |\Omega_{\alpha}|$, the coupling rate along $\Delta \mathbf{r}_x$ is as follows:

$$J_{m,n} = \tilde{J} X_0 X_x^* = t_1 \frac{[1 - i\zeta(-1)^{n_x - n_y}]}{\sqrt{1 + \zeta^2}} = t_1 e^{\pm i\phi}, \quad [16]$$

where $t_1 = \tilde{J} |X_0| |X_x| \sqrt{1 + \zeta^2}$. This results in the staggered phase pattern with tunable $\phi = \tan^{-1} \zeta$. The NN coupling along $\Delta \mathbf{r}_y$ can

[§]In principle, exact physical separations between trapped atoms do not play a significant role with photon-mediated long-range interactions. One may also engineer the spin Hamiltonian based on atoms sparsely trapped along a photonic crystal, even without specific ordering. It is only necessary to map the underlying symmetry and dimensionality of the desired spin Hamiltonian onto the physical system.

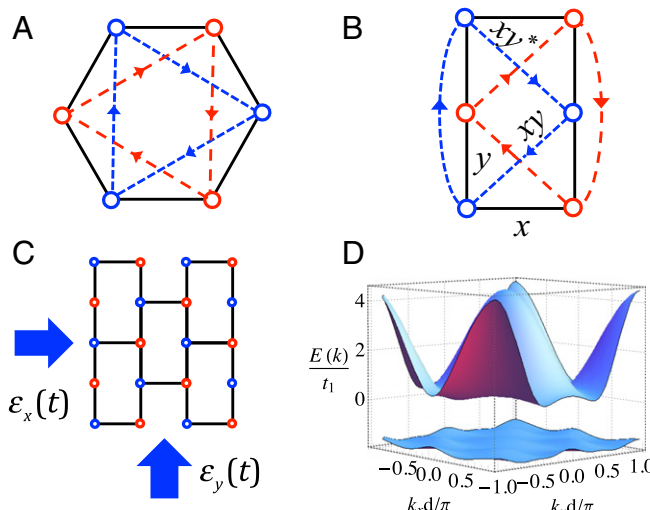


Fig. 7. Engineering a honeycomb-equivalent topological brick wall lattice. (A) Unit cell of a honeycomb lattice. Solid lines mark the NN hopping. Dashed lines mark the NNN hopping with phase gain ϕ along the direction of the arrows. (B) Unit cell of a brick wall lattice. Solid lines indicate the NN hopping as in A. NNNN hopping (curved dashed lines) and NNN hopping (diagonal dashed lines) correspond to the complex NNN hopping in A, making the two models topologically equivalent. (C) Brick wall lattice. Filled arrows illustrate the pump electric fields. (D) Band structure of the brick wall lattice, plotted with $\cos \phi = 3\sqrt{3}/43$ (58).

be introduced via another sideband with detuning $\tilde{\omega}_y = \delta_y = |\mu_B \nabla B \cdot \Delta \mathbf{r}_y|$ and $X_y(\mathbf{r}_n + \Delta \mathbf{r}_y) = -(|\Omega_1|/2\Delta) [e^{-i(n_y+1)\pi} + i\zeta e^{-in_y\pi}]$. **NNN coupling along $\Delta \mathbf{r}_{\alpha=xy,xy^*}$.** The sign of the coefficient depends on the sublattices. To engineer these couplings, we use two sidebands formed by field components in $\varepsilon_x(t)$, with detunings $\delta_{\alpha=xy,xy^*}$ and $X_{\alpha}(\mathbf{r}_n + \Delta \mathbf{r}_{xy,xy^*}) = \pm (|\Omega_2|/2\Delta) e^{-i\alpha(n_x+1)}$ at NNN sites. After pairing with the pump field X_0 at site \mathbf{r}_n , the resulting exchange coefficients are $J_{m,n} = \tilde{J} X_0 X_{\alpha=xy,xy^*}^* = \mp t_2 (-1)^{n_x - n_y}$, forming the required pattern with $t_2 = \tilde{J} |X_0| |X_{xy}|$.

NNNN coupling along $2\Delta \mathbf{r}_{\alpha=x,y^*}$. We use two sidebands $X_{2x,2y} = |\Omega_3| e^{-i\alpha n_y}/2\Delta$, propagating along \hat{y} with detunings $2\delta_{\alpha=x,y^*}$, to introduce the real coupling coefficient $t_3 = \tilde{J} |X_0| |X_{2x}|$.

Summing up, all of the components in the Raman field can be introduced by merely two pump beams propagating along \hat{x} and \hat{y} directions, respectively. In *SI Appendix C: Pump Field Configurations for Engineering a Chiral-Flux Square Lattice Model*, we explicitly write down the time-dependent electric field that contains all of the sidebands.

We note that it is also possible to simultaneously introduce both blue-detuned ($\delta_{\alpha} > 0$) and red-detuned ($\delta_{\alpha} = -\delta_{\alpha}$) sidebands in the Raman field to control the same spin-exchange term. That is, $J_{m,n} = \tilde{J} [X_0(\mathbf{r}_n) X_{\alpha}^*(\mathbf{r}_m) + X_0^*(\mathbf{r}_m) X_{\alpha}(\mathbf{r}_n)]$, which has contributions from X_{α} and $X_{-\alpha}$ of blue and red sidebands, respectively. Arranging both sidebands with equal amplitudes lead to equal contributions in the engineered coupling coefficient. This corresponds to applying amplitude modulations in the pump electric field. In real experiments, amplitude modulation can be achieved by, for example, the combination of acoustic-optical modulators, and optical IQ-modulators.

"Honeycomb"-Equivalent Topological Lattice Model. To further demonstrate the flexibility of the proposed platform, we create Haldane's honeycomb model (73) via a topologically equivalent brick wall lattice (74, 86). Here, we engineer the brick wall configuration using the identical atom-PCW platform discussed in the previous example. Mapping between the two models is illustrated in Fig. 7 A and B, which contains the following two nontrivial steps: (i) generating a checkerboard-like NN-exchange pattern in the \hat{x} direction; (ii) obtaining NNN (along $\Delta \mathbf{r}_{xy,xy^*}$) and

NNNN (along $2\Delta \mathbf{r}_y$) couplings with the same strength and with a coupling phase $\phi_{mn} = \pm\phi$, which alternates sign across two sublattices. Thus, our target Hamiltonian is given by the following:

$$H = t_1 \sum_{\langle m,n \rangle} (\sigma_m^{\dagger} \sigma_n + \text{h.c.}) + t_2 \sum_{\{m,n\}} (e^{i\phi_{mn}} \sigma_m^{\dagger} \sigma_n + \text{h.c.}), \quad [17]$$

where $\langle \cdot \rangle$ denotes NN pairs in the brick wall configuration (Fig. 7) and t_1 is the coupling coefficient. Note that, for simplicity, we discuss a special case where all NN-coupling coefficients from a brick wall vertex are identical. The second summation in Eq. 17 runs over both NNN and NNNN pairs with identical coupling coefficient t_2 and alternating phase $\phi_{mn} = \pm\phi$ (Fig. 7).

As in the previous case, we use a strong pump field (propagating along \hat{y}), as well as several other weak sidebands to generate all necessary spin-exchange terms. Detailed descriptions on engineering individual terms can be found in *SI Appendix D: Pump Field Configurations for Engineering a Topological Spin Model in a Brick Wall Lattice*. The most important ingredient, discussed here, is that we can generate checkerboard-like NN coupling (along \hat{x}), with $J_{m,n} = \tilde{J} X_0 X_{\hat{x}}^* = (t_1/2) [1 - (-1)^{n_x - n_y}]$. This is achieved by using a sideband of detuning δ_x and amplitude $X_x = (|\Omega|/4\Delta) [e^{-in_y\pi} + \zeta e^{-i(n_x+1)\pi}]$ at position $\mathbf{r}_m = \mathbf{r}_n + \Delta \mathbf{r}_x$, formed by two fields propagating along \hat{y} and \hat{x} , respectively. If both fields have the same amplitude ($\zeta = 1$), they either add up or cancel completely depending on whether $n_x - n_y$ is odd or even. If one applies the same trick toward NN coupling along \hat{y} , but with $\zeta \neq 1$, the coupling amplitude modulates spatially in a checkerboard pattern. Essentially, all three NN terms around a brick wall vertex can be independently controlled, opening up further possibilities to engineer, for example, Kitaev's honeycomb lattice model (87, 88).

For physical implementations, again only two pump beams can introduce all components required in the Raman field, which is very similar to the previous case. We stress that, by merely changing the way the Raman field is modulated, one can dynamically adjust the engineered spin Hamiltonians and even the topology, as we compare both cases. This is a unique feature enabled by our capability to fully engineer long-range spin interactions.

Moreover, many of the tricks discussed above can also be implemented in 1D PCWs. It is even possible to engineer a topological 1D spin chain, by exploiting long-range interactions to map out nontrivial connection between spins. For example, our method can readily serve as a realistic approach to realize a topological 1D spin chain as recently proposed in ref. 89.

XXZ Spin Hamiltonian with Tunable Interaction $1/r^n$. In the last example, we highlight the possibility of engineering a large class of XXZ spin Hamiltonians, which were studied extensively in the literature because of the emergence of frustration related phenomena (60, 90–96) and their intriguing nonequilibrium dynamics (45–50). An XXZ Hamiltonian is typically written as follows:

$$H_{XXZ} = -B \sum_n \sigma_n^z + \sum_{n < m} \frac{J}{r_{n,m}^{\eta}} [\cos(\theta) \sigma_n^z \sigma_m^z + \sin(\theta) (\sigma_n^x \sigma_m^x + \sigma_n^y \sigma_m^y)], \quad [18]$$

where an effective magnetic field B controls the number of excitations, $r_{n,m} = |\mathbf{r}_n - \mathbf{r}_m|$, and the parameter θ determines the relative strength between the ZZ and XY interactions. This class of spin models has been previously studied, but mostly restricted to nearest neighbors (90–93) or dipolar ($\eta = 3$) interactions (60, 94, 95).

In our setup, one can simulate XXZ models with arbitrary η by first introducing unique ground-state energy shifts at each of the separation $\mathbf{r}_n - \mathbf{r}_m$, and then applying a strong pump field of amplitude Ω_0 together with N_d auxiliary fields Ω_{α} of different detunings

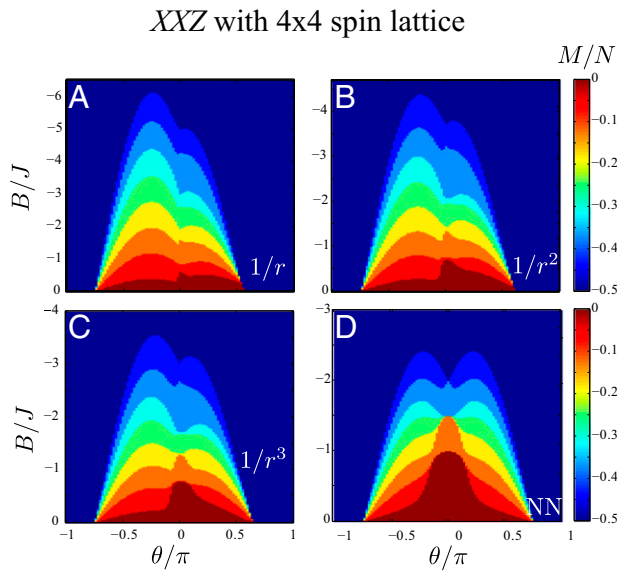


Fig. 8. Mean magnetization M/N for a system with $N=16$ atoms in a square lattice, restricted to $N_{\text{exc}} \leq 8$ excitations and $\eta=1$ (A), 2 (B), 3 (C), and NN couplings (D).

to introduce spin interactions at each separations.[¶] Moreover, the parameter θ that determines the ratio between ZZ and XY interaction can be controlled by using different pump intensities in the stroboscopic steps (*SI Appendix E: PCW and Pump Field Configurations for Engineering an XXZ Spin Hamiltonian with $1/r^\eta$ Interaction*).

To illustrate physics that can emerge in the first experimental setups with only a few atoms, we study the total magnetization of a small square lattice of $n_s \times n_s$ ($=N$) 16 atomic spins. We apply exact diagonalization restricting to $N_{\text{exc}} \leq 8$ excitations for $N=16$ spins and cover one-half of the phase diagram with $B>0$. In Fig. 8, we explore the mean magnetization of the system $M/N = \frac{1}{2} \sum_i \langle \sigma_i^z \rangle / N$ as a function of B and θ for $\eta=1$ (A), 2 (B), 3 (C), and NN couplings (D). At $\theta=0$, the system behaves classically showing the so-called “devil staircase” (97) of insulating states with different rational filling factors and crystalline structures. As already explored in ref. 95 for 1D dipolar systems ($\eta=3$), the presence of long-range interactions, compared with nearest-neighbor models, lead to stronger frustration effects. This manifests in the magnetization diagram with an asymmetry between $\theta \leq 0$. In Fig. 8, we show that longer-range interactions lead to even higher degree of asymmetry. Moreover, in refs. 60 and 95, it was discussed that long-range coupling leads to the formation of supersolid phases, in which crystalline structure and long-range order coexist. These may be even more favored by longer-range interactions. Full characterization of the phases diagram is, however, beyond the scope of this paper and will be discussed elsewhere.

Another especially interesting arena is the behavior of strongly long-range interacting systems (η smaller than the lattice dimension D) under nonequilibrium dynamics. It has recently been predicted to yield “instantaneous” transmission of correlations after a local quench (45, 47, 48, 96), breaking the so-called Lieb-Robinson bound.

Finally, it is interesting to point out that magnetization can be measured by first freezing the interaction (via shutting off the pump lasers) followed by atom number counting using state-dependent fluorescence imaging. Coherence and off-diagonal long-range orders

of the many-body states may be probed via guided photons in another propagation mode along the PCW (98).

Limitations and Error Analysis. Until now, we have mainly focused on how to engineer H_0 in an ideal situation. We neglected spontaneous emission or GM photon losses and considered that the energy gradient (or δ , the ground-state energy difference between nearest neighboring atoms) can be made very large compared with the interaction energy scales that we want to simulate ($|\delta| \gg |J_{m,m+1}|$). Because the effect of finite cooperativities was considered in detail in refs. 36 and 37, and their conclusions translate immediately to our extension to multifrequency pumps, in this work we mainly focus on the effect of finite δ . In addition, we also discuss the effects of AC Stark shifts as in Eq. 9, and its error contributions, together with other possible error sources.

Corrections Introduced from Higher Harmonics: A Floquet Analysis. We discuss errors and the associated error reduction scheme following a Floquet analysis with multifrequency driving (99, 100), applicable mainly to 1D models. Including all of the time-dependent terms in a multifrequency pumping scheme, we have (Eq. 5) $H(t) = \sum_p H_p e^{ip\delta t}$, where H_p represents the part that oscillates at frequency $p\delta$. This Hamiltonian has a period $T=2\pi/\delta$. It can be shown that at integer multiples of T , the observed system should behave as if it is evolving under an effective Hamiltonian[#]:

$$H_{\text{eff},1} \approx H_0 + \frac{1}{\delta} \sum_p \frac{[H_p, H_{-p}]}{p} + \frac{1}{2\delta^2} \sum_p \frac{[[H_p, H_0], H_{-p}] + [[H_{-p}, H_0], H_p]}{p^2}. \quad [19]$$

This means that the leading error in our simple scheme would be on the order of J^2/δ , where J is the simulated interaction strength. However, we note that if $H_p = \pm H_{-p}$, the leading error term $\sum_p [H_p, H_{-p}]/(p\delta)$ should vanish. In other words, first-order error vanishes if H_p is either symmetric or antisymmetric under a time reversal operation \mathcal{T} . Although the original Hamiltonian $H(t)$ does not necessarily possess such symmetry, it is possible to introduce a two-step periodic operation $H_{\text{2step}} = \{H, \mathcal{T}H, H, \mathcal{T}H, \dots\}$ to cancel the first-order error while keeping the time-independent part $H_{\text{2step},0} = H_0$ identical. This results in an effective Hamiltonian in the Floquet picture:

$$H_{\text{eff},2} = H_0 + H_{\text{err},2} \approx H_0 + \frac{4}{\delta^2} \sum_p (-1)^p \frac{[[\tilde{H}_p, H_0], \tilde{H}_p]}{p^2}, \quad [20]$$

where \tilde{H}_p is the (operator) Fourier coefficient of the two-step Hamiltonian and the leading error reduces to the order of J^3/δ^2 .

To achieve the time reversal operation, we must reverse the phase of the driving lasers, as well as the sign of the energy offsets between the atoms. Specifically, we can engineer a periodic two-step Hamiltonian by first making the system evolve under presumed H_0 (along with other time-dependent terms) for a time interval T , and then, for the next time interval T , we flip the sign of the energy gradient, followed by reversing the propagation direction of the Raman fields such that $X_\alpha \rightarrow X_\alpha^*$ in Eq. 5. As a result, all of the time-dependent Hamiltonians $\tilde{H}_p, \forall p \neq 0$, become H_{-p} in the second step, resulting in $\tilde{H}_p = (-1)^p \tilde{H}_{-p}$ required for error reduction; whereas the time-independent Hamiltonian H_0 remains identical in the two-step Hamiltonian. See *SI Appendix F: Error Reduction and Analysis* for more discussions.

[¶]To simulate a square lattice of $n_s \times n_s$ ($=N$) atomic spins, we find that the number of different distances grows as $N_d = (n_s(n_s+1)/2) - 2$, which is linearly proportional to the number of atoms $N_d \propto N$.

[#]When the measurement time is incommensurate with period T , small-amplitude and fast-oscillating spin-dynamics due to time-dependent terms in Eq. 5 manifest as extra errors; see the discussion about micromotion in refs. 99 and 100.

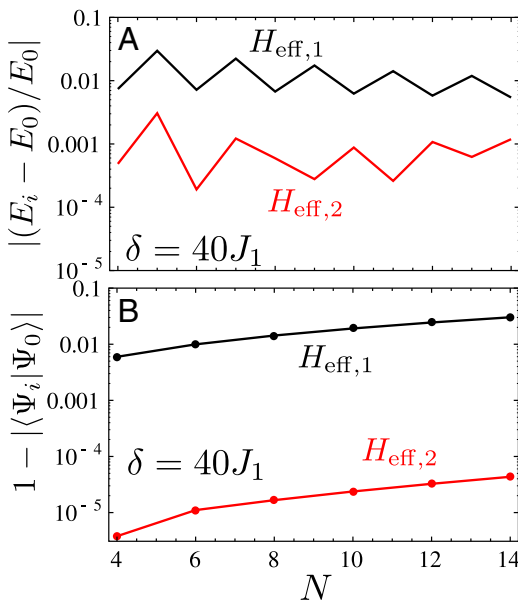


Fig. 9. (A) Comparison of ground-state energy error $|(E_i - E_0)/E_0|$ and (B) ground-state overlap $|\langle \Psi_i | \Psi_0 \rangle|$ as a function of N for Hamiltonians $H_{\text{eff}},1$ (black) and $H_{\text{eff}},2$ (red) with detuning $\delta/J_1 = 40$.

Numerical Analysis on the Haldane–Shastry Spin Chain. We now analyze numerically and discuss error on one particular example. For numerical simplicity, we choose the Haldane–Shastry model as its 1D character makes it numerically more accessible. However, the conclusions regarding the estimation of errors can be mostly extended to other models. As we have shown in Eq. 13, the Haldane–Shastry Hamiltonian is composed by an XY term plus a ZZ term that we can simulate stroboscopically. As we already analyzed the Trotter error due to the stroboscopic evolution, here we focus on the XY part of the Hamiltonian, which reads as follows:

$$H_{\text{HS},xy} = \sum_{m=1}^N \sum_{n=1}^{N-m} \frac{J_0}{\sin^2(n\pi/N)} \left(\sigma_{sg}^m \sigma_{gs}^{m+n} + \sigma_{sg}^{m+n} \sigma_{gs}^m \right), \quad [21]$$

where $J_0 = J\pi^2/N^2$. Following the prescribed engineering steps, the total time-dependent Hamiltonian resulting from multiple sidebands can be written as $H(t) = \sum_p H_p e^{ip\delta t}$, with the following:

$$H_p = \sum_{m=1}^N \sum_{n=1}^{N-m} \left(J_{n,(p)} \sigma_{sg}^m \sigma_{gs}^{m+n} + J_{n,(-p)}^* \sigma_{sg}^{m+n} \sigma_{gs}^m \right), \quad [22]$$

and we have defined $J_{n,(p)} = \sum_{\alpha,\beta=0}^{N-1} X_\alpha X_\beta^* \delta_{n-p,\beta-\alpha}$. Here, X_α are fixed such that $H_0 = H_{\text{HS},xy}$.

To illustrate the effect of error cancellations, we consider first a scenario where we directly apply Eq. 22. To leading order, the effective Hamiltonian is $H_{\text{eff}},1$ as in Eq. 19. We then analyze the two-step driving, using the effective Hamiltonian $H_{\text{eff}},2$ in Eq. 20, with H_p given by Eqs. S45 and S46.

We calculate the ground-state energies and eigenvectors of H_0 , $H_{\text{eff}},1$, and $H_{\text{eff}},2$, which we denote as $E_{0,1,2}$ and $|\Psi_{0,1,2}\rangle$, respectively, for different number of atoms and different ratios of δ/J_0 . The results are shown in Figs. 9 and 10. In panels A, we show the error in absolute value with respect to the ideal Hamiltonian H_0 . Interestingly, due to particular structure of $|\Psi_0\rangle$ and H_p , one can show that $\langle \Psi_0 | [H_p, H_{-p}] | \Psi_0 \rangle \approx 0$ and the first-order correction to the energy vanishes. This is confirmed in Fig. 10A, where we found that the error actually scales with $1/\delta^2$.

Moreover, it is also enlightening to compare the overlap of the ground states as shown in Figs. 9B and 10B. We only compute

the even-atom number configuration as the odd ones are degenerate and therefore the ground state is not uniquely defined. We see that the ground-state overlap of $H_{\text{eff}},2$ is several orders of magnitude better than the one with $H_{\text{eff}},1$. Moreover, its dependence on δ is better than the $1/\delta^2$ expectation.

The Role of Time-Dependent Stark Shifts in the Error Analysis. In the previous discussions, we have dropped the contribution of the time-dependent Stark shifts:

$$H_{\text{ac}}(t) = - \sum_n \sum_{\alpha > \beta}^{m_p-1} \Re \left[\frac{\Omega_\alpha \Omega_\beta^*}{2\Delta} e^{i\tilde{\omega}_{\alpha\beta} t} \right] \sigma_{ss}^n, \quad [23]$$

where $\tilde{\omega}_{\alpha\beta} = \tilde{\omega}_\alpha - \tilde{\omega}_\beta$. In *SI Appendix F: Error Reduction and Analysis*, we discuss its role in the effective Hamiltonian, using the Floquet error analysis. To summarize, we evaluated the error in the two-step driving scheme in various configurations.

Generic Hamiltonians with translational invariance. By translational invariance, we mean that there are no site-dependent spin interactions, and the spin-exchange coefficients remain identical as we offset the spin index by one or more. This means that all components in the pump field should drive the system with uniform optical phases as in the Haldane–Shastry model discussed above. The error by $H_{\text{ac}}(t)$ averages out to zero in the Floquet picture. In the butterfly scheme, however, both $|g\rangle$ and $|s\rangle$ states are pumped and they may be shifted differently. This leads to slight modifications in the engineered XX and YY terms.

Models containing sublattices. For topological models that contain sublattices, as in our examples, the pump fields are not perfectly transverse and Stark shifts are site dependent, resulting in non-vanishing error. For realistic PCW realizations, one should set moderate pump detuning $\tilde{J}/\Delta \gtrsim O(1)$ such that leading error contribution will be $\lesssim J^3/\delta^2$, and for $\delta \gg J$, the Stark shift terms may be ignored.

Stark shift-dominated regime. It may be possible that our sublattice models be purposely driven with large-amplitude pumps such that $|\Omega|^2/\Delta \gtrsim \delta$. Stark shift contributions would become important in the resulting spin dynamics. However, if we choose a large pump

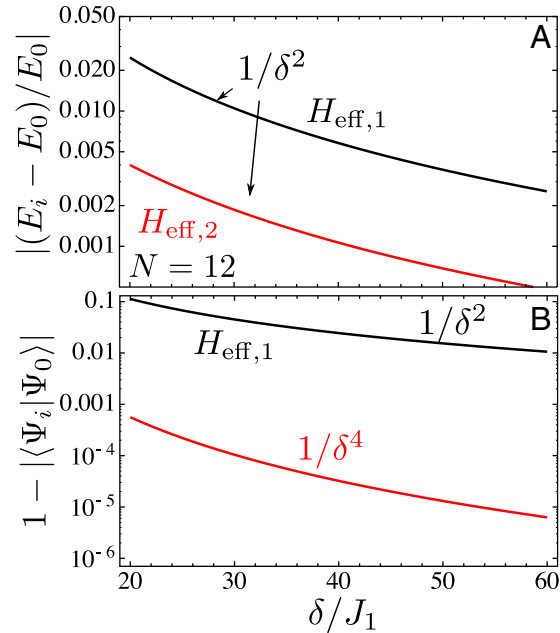


Fig. 10. (A) Comparison of ground-state energy error $|(E_i - E_0)/E_0|$ and (B) ground-state overlap $|\langle \Psi_i | \Psi_0 \rangle|$ as a function of δ/J_1 for Hamiltonians $H_{\text{eff}},1$ (black) and $H_{\text{eff}},2$ (red) for $N = 12$ atoms.

detuning $\Delta > \tilde{J}$, the dominant error contribution can in fact be written in the following simple form:

$$H_{\text{err},2} \approx \sum_{m,n} \tilde{A}_{m,n} (J_{m,n} \sigma_{\text{gs}}^m \sigma_{\text{sg}}^n + \text{h.c.}), \quad [24]$$

where $\tilde{A}_{m,n}$ is a site-dependent amplitude. In a special case that only two sublattices are present, as in our examples, we note that $\tilde{A}_{m,n}$ may only depend on the distance $r_{m,n}$ and is site independent. This “error” term would then uniformly modify the XY coupling strengths to a new value:

$$J'_{m,n} = (1 + \tilde{A}_{m,n}) J_{m,n}. \quad [25]$$

The next leading order errors are a factor of $\sim \tilde{J}/\Delta$ smaller than this leading Stark shift contribution, suggesting we can always increase the detuning Δ , while keeping $|\Omega|/\Delta$ constant, to reduce the error contribution.

Other Error Sources and Heating Effects. Apart from errors arising from multifrequency driving, there are other common error sources in cold atoms that we have not considered so far, such as motional heating. In the PCW platform, atoms are tightly confined with a trap depth more than three orders of magnitude larger than the recoil energy, rendering well-separated motional bands such that effects like interband heating (101) can be suppressed. Spin-exchange rates in the PCW platform, however, can be adjusted to 1 MHz $\gtrsim |J^{xy,z}| \gg 1$ kHz so that the many-body time scales ($\ll 1$ ms) can be much faster than those associated with motional heating.

In fact, spin temperature can be decoupled from real atomic temperature while simulating the spin models. For example, one can polarize atomic spins initially in a strong magnetic field ($B \gg |J^{xy,z}|$) to approximate a zero-temperature paramagnetic phase (17). The magnetic field can then be ramped down adiabatically to the final value of the desired spin model. Limitations to adiabaticity and, therefore, to the accessible spin temperature will ultimately be limited by the fidelity of the spin-exchange (36, 37) or by motional heating that leads to dephasing, whichever gives a more stringent bound.

Conclusions and Outlook

In this paper, we have shown that atom-nanophotonic systems present appealing platforms to engineer many-body quantum matter by using low-dimensional photons to mediate interaction between distant atom pairs. We have shown that, by introducing energy gradients in 1D and 2D, and by applying multifrequency

Raman addressing beams, it is possible to engineer a large class of many-body Hamiltonians. In particular, by carefully arranging the propagation phases of Raman beams, it is possible to introduce geometric phases into the spin system, thereby realizing nontrivial topological models with long-range spin–spin interactions.

Another appealing feature of our platform is the possibility of engineering periodic boundary conditions, as explicitly shown in the 1D Haldane–Shastry model, or other global lattice topology by introducing long-range interactions between spins located at the boundaries of a finite system. Using 2D PCWs, for example, it is possible to create previously unavailable spin-lattice geometries such as Möbius strip, torus, or lattice models with singular curvatures such as conic geometries (102) that may lead to localized topological states with potential applications in quantum computations.

We emphasize that all of the pairwise-tunable interactions can be dynamically tuned via, for example, electro-optical modulators at timescales much faster than that of characteristic spin interactions. Therefore, the spin interactions can either be adiabatically adjusted to transform between spin models or even be suddenly quenched down to zero by removing all or part of the Raman coupling beams. We may monitor spin dynamics with great detail: after we initially prepare the atomic spins in a known state by, say, individual or collective microwave addressing, we can set the system to evolve under a designated spin Hamiltonian, followed by removing all of the interactions to “freeze” the dynamics for atomic state detection. Potentially, this allows for detailed studies on quantum dynamics of long-range, strongly interacting spin systems that are driven out-of-equilibrium. The dynamics may be even richer because the spins are weakly coupled to a structured environment via photon dissipations. We expect such a platform may bring novel opportunities to the study of quantum thermalization in long-range many-body systems, or for further understanding of information propagation in a long-range quantum network.

ACKNOWLEDGMENTS. We gratefully acknowledge discussions with T. Shi and Y. Wu. The work of C.-L.H. and H.J.K. was funded by the Institute for Quantum Information and Matter, a National Science Foundation (NSF) Physics Frontier Center with support of the Moore Foundation; by the Air Force Office of Scientific Research (AFOSR) Quantum Memories in Photon-Atomic Solid-State Systems Multidisciplinary Research Program of the University Research Initiative (MURI); by the Department of Defense National Security Science and Engineering Faculty Fellowship Program; by NSF Grant PHY1205729; by the Office of Naval Research (ONR) Award N00014-16-1-2399; and by the ONR Quantum Opto-Mechanics with Atoms and Nanostructured Diamond MURI. A.G.-T. and J.I.C. acknowledge funding by the European Union integrated project “Simulators and Interfaces with Quantum Systems.” A.G.-T. also acknowledges support from Alexander Von Humboldt Foundation and Intra-European Marie Curie Fellowship Nanophotonics for Quantum Information and Simulation (625955).

1. Cirac JI, Zoller P (2012) Goals and opportunities in quantum simulation. *Nat Phys* 8(4): 264–266.
2. Jaksch D, Zoller P (2005) The cold atom Hubbard toolbox. *Ann Phys* 315(1):52–79.
3. Bloch I, Dalibard J, Nascimbène S (2012) Quantum simulations with ultracold quantum gases. *Nat Phys* 8:267–276.
4. Trotzky S, et al. (2008) Time-resolved observation and control of superexchange interactions with ultracold atoms in optical lattices. *Science* 319(5861):295–299.
5. Simon J, et al. (2011) Quantum simulation of antiferromagnetic spin chains in an optical lattice. *Nature* 472(7343):307–312.
6. Greif D, Uehlinger T, Jotzu G, Tarruell L, Esslinger T (2013) Short-range quantum magnetism of ultracold fermions in an optical lattice. *Science* 340(6138): 1307–1310.
7. Griesmaier A, Werner J, Hensler S, Stuhler J, Pfau T (2005) Bose-Einstein condensation of chromium. *Phys Rev Lett* 94(16):160401.
8. Lu M, Burdick NQ, Youn SH, Lee BL (2011) Strongly dipolar Bose-Einstein condensate of dysprosium. *Phys Rev Lett* 107(19):190401.
9. Micheli A, Brennen G, Zoller P (2006) A toolbox for lattice-spin models with polar molecules. *Nat Phys* 2(5):341–347.
10. Ni KK, et al. (2008) A high phase-space-density gas of polar molecules. *Science* 322(5899):231–235.
11. Yan B, et al. (2013) Observation of dipolar spin-exchange interactions with lattice-confined polar molecules. *Nature* 501(7468):521–525.
12. Jaksch D, et al. (2000) Fast quantum gates for neutral atoms. *Phys Rev Lett* 85(10): 2208–2211.
13. Weimer H, Muller M, Lesanovsky I, Zoller P, Buchler HP (2010) A Rydberg quantum simulator. *Nat Phys* 6(5):382–388.
14. Saffman M, Walker TG, Mølmer K (2010) Quantum information with Rydberg atoms. *Rev Mod Phys* 82(3):2313–2363.
15. Schauß P, et al. (2012) Observation of spatially ordered structures in a two-dimensional Rydberg gas. *Nature* 491(7422):87–91.
16. Porras D, Cirac JI (2004) Effective quantum spin systems with trapped ions. *Phys Rev Lett* 92(20):207901.
17. Kim K, et al. (2010) Quantum simulation of frustrated Ising spins with trapped ions. *Nature* 465(7298):590–593.
18. Blatt R, Roos CF (2012) Quantum simulations with trapped ions. *Nat Phys* 8(4): 277–284.
19. Britton JW, et al. (2012) Engineered two-dimensional Ising interactions in a trapped-ion quantum simulator with hundreds of spins. *Nature* 484(7395):489–492.
20. Islam R, et al. (2013) Emergence and frustration of magnetism with variable-range interactions in a quantum simulator. *Science* 340(6132):583–587.
21. Korenblit S, et al. (2012) Quantum simulation of spin models on an arbitrary lattice with trapped ions. *New J Phys* 14(9):095024.
22. Kimble HJ (2008) The quantum internet. *Nature* 453(7198):1023–1030.
23. Baumann K, Guerlin C, Brennecke F, Esslinger T (2010) Dicke quantum phase transition with a superfluid gas in an optical cavity. *Nature* 464(7293):1301–1306.
24. Gopalakrishnan S, Lev BL, Goldbart PM (2009) Emergent crystallinity and frustration with Bose-Einstein condensates in multimode cavities. *Nat Phys* 5(11):845–850.
25. Goban A, et al. (2014) Atom-light interactions in photonic crystals. *Nat Commun* 5:3808.

26. Goban A, et al. (2015) Superradiance for atoms trapped along a photonic crystal waveguide. *Phys Rev Lett* 115(6):063601.

27. Thompson JD, et al. (2013) Coupling a single trapped atom to a nanoscale optical cavity. *Science* 340(6137):1202–1205.

28. Tiecke TG, et al. (2014) Nanophotonic quantum phase switch with a single atom. *Nature* 508(7495):241–244.

29. Majumdar A, et al. (2012) Design and analysis of photonic crystal coupled cavity arrays for quantum simulation. *Phys Rev B* 86(19):195312.

30. Javadi A, et al. (2015) Single-photon non-linear optics with a quantum dot in a waveguide. *Nat Commun* 6:8655.

31. Barclay PE, Fu KM, Santori C, Beausoleil RG (2009) Hybrid photonic crystal cavity and waveguide for coupling to diamond NV-centers. *Opt Express* 17(12):9588–9601.

32. Hausmann BJM, et al. (2013) Coupling of NV centers to photonic crystal nanobeams in diamond. *Nano Lett* 13(12):5791–5796.

33. Houch AE, Türeci HE, Koch J (2012) On-chip quantum simulation with superconducting circuits. *Nat Phys* 8(4):292–299.

34. Eichler C, et al. (2015) Exploring interacting quantum many-body systems by experimentally creating continuous matrix product states in superconducting circuits. *Phys Rev X* 5(4):041044.

35. McKay DC, Naik R, Reinhold P, Bishop LS, Schuster DI (2015) High-contrast qubit interactions using multimode cavity QED. *Phys Rev Lett* 114(8):080501.

36. Douglas JS, et al. (2015) Quantum many-body models with cold atoms coupled to photonic crystals. *Nat Photonics* 9(5):326–331.

37. González-Tudela A, Hung CL, Chang D, Cirac J, Kimble H (2015) Subwavelength vacuum lattices and atom-atom interactions in photonic crystals. *Nat Photonics* 9(5):320–325.

38. Kurizki G (1990) Two-atom resonant radiative coupling in photonic band structures. *Phys Rev A* 42(5):2915–2924.

39. John S, Wang J (1990) Quantum electrodynamics near a photonic band gap: Photon bound states and dressed atoms. *Phys Rev Lett* 64(20):2418–2421.

40. John S, Wang J (1991) Quantum optics of localized light in a photonic band gap. *Phys Rev B Condens Matter* 43(16):12772–12789.

41. Hartmann MJ, Brandao FGSL, Plenio MB (2006) Strongly interacting polaritons in coupled arrays of cavities. *Nat Phys* 2(12):849–855.

42. Greentree AD, Tahan C, Cole JH, Hollenberg LCL (2006) Quantum phase transitions of light. *Nat Phys* 2(12):856.

43. Cho J, Angelakis DG, Bose S (2008) Fractional quantum Hall state in coupled cavities. *Phys Rev Lett* 101(24):246809.

44. Hartmann MJ, Brandão FGSL, Plenio MB (2008) Quantum many-body phenomena in coupled cavity arrays. *Laser Photonics Rev* 2(6):527.

45. Eisert J, van den Worm M, Manmansa SR, Kastner M (2013) Breakdown of quasilocality in long-range quantum lattice models. *Phys Rev Lett* 111(26):260401.

46. Gong ZX, Foss-Feig M, Michalakis S, Gorshkov AV (2014) Persistence of locality in systems with power-law interactions. *Phys Rev Lett* 113(3):030602.

47. Jurcevic P, et al. (2014) Quasiparticle engineering and entanglement propagation in a quantum many-body system. *Nature* 511(7508):202–205.

48. Richerme P, et al. (2014) Non-local propagation of correlations in quantum systems with long-range interactions. *Nature* 511(7508):198–201.

49. Hazzard KRA, et al. (2014) Quantum correlations and entanglement in far-from-equilibrium spin systems. *Phys Rev A* 90(6):063622.

50. Vodola D, Lepori L, Ercolessi E, Gorshkov AV, Pupillo G (2014) Kitaev chains with long-range pairing. *Phys Rev Lett* 113(15):156402.

51. Jaksch D, Zoller P (2003) Creation of effective magnetic fields in optical lattices: The Hofstadter butterfly for cold neutral atoms. *New J Phys* 5(1):56.

52. Bermudez A, Schaeftz T, Porras D (2011) Synthetic gauge fields for vibrational excitations of trapped ions. *Phys Rev Lett* 107(15):150501.

53. Kolovsky AR (2011) Creating artificial magnetic fields for cold atoms by photon-assisted tunneling. *EPL* 93(2):20003.

54. Aidelsburger M, et al. (2013) Realization of the Hofstadter Hamiltonian with ultracold atoms in optical lattices. *Phys Rev Lett* 111(18):185301.

55. Miyake H, Siviloglou GA, Kennedy CJ, Burton WC, Ketterle W (2013) Realizing the Harper Hamiltonian with laser-assisted tunneling in optical lattices. *Phys Rev Lett* 111(18):185302.

56. Haldane FDM (1988) Exact Jastrow-Gutzwiller resonating-valence-bond ground state of the spin-1/2 antiferromagnetic Heisenberg chain with $1/l^2$ exchange. *Phys Rev Lett* 60(7):635–638.

57. Shastry BS (1988) Exact solution of an $S = 1/2$ Heisenberg antiferromagnetic chain with long-ranged interactions. *Phys Rev Lett* 60(7):639–642.

58. Neupert T, Santos L, Chamon C, Mudry C (2011) Fractional quantum Hall states at zero magnetic field. *Phys Rev Lett* 106(23):236804.

59. Sun K, Gu Z, Katsura H, Das Sarma S (2011) Nearly flatbands with nontrivial topology. *Phys Rev Lett* 106(23):236803.

60. Maik M, Hauke P, Dutta O, Zakrzewski J, Lewenstein M (2012) Quantum spin models with long-range interactions and tunnelings: A quantum Monte Carlo study. *New J Phys* 14(11):113006.

61. Blaum A, Huang RS, Wallraff A, Girvin SM, Schoelkopf RJ (2004) Cavity quantum electrodynamics for superconducting electrical circuits: An architecture for quantum computation. *Phys Rev A* 69(6):062320.

62. Schuster DI, et al. (2007) Resolving photon number states in a superconducting circuit. *Nature* 445(7127):515–518.

63. Jané E, Vidal G, Dür W, Zoller P, Cirac JI (2003) Simulation of quantum dynamics with quantum optical systems. *Quantum Inf Comput* 3(1):15–37.

64. Berry DW, Ahokas G, Cleve R, Sanders BC (2007) Efficient quantum algorithms for simulating sparse Hamiltonians. *Commun Math Phys* 270(2):359–371.

65. Childs AM, Kothari R (2011) Simulating sparse Hamiltonians with star decompositions. *Theory of Quantum Computation, Communication, and Cryptography* (Springer, Berlin), pp 94–103.

66. Berry DW, Childs AM (2012) Black-box Hamiltonian simulation and unitary implementation. *Quantum Information and Computation* 12(1–2):29.

67. Dalibard J, Gerbier F, Juzeliūnas G, Öhberg P (2011) Colloquium: Artificial gauge potentials for neutral atoms. *Rev Mod Phys* 83(4):1523–1543.

68. Hauke P, et al. (2012) Non-abelian gauge fields and topological insulators in shaken optical lattices. *Phys Rev Lett* 109(14):145301.

69. Struck J, et al. (2013) Engineering Ising-xy spin-models in a triangular lattice using tunable artificial gauge fields. *Nat Phys* 9(11):738–743.

70. Goldman N, Juzeliūnas G, Öhberg P, Spielman IB (2014) Light-induced gauge fields for ultracold atoms. *Rep Prog Phys* 77(12):126401.

71. Atala M, et al. (2014) Observation of chiral currents with ultracold atoms in bosonic ladders. *Nat Phys* 10(8):588–593.

72. Kennedy CJ, Burton WC, Chung WC, Ketterle W (2015) Observation of Bose-Einstein condensation in a strong synthetic magnetic field. *Nat Phys* 11(10):859–864.

73. Haldane FDM (1988) Model for a quantum Hall effect without Landau levels: Condensed-matter realization of the “parity anomaly.” *Phys Rev Lett* 61(18):2015–2018.

74. Jotzu G, et al. (2014) Experimental realization of the topological Haldane model with ultracold fermions. *Nature* 515(7526):237–240.

75. Duca L, et al. (2015) An Aharonov-Bohm interferometer for determining Bloch band topology. *Science* 347(6219):288–292.

76. Aidelsburger M, et al. (2015) Measuring the chern number of Hofstadter bands with ultracold bosonic atoms. *Nat Phys* 11(2):162–166.

77. Fläschner N, et al. (2016) Experimental reconstruction of the Berry curvature in a topological Bloch band. *Science* 352(6389):1901–1904.

78. Lohse M, Schweizer C, Zilberman O, Aidelsburger M, Bloch I (2016) A thouless quantum pump with ultracold bosonic atoms in an optical superlattice. *Nat Phys* 12(4):350–354.

79. Nakajima S, et al. (2016) Topological thouless pumping of ultracold fermions. *Nat Phys* 12(4):296–300.

80. Wu Z, et al. (2015) Realization of two-dimensional spin-orbit coupling for Bose-Einstein condensates. *arXiv:1511.08170*.

81. Mancini M, et al. (2015) Observation of chiral edge states with neutral fermions in synthetic Hall ribbons. *Science* 349(6255):1510–1513.

82. Stuhl BK, Lu HI, Aycoc LM, Genkina D, Spielman IB (2015) Visualizing edge states with an atomic Bose gas in the quantum Hall regime. *Science* 349(6255):1514–1518.

83. Cooper NR, Dalibard J (2013) Reaching fractional quantum Hall states with optical flux lattices. *Phys Rev Lett* 110(18):185301.

84. Yao NY, et al. (2013) Realizing fractional Chern insulators in dipolar spin systems. *Phys Rev Lett* 110(18):185302.

85. Wang YF, Gu ZC, Gong CD, Sheng DN (2011) Fractional quantum Hall effect of hard-core bosons in topological flat bands. *Phys Rev Lett* 107(14):146803.

86. Tarruell L, Greif D, Uehlinger T, Jotzu G, Esslinger T (2012) Creating, moving and merging Dirac points with a Fermi gas in a tunable honeycomb lattice. *Nature* 483(7389):302–305.

87. Kitaev A (2006) Anyons in an exactly solved model and beyond. *Ann Phys* 321(1):2–111.

88. Feng XY, Zhang GM, Xiang T (2007) Topological characterization of quantum phase transitions in a spin-1/2 model. *Phys Rev Lett* 98(8):087204.

89. Graß T, Muschik C, Celi A, Chhajlany RW, Lewenstein M (2015) Synthetic magnetic fluxes and topological order in one-dimensional spin systems. *Phys Rev A* 91(6):063612.

90. Wessel S, Troyer M (2005) Supersolid hard-core bosons on the triangular lattice. *Phys Rev Lett* 95(12):127205.

91. Melko RG, et al. (2005) Supersolid order from disorder: Hard-core bosons on the triangular lattice. *Phys Rev Lett* 95(12):127207.

92. Boninsegni M, Prokof'ev N (2005) Supersolid phase of hard-core bosons on a triangular lattice. *Phys Rev Lett* 95(23):237204.

93. Trefzger C, Menotti C, Lewenstein M (2008) Ultracold dipolar gas in an optical lattice: The fate of metastable states. *Phys Rev A* 78(4):043604.

94. Büchler HP, et al. (2007) Strongly correlated 2D quantum phases with cold polar molecules: Controlling the shape of the interaction potential. *Phys Rev Lett* 98(6):060404.

95. Hauke P, et al. (2010) Complete devil's staircase and crystal-superfluid transitions in a dipolar XXZ spin chain: A trapped ion quantum simulation. *New J Phys* 12(11):113037.

96. Hauke P, Tagliacozzo L (2013) Spread of correlations in long-range interacting quantum systems. *Phys Rev Lett* 111(20):207202.

97. Bal P, Bruinsma R (1982) One-dimensional Ising model and the complete devil's staircase. *Phys Rev Lett* 49(4):249–251.

98. Hood JD, et al. (2016) Atom-atom interactions around the band edge of a photonic crystal waveguide. *arXiv:1603.02771*.

99. Goldman N, Dalibard J (2014) Periodically driven quantum systems: Effective Hamiltonians and engineered gauge fields. *Phys Rev X* 4(3):031027.

100. Goldman N, Dalibard J, Aidelsburger M, Cooper NR (2015) Periodically driven quantum matter: The case of resonant modulations. *Phys Rev A* 91(3):033632.

101. Weinberg M, et al. (2015) Multiphoton interband excitations of quantum gases in driven optical lattices. *Phys Rev A* 92(4):043621.

102. Biswas RR, Son DT (2014) Fractional charge and inter-Landau level states at points of singular curvature. *arXiv:1412.3809*.

103. Gardiner GW, Zoller P (2000) *Quantum Noise* (Springer, Berlin), 2nd Ed.

104. Lloyd S (1996) Universal quantum simulators. *Science* 273(5278):1073–1078.

Supporting Information

Hung et al. 10.1073/pnas.1603777113

SI Summary

In *SI Appendix A: Complete Derivation of Final Time-Dependent Hamiltonian*, we give a detailed derivation of the time- dependent effective Hamiltonian (Eq. 4 of the main text):

$$H_{XY}(t) = \sum_{m,n \neq m}^N \sum_{\alpha,\beta=0}^{m_p-1} X_\alpha X_\beta^* \tilde{J}(\mathbf{r}_{m,n}) e^{i(\omega_{gm} - \omega_{gn} + \tilde{\omega}_\alpha - \tilde{\omega}_\beta)t} \sigma_{gs}^m \sigma_{sg}^n. \quad [\text{S1}]$$

In *SI Appendix B: Proper Choice of Ground-State Energy Shifts in 2D Models*, we discuss how to properly introduce ground-state energy shifts to engineer generic spin models in 2D. In *SI Appendix C: Pump Field Configurations for Engineering a Chiral-Flux Square Lattice Model*, *SI Appendix D: Pump Field Configurations for Engineering a Topological Spin Model in a Brick Wall Lattice*, and *SI Appendix E: PCW and Pump Field Configurations for Engineering an XXZ Spin Hamiltonian with $1/r^n$ Interaction*, we describe in detail the PCW and the pump field configurations to engineer a topological chiral-flux lattice model, a brick wall lattice model, and an XXZ model with $1/r^n$ dependence, respectively. In *SI Appendix F: Error Reduction and Analysis*, we discuss in detail regarding error reduction and analysis.

SI Appendix A: Complete Derivation of Final Time-Dependent Hamiltonian

The PCWs support localized one or 2D photonic guided modes (GMs), which can be described by a Hamiltonian (using $\hbar = 1$):

$$H_{\text{GM}} = \sum_{\mathbf{k}} \omega_{\mathbf{k}} a_{\mathbf{k}}^\dagger a_{\mathbf{k}}, \quad [\text{S2}]$$

where $\omega_{\mathbf{k}}$ is the dispersion relation of the GMs. Neglecting counter rotating terms, the light-matter Hamiltonian can be written as follows:

$$H_{\text{lm}} = \sum_{\mathbf{k},n} g_{\mathbf{k}}(\mathbf{r}_n) a_{\mathbf{k}} \sigma_{eg}^n + \text{h.c.}, \quad [\text{S3}]$$

where $g_{\mathbf{k}}(\mathbf{r}_n) = g_{\mathbf{k}} e^{i\mathbf{k} \cdot \mathbf{r}_n}$ is the single-photon coupling constant. The atomic Hamiltonian is given by the following:

$$H_{\text{a}} = \sum_n \left(\omega_e \sigma_{ee}^n + \omega_{g,n} \sigma_{gg}^n \right), \quad [\text{S4}]$$

where it is important to highlight that we introduce a site-dependent energy in the hyperfine level $|g\rangle_n$ that can be achieved, for example, by introducing a magnetic field gradient (or a Stark shift gradient) in either 1D or 2D as depicted in Fig. 1 *A* and *B* in the main text. This site-dependent energy, together with a multifrequency driving for $|s\rangle_n \leftrightarrow |e\rangle_n$ are the key ingredients of our proposal. Multifrequency driving with m_p different components can be described through a Hamiltonian:

$$H_{\text{d}}(t) = \sum_n \left(\frac{\Omega(t)}{2} \sigma_{se}^n e^{i\omega_L t} + \text{h.c.} \right), \quad [\text{S5}]$$

where we have used the notation $\sigma_{ab}^n = |a\rangle_n \langle b|$, and ω_L is the main driving frequency. All components of the driving field are embedded in $\Omega(t)$, which can be written as follows:

$$\Omega(t) \equiv \sum_{\alpha=0}^{m_p-1} \Omega_\alpha e^{i\tilde{\omega}_\alpha t}, \quad [\text{S6}]$$

where $\tilde{\omega}_\alpha$ are m_p different frequency detunings ($\tilde{\omega}_{\alpha=0} = 0$) and Ω_α the Rabi frequency that will be used to achieve full control of the

atom–atom interactions. The dynamics of the system is described by the sum of all of the above Hamiltonians: $H = H_{\text{a}} + H_{\text{GM}} + H_{\text{d}}(t) + H_{\text{lm}}$.

We are interested in the conditions where $|\Delta| = |\omega_e - \omega_L| \gg \Omega$, such that the excited states are only virtually populated. To adiabatically eliminate states $|e\rangle_n$, it is convenient to work in a rotating frame defined by the transformation $U = \exp(i(\sum_n \omega_L \sigma_{ee}^n t + i\sum_{\mathbf{k}} \omega_{\mathbf{k}} a_{\mathbf{k}}^\dagger a_{\mathbf{k}})t)$, which transforms the Hamiltonian by $H \rightarrow U H U^\dagger - iU \partial_t U^\dagger$. Writing each of the transformed Hamiltonians, we have the following:

$$\begin{aligned} H_{\text{lm}} \rightarrow \tilde{H}_{\text{lm}} &= \sum_{\mathbf{k},n} g_{\mathbf{k}}(\mathbf{r}_n) a_{\mathbf{k}} \sigma_{eg}^n e^{i(\omega_L - \omega_{\mathbf{k}})t} + \text{h.c.}, \\ H_{\text{d}} \rightarrow \tilde{H}_{\text{d}} &= \sum_n \left(\frac{\Omega(t)}{2} \sigma_{se}^n + \text{h.c.} \right), \\ H_{\text{a}} \rightarrow \tilde{H}_{\text{a}} &= \sum_n \left(\Delta \sigma_{ee}^n + \omega_{g,n} \sigma_{gg}^n \right), \end{aligned} \quad [\text{S7}]$$

while H_{GM} transforms to zero. Notice that, due to the multifrequency driving, it is not possible to find a reference frame where the Hamiltonian is time independent. Despite the time dependence, it is still possible to adiabatically eliminate the excited states. For this purpose, we define a projector operator for the atomic subspace, $\mathbb{P} = \sum_n (\sigma_{gg}^n + \sigma_{ss}^n)$, that projects out the excited states, and its orthogonal counterpart, $\mathbb{Q} = \sum_n \sigma_{ee}^n$. Using these operators, one can formally project out slow and fast subspaces in the Schrödinger equation:

$$\begin{aligned} i \frac{d\mathbb{P}|\Psi\rangle}{dt} &= \mathbb{P} H \mathbb{P} |\Psi\rangle + \mathbb{P} H \mathbb{Q} |\Psi\rangle, \\ i \frac{d\mathbb{Q}|\Psi\rangle}{dt} &= \mathbb{Q} H \mathbb{P} |\Psi\rangle + \mathbb{Q} H \mathbb{Q} |\Psi\rangle. \end{aligned} \quad [\text{S8}]$$

By using the fact that $\mathbb{Q} H \mathbb{Q}$ is actually time independent and assuming that initially there are no contributions from the excited states, that is, $\mathbb{Q}|\Psi(0)\rangle = 0$, one can formally integrate $\mathbb{Q}|\Psi\rangle$ (by parts), input the result into the equation of $\mathbb{P}|\Psi\rangle$, and obtain an effective Hamiltonian for the slow subspace:

$$i \frac{d\mathbb{P}|\Psi\rangle}{dt} \approx \left(\mathbb{P} H \mathbb{P} - \mathbb{P} H \mathbb{Q} \frac{1}{\mathbb{Q} H \mathbb{Q}} \mathbb{Q} H \mathbb{P} \right) \mathbb{P} |\Psi\rangle \equiv H_{\text{eff}} \mathbb{P} |\Psi\rangle. \quad [\text{S9}]$$

The resulting effective Hamiltonian then reads as the following:

$$\begin{aligned} H_{\text{eff}} &= \tilde{H}_{\text{eff,a}} + \tilde{H}_{\text{eff,lm}} + \tilde{H} \\ &= \sum_n \left(\omega_{g,n} \sigma_{gg,n} - \frac{\Omega(t) \Omega^*(t)}{4\Delta} \sigma_{ss,n} \right) \\ &\quad - \sum_{\mathbf{k},n} \frac{g_{\mathbf{k}}(\mathbf{r}_n) \Omega(t)}{2\Delta} a_{\mathbf{k}} \sigma_{sg}^n e^{i(\omega_L - \omega_{\mathbf{k}})t} + \text{h.c.}, \\ &\quad - \sum_{\mathbf{k},n} \frac{|g_{\mathbf{k}}(\mathbf{r}_n)|^2}{\Delta} a_{\mathbf{k}}^\dagger a_{\mathbf{k}} \sigma_{gg}^n, \end{aligned} \quad [\text{S10}]$$

where we have absorbed some irrelevant phases. The contribution of $\tilde{H} = -\sum_{\mathbf{k},n} (|g_{\mathbf{k}}(\mathbf{r}_n)|^2 / \Delta) a_{\mathbf{k}}^\dagger a_{\mathbf{k}} \sigma_{gg}^n$ will be negligible because it is proportional to the number of GM photons, which is close to 0 in our situation (36, 37). Rewriting the effective Hamiltonian in the

interaction picture with respect to $\tilde{H}_{\text{eff,a}}$, we arrive at the following light-matter Hamiltonian:

$$H_{\text{eff,lm}}(t) = -\sum_{\mathbf{k},n} \frac{g_{\mathbf{k}}(\mathbf{r}_n)\Omega(t)}{2\Delta} a_{\mathbf{k}} \sigma_{sg}^n e^{i(\omega_L - \omega_{\mathbf{k}} - \omega_{g,n})t} + \text{h.c.} \quad [\text{S11}]$$

Note that, for simplicity in the derivation, we have neglected the contribution of the time-dependent Stark shift in the $|s\rangle_n$ states, which is given by the following:

$$\delta\omega_s(t) = -\frac{\Omega(t)\Omega^*(t)}{4\Delta} = -\sum_{\alpha=0}^{m_p-1} \frac{|\Omega_{\alpha}|^2}{4\Delta} - \sum_{\alpha>\beta}^{m_p-1} \Re \left[\frac{\Omega_{\alpha}\Omega_{\beta}^*}{2\Delta} e^{i(\tilde{\omega}_{\alpha} - \tilde{\omega}_{\beta})t} \right]. \quad [\text{S12}]$$

Here, $\Re[\cdot]$ indicates real part. The time-independent contribution can be absorbed into the energy of ω_s without significant contribution to the dynamics, whereas the time-dependent terms will be averaged out in the atomic timescales that we are interested in. We consider its possible detrimental effects in *SI Appendix F: Error Reduction and Analysis*, where we analyze the limitations and other error sources.

The relaxation timescales of the GMs in the PCWs are typically much faster than the atomic ones, such that we can trace out the photonic information to obtain an effective master equation that describes the dynamics of the atomic system through its density matrix evolution (103):

$$\frac{d\rho}{dt} = \sum_{m,n} \left[\Gamma_{m,n}(t) \left(\sigma_{sg}^n \rho \sigma_{gs}^m - \sigma_{sg}^n \sigma_{gs}^m \rho \right) + \Gamma_{m,n}^*(t) \left(\sigma_{sg}^m \rho \sigma_{gs}^n - \rho \sigma_{sg}^m \sigma_{gs}^n \right) \right], \quad [\text{S13}]$$

where the time-dependent coefficients are given by the following:

$$\Gamma_{m,n}(t) = \int_0^{\infty} ds f_{\mathbf{k},m,n} e^{i(\omega_{g,m} - \omega_{g,n})t} e^{-i(\omega_k + \omega_{g,m} - \omega_L)s} \frac{\Omega(t)\Omega^*(t-s)}{4\Delta^2}, \quad [\text{S14}]$$

with $f_{\mathbf{k},m,n} = \sum_{\mathbf{k}} |g_{\mathbf{k}}|^2 e^{i\mathbf{k}\cdot(\mathbf{r}_n - \mathbf{r}_m)}$. Expanding $\Omega(t)\Omega^*(t-s) = \sum_{\alpha,\beta} \Omega_{\alpha}\Omega_{\beta}^* e^{i(\tilde{\omega}_{\alpha} - \tilde{\omega}_{\beta})t} e^{i\tilde{\omega}_{\beta}s}$, we find that

$$\Gamma_{m,n}(t) = \sum_{\alpha,\beta} \frac{\Omega_{\alpha}\Omega_{\beta}^*}{4\Delta^2} \Gamma_{m,n,\beta,\infty} e^{i(\omega_{g,m} - \omega_{g,n} + \tilde{\omega}_{\alpha} - \tilde{\omega}_{\beta})t}, \quad [\text{S15}]$$

where $\Gamma_{m,n,\beta,\infty}$ is the time-independent contribution that can be written as follows:

$$\Gamma_{m,n,\beta,\infty} = \int_0^{\infty} ds f_{\mathbf{k},m,n} e^{-i(\omega_k + \omega_{g,m} - \omega_L - \tilde{\omega}_{\beta})s}. \quad [\text{S16}]$$

Using that $\int_0^{\infty} e^{ix\tau} d\tau = \pi\delta(x) - iP(1/x)$, and assuming that we are working in the regime within the band gap (Fig. 1D; assuming an infinite structure), that is, $\Delta_{m,\beta} = \omega_c - \omega_L + \omega_{g,m} - \tilde{\omega}_{\beta} < 0$ such that the dissipative terms [δ-contribution] vanish, $\Gamma_{m,n}(t)$ contains only dispersive contributions,

$$\Gamma_{m,n}(t) = i \sum_{\alpha,\beta} \frac{\Omega_{\alpha}\Omega_{\beta}^*}{4\Delta^2} \tilde{J}_{m,n} e^{i(\omega_{g,m} - \omega_{g,n} + \tilde{\omega}_{\alpha} - \tilde{\omega}_{\beta})t}, \quad [\text{S17}]$$

and $\tilde{J}_{m,n}$ is defined as follows:

$$\tilde{J}_{m,n} = \sum_{\mathbf{k} \in \text{BZ}} \frac{|g_{\mathbf{k}}|^2}{(\omega_L - \omega_k - \omega_{g,m} + \tilde{\omega}_{\beta})} e^{i\mathbf{k}\cdot(\mathbf{r}_n - \mathbf{r}_m)}, \quad [\text{S18}]$$

coinciding with the expressions obtained in refs. 36 and 37 when $|\tilde{\omega}_{\beta} - \omega_{g,m}| \ll |\omega_L - \omega_c|$. Then, depending on the dimensionality of the reservoir, we have the following (36, 37):

$$\tilde{J}_{m,n,1\text{d}} \propto e^{-|\mathbf{r}_{m,n}|/\xi}, \quad [\text{S19}]$$

$$\tilde{J}_{m,n,2\text{d}} \propto K_0(|\mathbf{r}_{m,n}|/\xi), \quad [\text{S20}]$$

where $\mathbf{r}_{m,n} = \mathbf{r}_m - \mathbf{r}_n$ and $K_0(x)$ is the modified Bessel function of the second kind; $\xi = \sqrt{A/|\Delta_{xy}|}$ controls the effective range of the interaction; $\Delta_{xy} = |\omega_c - \omega_L|$ is the effective detuning with respect to the band edge, and A is the curvature of the band (Fig. 1C). Notice that there is another underlying assumption in the derivation, namely, that the coupling strength $|g_{\mathbf{k}}|^2$ of the driven GMs must be approximately constant for all of the sideband frequencies $\omega_L + \tilde{\omega}_{\alpha}$. If not, the variation of $|g_{\mathbf{k}}|^2$ can be compensated by adjusting sideband amplitudes Ω_{α} . Furthermore, because we focus on full control introduced by multifrequency drivings, we will not specify the form of $\tilde{J}_{m,n}$ and simply assume a constant $\tilde{J}_{m,n} = \tilde{J}$ throughout the interaction range considered. However, one should be aware that the length scale ξ will pose the ultimate limitation of the range of the interactions that we can simulate.

Because we have $\Gamma_{m,n}^*(t) = -\Gamma_{n,m}(t)$, the evolution of the density matrix in Eq. S13 is governed by an effective XY Hamiltonian:

$$H_{xy}(t) = \sum_{m,n \neq m}^N \sum_{\alpha,\beta} \frac{\Omega_{\alpha}\Omega_{\beta}^*}{4\Delta^2} \tilde{J}_{m,n} e^{i(\omega_{g,m} - \omega_{g,n} + \tilde{\omega}_{\alpha} - \tilde{\omega}_{\beta})t} \sigma_{gs}^m \sigma_{sg}^n. \quad [\text{S21}]$$

Interestingly, if we choose $\omega_{g,n} - \omega_{g,m} \neq 0$, we can control the resonant processes by adjusting the laser frequencies $\tilde{\omega}_{\alpha}$. In particular, two atoms n and m , will be interacting through a resonant process with rate $\Omega_{\alpha}\Omega_{\beta}^* \tilde{J}_{m,n}/(4\Delta^2)$ when the resonant condition,

$$\omega_{g,m} - \omega_{g,n} = \tilde{\omega}_{\beta} - \tilde{\omega}_{\alpha}, \quad [\text{S22}]$$

is satisfied. The intuitive picture is depicted in Fig. 2A in the main text: the atom n scatters from sideband α a photon with energy $\omega_L + \tilde{\omega}_{\alpha} - \omega_{g,n}$ into GMs. When this photon propagates to atom m , it will only be absorbed via a sideband β that satisfies $\omega_L + \tilde{\omega}_{\alpha} - \omega_{g,n} = \omega_L + \tilde{\omega}_{\beta} - \omega_{g,m}$, with the rest of the sidebands being off-resonant; Fig. 2B depicts the reversed process. Therefore, the Hamiltonian $H_{xy}(t)$ can be separated into time-independent (on-resonant) and time-independent (off-resonant) contributions: $H_{xy}(t) = H_{xy,0} + \tilde{H}_{xy}(t)$, where $H_{xy,0}$ is an XY spin Hamiltonian,

$$H_{xy,0} = \sum_{m,n \neq m}^N J_{m,n} \sigma_{gs}^m \sigma_{sg}^n, \quad [\text{S23}]$$

where the spin-exchange coefficient $J_{m,n}$ can be fully controlled by adjusting Ω_{α} and $\tilde{\omega}_{\alpha}$. We have the following:

$$J_{m,n} = \sum_{\alpha,\beta} \frac{\Omega_{\alpha}\Omega_{\beta}^*}{4\Delta^2} \tilde{J}_{m,n} \delta(\omega_{g,m} - \omega_{g,n} + \tilde{\omega}_{\alpha} - \tilde{\omega}_{\beta}), \quad [\text{S24}]$$

where $\delta(0) = 1$ and $\delta(x \neq 0) = 0$. Note that, to fully control $J_{m,n}$ at each distance $\mathbf{r}_{m,n}$, we need to introduce enough sidebands to cover all of the energy differences $\omega_{g,m} - \omega_{g,n}$.

If the characteristic energy scale of the spin Hamiltonian $H_{xy,0}$ is much smaller than the minimum energy detuning $\delta_{\omega} \equiv \min\{|\omega_{g,n} - \omega_{g,m}|\}$ between different sites, that is, $\delta_{\omega} \gg \Omega_{\alpha}\Omega_{\beta}/(4\Delta^2)$, the time-dependent processes will be highly

off-resonant, yielding the ideal Hamiltonian $H_{xy}(t) \approx H_{xy,0}$. In practical situations, δ_ω will be a limited resource because of the requirement for large field gradient over the distance of a PCW unit cell. Thus, in *SI Appendix F: Error Reduction and Analysis*, we discuss errors created by the time-dependent processes, and strategies to minimize the errors.

As a last remark, if we explicitly write down the phase dependence of the Raman pump in Eq. S23, it follows that $J_{m,n} \equiv |J_{m,n}|e^{i\mathbf{k}_L \cdot \mathbf{r}_{m,n}}$ (and now $J_{m,n} = J_{n,m}$ for $\mathbf{k}_L \cdot \mathbf{r}_{m,n} = 0$). If the illumination is not perfectly transverse, that is, $\mathbf{k}_L \cdot \mathbf{r}_{m,n} \neq 0$, then $H_{xy,0}$ acquires spatial-dependent, complex coupling coefficients:

$$H_{xy,0} = \sum_{m,n>m}^N J_{m,n} \left(e^{i\mathbf{k}_L \cdot \mathbf{r}_{m,n}} \sigma_{gs}^m \sigma_{sg}^n + e^{-i\mathbf{k}_L \cdot \mathbf{r}_{m,n}} \sigma_{gs}^n \sigma_{sg}^m \right), \quad [\text{S25}]$$

which gives us the possibility to engineer geometrical phases and nontrivial topological spin models. We also note that, in the above simple expression, we are assuming $\mathbf{k}_\alpha = \mathbf{k}_L$ being a constant for all different sidebands Ω_α .

Independent Control of XX and YY Interactions. So far, we have been able to engineer full control of spin-exchange or XY Hamiltonians. In this section, we will show how by slight modification of the atomic-level structure, we can engineer the XX and YY terms independently. In particular, we use a butterfly-like structure as depicted in Fig. 3B, where there are two transitions coupled to the GMs, that is, $|g\rangle \leftrightarrow |e\rangle$ and $|s\rangle \leftrightarrow |\bar{e}\rangle$, and two different multifrequency Raman fields, $\Omega_g(t)$ and $\Omega_s(t)$. Assuming that we have copropagating beams or perfectly transverse illumination, that is, $\mathbf{k}_L \cdot \mathbf{r}_{m,n} = 0$, we can adiabatically eliminate the excited states $|e\rangle$ and $|\bar{e}\rangle$ following a similar procedure as in the previous section (Eq. S11) to obtain an effective light-matter Hamiltonian:

$$H_{\text{eff,lm}}(t) = - \sum_{\mathbf{k}, n} \frac{g_{\mathbf{k}}(\mathbf{r}_n) \Omega(t)}{2\Delta} a_{\mathbf{k}} \left(\sigma_{sg}^n + e^{-i\phi_{gs}} \sigma_{gs}^n \right) e^{i(\omega_L - \omega_{\mathbf{k}} - \omega_{g,n})t} + \text{h.c.}, \quad [\text{S26}]$$

where we assumed that $\Omega_s(t)/\Delta_s = \Omega_g(t)e^{i\phi_{gs}}/\Delta_g \equiv \Omega(t)/\Delta$, $\Delta_{sg} = \omega_e - \omega_{L,sg}$, and ϕ_{gs} is the relative phase between the two multifrequency Raman fields that can be adjusted at will.

Adiabatically eliminating the photonic modes under all of the approximations that we used in the previous section, we arrive at an effective Hamiltonian:

$$H_{xx,yy,0} = \sum_{m,n>m}^N \left[J_{m,n} \left(\sigma_{gs}^m + e^{i\phi_{gs}} \sigma_{sg}^m \right) \left(\sigma_{sg}^n + e^{-i\phi_{gs}} \sigma_{gs}^n \right) + \text{h.c.} \right], \quad [\text{S27}]$$

which, depending on the phase ϕ_{gs} , can drive either X or Y component, that is, $(\sigma_{gs}^m \pm \sigma_{sg}^m)$, or more exotic combinations for general ϕ_{gs} . Moreover, if the two pump beams are not copropagating, they create spatial-dependent phases ϕ_{gs} . This can create site-dependent XX , YY , or XY terms.

Stroboscopic Engineering of ZZ Interactions. One way to engineer H_{ZZ} from pure XY terms is to notice that $R_x(\pm\pi/2) (\sigma_x^n \sigma_x^m + \sigma_y^n \sigma_y^m) R_x^\dagger(\pm\pi/2) = \sigma_x^n \sigma_x^m \mp \sigma_z^n \sigma_z^m$ and $R_y(\pm\pi/2) (\sigma_x^n \sigma_x^m + \sigma_y^n \sigma_y^m) R_y^\dagger(\pm\pi/2) = \sigma_y^n \sigma_y^m \pm \sigma_z^n \sigma_z^m$, where we have used the following notation to characterize rotations along the \mathbf{n} axis, that is, $R_{\mathbf{n}}(\theta) = e^{i\sigma_{\mathbf{n}}\theta/2}$. This is particularly useful when both XY and ZZ interactions have the same coupling strengths (e.g., the Haldane–Shastry model). For engineering ZZ terms in a generic spin Hamiltonian, one can apply spin rotations

$R_y(\pi/2)$, such that $R_y(\pi/2) \sigma_x R_y^\dagger(\pi/2) = \sigma_z$, to transform arbitrary XX terms into desired ZZ interactions. Spin rotation can be realized, for example, with a collective microwave driving $H_{\text{mw}} = \sum_n ((\Omega_{\text{mw}}/2) \sigma_{sg}^n + \text{h.c.})$, in which a $\pi/2$ -microwave pulse rotates the basis $\{|g\rangle_n, |s\rangle_n\} \rightarrow \{(|g\rangle_n + |s\rangle_n)/\sqrt{2}, (-|g\rangle_n + |s\rangle_n)/\sqrt{2}\}$.

Thus, an H_{XXZ} Hamiltonian can be simulated using the following stroboscopic evolution: $\{H_{XY}, H_{ZZ}, H_{XY}, H_{ZZ}, \dots\}$ in N_t step as schematically depicted in Fig. 4. The unitary evolution in each step $\delta t = t/N_t$ is given by the following:

$$e^{-i(H_{XY}+H_{ZZ})\delta t} \approx e^{-iH_{XY}\delta t} e^{-iH_{ZZ}\delta t} \left(1 - \frac{i[H_{XY}, H_{ZZ}]\delta t^2}{2} \right), \quad [\text{S28}]$$

where we see that the leading error is $O(\delta t^2)$. When repeating this step N_t times, the leading error in the evolution can be bounded by the following:

$$E_2 \leq \frac{\|[H_{XY}, H_{ZZ}]\| t^2}{2N_t}, \quad [\text{S29}]$$

for $N_t \gg 1$. It can be shown (104) that higher-order error terms give smaller error bounds. Because of long-range interactions, the commutator $[H_{XY}, H_{ZZ}]$ contains up to $N(N-1)(N-2)$ terms that are different from 0. Thus, the scaling of the error in the limit of $N \gg 1$ is approximately given by the following:

$$E_2 \leq \frac{N(RJt)^2}{N_t}, \quad [\text{S30}]$$

where $J = \max[J_{m,n}]$ is the largest energy scale of the Hamiltonian we want to simulate, and R is the approximate number of atoms coupled through the interaction. For example, if $J_{m,n}$ is a nearest neighbor interaction, $R = 1$. If $J_{m,n} \propto 1/|m-n|^\eta$, then $R \propto \sum_{n=1}^N 1/|n|^\eta$, which typically grows much slower than N . Because $E_2 \propto 1/N_t$, the Trotter error in N_t steps can in principle be decreased to a given accuracy ϵ by using enough steps, that is, $N_t \geq N(RJt)^2/\epsilon$.

More complicated stroboscopic evolutions may lead to a more favorable error scaling (64–66), although in real experiments there will be a trade-off between minimizing the Trotter error and the fidelity of the individual operations to achieve H_{XY} and H_{ZZ} . As this will depend on the particular experimental setup, we will leave such analysis out of current discussions. For illustration, we will only consider the simplest kind of stroboscopic evolution that we depicted in Fig. 4.

SI Appendix B: Proper Choice of Ground-State Energy Shifts in 2D Models

For generic 2D lattice models, we need to introduce ground-state energy shifts between sites (m, n) separated by $\mathbf{r}_{m,n} = \mathbf{r}_m - \mathbf{r}_n$ to engineer the interaction between them. The energy shifts need to be unique for specific site separation vector $\mathbf{r}_{m,n}$, but should be independent of \mathbf{r}_m to preserve translational invariance, which is generally required for spin lattice models. To do this, we can introduce a linear magnetic field gradient $\nabla B \cdot \mathbf{a}_l \equiv B_l$, where \mathbf{a}_l ($l = 1, 2$) are the Bravais vectors of a unit cell. We require that the ratio $q = B_1/B_2$ of B-field gradients along two Bravais vectors be an irrational number such that, for any $\mathbf{r}_n = (n_x, n_y)$ with $n_x, n_y \in \mathbb{Z}$, $\omega_{g,n} = \mu_B(n_x \times q + n_y)B_2$ is a unique number. As a result, each sideband can only induce a resonant interaction at a specific separation $\mathbf{r}_{m,n}$. Moreover, we also need to ensure that there exists no \mathbf{r}_m such that $|\omega_{g,m} - \omega_{g,n}| \lesssim J_{m,n}$ that can lead to

¹More precisely, $[H_{XY}, H_{ZZ}] = -2 \sum_{m,n}^N J_{m,n}^y \Delta_{m,n}^z \sigma_{gs}^m \sigma_{sg}^n$, where $\Delta_{m,n}^z \equiv \sum_{q \neq m,n} (J_{q,m}^z - J_{q,n}^z) \sigma_{qz}^2$. Assuming a highly frustrated state, we simply estimate that $|\langle \Delta_{m,n}^z \rangle| \lesssim JR$ and $\|[H_{XY}, H_{ZZ}]\| \leq 2(JR)^2$.

significant time-dependent terms in Eq. 6 of the main text. In general, for a finite-size system, this situation can be avoided.

SI Appendix C: Pump Field Configurations for Engineering a Chiral-Flux Square Lattice Model

In this section, we explicitly write down the time-dependent electric field $\mathbf{E}(\mathbf{r}_n, t)$ that generates the desired Raman field $\Omega(t) \equiv \langle s | \mathbf{d} \cdot \mathbf{E}^* | e \rangle$ for the chiral-flux Hamiltonian, Eq. 15, discussed in the main text. We have $\mathbf{E}(\mathbf{r}_n, t) = \hat{z}[\varepsilon_x(t)e^{i\hat{k}\hat{x} \cdot \mathbf{r}_n} + \varepsilon_y(t)e^{i\hat{k}\hat{y} \cdot \mathbf{r}_n}]e^{-i\omega_L t}$, where $\langle s | \mathbf{d} | e \rangle$ is the transition dipole moment. For the field propagating along \hat{y} , the amplitude reads as follows:

$$\varepsilon_y(t) = \varepsilon_0 + \varepsilon_1(e^{-i\delta_x t} - e^{-i\delta_y t}) + \varepsilon_3(e^{-2i\delta_x t} + e^{-2i\delta_y t}). \quad [\text{S31}]$$

For the field propagating along \hat{x} , we similarly require the following:

$$\varepsilon_x(t) = i\zeta\varepsilon_1(e^{-i\delta_x t} + e^{-i\delta_y t}) + \varepsilon_2(e^{-i\delta_{xy} t} - e^{-i\delta_{y*} t}). \quad [\text{S32}]$$

Each term in Eqs. S31 and S32 contributes to specific sideband in the Raman field and $|\Omega_\alpha| = \langle s | \mathbf{d} \cdot \hat{z} | e \rangle \varepsilon_\alpha$. Pairing individual sidebands to the main Raman field introduced by the leading term $\varepsilon_0 \gg \varepsilon_{1,2,3}$ leads to the desired spin-exchange interactions as discussed in the main text.

We note that there are more ways other than Eqs. S31 and S32 to engineer the spin Hamiltonian. It is also possible to introduce both blue-detuned ($\delta_\alpha > 0$) and red-detuned ($\delta_{-\alpha} = -\delta_\alpha$) sidebands in the Raman field to control the same spin-exchange term. That is,

$$J_{m,n} = \tilde{J} \left[X_0(\mathbf{r}_n) X_\alpha^*(\mathbf{r}_m) + X_0^*(\mathbf{r}_m) X_{-\alpha}(\mathbf{r}_n) \right], \quad [\text{S33}]$$

which has contributions from X_α and $X_{-\alpha}$ of blue and red sidebands, respectively. Arranging both sidebands with equal amplitudes can lead to equal contributions in the engineered coupling coefficient. This corresponds to replacing frequency shifts $e^{-i\delta_{at}}$ in Eqs. S31 and S32 with amplitude modulations $\cos \delta_{at}$. We may replace the fields by the following:

$$\varepsilon_y(t) = \varepsilon_0 + \frac{\varepsilon_1}{2}(\cos \delta_x t - \cos \delta_y t) + \frac{\varepsilon_3}{2}(\cos 2\delta_x t + \cos 2\delta_y t), \quad [\text{S34}]$$

$$\varepsilon_x(t) = i\zeta \frac{\varepsilon_1}{2}(\cos \delta_x t + \cos \delta_y t) + \frac{\varepsilon_2}{2}(\cos \delta_{xy} t - \cos \delta_{y*} t). \quad [\text{S35}]$$

SI Appendix D: Pump Field Configurations for Engineering a Topological Spin Model in a Brick Wall Lattice

In this section, we describe in detail how to engineer Haldane's topological spin model, Eq. 17 of the main text,

$$H = t_1 \sum_{\langle m, n \rangle} \left(\sigma_m^\dagger \sigma_n + \text{h.c.} \right) + t_2 \sum_{\{m, n\}} \left(e^{i\phi_{mn}} \sigma_m^\dagger \sigma_n + \text{h.c.} \right), \quad [\text{S36}]$$

in a brick wall configuration. Introducing a strong pump field of amplitude Ω_0 , propagating along \hat{y} , we can engineer the interaction terms one-by-one as the following:

- Uniform NN coupling along \hat{y} : This term can be realized with a sideband of detuning δ_y and $X_y(\mathbf{r}_n + \Delta \mathbf{r}_y) = -(|\Omega_1|/2\Delta)e^{-i(n_y+1)\pi}$, pairing with the strong pump field $X_0(\mathbf{r}_n) = (|\Omega_0|/2\Delta)e^{-in_y\pi}$, which propagates along \hat{y} . The resulting coupling coefficient is $t_1 = \tilde{J}|X_0||X_y|$. This term can also be extended to engineer nonuniform coupling coefficients; see the following discussion.
- Checkerboard-like NN coupling along \hat{x} : We introduce a sideband of detuning δ_x and amplitude $X_x(\mathbf{r}_n + \Delta \mathbf{r}_x) =$

$(|\Omega|/4\Delta)[e^{-in_y\pi} + \zeta e^{-i(n_x+1)\pi}]$, formed by two fields propagating along \hat{y} and \hat{x} , respectively. If both fields have the same amplitude ($\zeta = 1$), they either add up or cancel completely, depending on whether $n_x + n_y$ is odd or even. The resulting coupling rate is real with amplitude as follows:

$$J_{m,n} = \tilde{J} X_0 X_x^* = \frac{t_1}{2} [1 - (-1)^{n_x - n_y}], \quad [\text{S37}]$$

and vanishes exactly in a checkerboard pattern. If one applies the same trick toward NN coupling along \hat{y} , but with $\zeta \neq 1$, the coupling amplitude also modulates in a checkerboard pattern. Essentially, all three NN terms around a brick wall vertex can be independently controlled, opening up further possibility to engineer, for example, Kitaev's honeycomb lattice model (87, 88).

- Complex NNN and NNNN couplings: The NNNN terms can be similarly generated by using a sideband of detuning $2\delta_y$, and $X_{2y}(\mathbf{r}_n + \Delta \mathbf{r}_{2y}) = \frac{|\Omega_2|}{2\Delta} [e^{-i(n_y+2)\pi} + i\zeta e^{-in_y\pi}]$, formed by two initially $\pi/2$ out-of-phase fields propagating, respectively, along \hat{y} and \hat{x} . The same trick can be used for NNN couplings using sidebands of detunings δ_{xy}, δ_{y*} respectively. The coupling phase ϕ can be arbitrarily controlled by the amplitude ratio ζ , as we showed in Eq. 16 in the main text.

To engineer this model, again only two pump beams can introduce all components required in the Raman field. We can write down the \hat{x} , \hat{y} -propagating fields with amplitude modulations (that is, with equal blue- and red-sideband contributions); for the field propagating along \hat{y} , we have the following:

$$\begin{aligned} \varepsilon_y(t) = & \varepsilon_0 + \varepsilon_1 \left(\frac{1}{2} \cos \delta_x t - \cos \delta_y t \right) \\ & + \varepsilon_2 (\cos 2\delta_y t - \cos \delta_{xy} t - \cos \delta_{y*} t), \end{aligned} \quad [\text{S38}]$$

and, for the field propagating along \hat{x} , we require the following:

$$\varepsilon_x(t) = \frac{\varepsilon_1}{2} \cos \delta_x t - i\zeta \varepsilon_2 (\cos 2\delta_y t + \cos \delta_{xy} t - \cos \delta_{y*} t). \quad [\text{S39}]$$

One may similarly replace amplitude modulations $\cos \delta_{at}$ by frequency modulation $e^{-i\delta_{at}}$ to engineer the spin model, as in Eqs. S31 and S32.

SI Appendix E: PCW and Pump Field Configurations for Engineering an XXZ Spin Hamiltonian with $1/r^\eta$ Interaction

We describe how to engineer an XXZ Hamiltonian, which is typically written as follows:

$$\begin{aligned} H_{XXZ} = & -B \sum_n \sigma_n^z + \sum_{n < m} \frac{J}{|\mathbf{r}_n - \mathbf{r}_m|^\eta} [\cos(\theta) \sigma_n^z \sigma_m^z \\ & + \sin(\theta) (\sigma_n^x \sigma_m^x + \sigma_n^y \sigma_m^y)], \end{aligned} \quad [\text{S40}]$$

where an effective magnetic field B that controls the number of excitations can be introduced by the detuning of addressing beams; the parameter θ determines the relative strength between the ZZ and XY interactions.

We can simulate any η and θ in a 2D PCW as follows:

- First, we require the decay length scale ξ to be sufficiently large such that GM photon coupling strength $\tilde{J}(\mathbf{r}_{m,n})$ is only limited by the energy spread in the low-dimensional reservoir. For example, in 2D with quadratic dispersion as depicted in Fig. 1D of the main text, one can simulate any interaction that decays faster than $K_0(|\mathbf{r}_{m,n}|/\xi) \approx \log(\xi/|\mathbf{r}_{m,n}|)$, where $K_0(x)$ is the

modified Bessel function of the second kind (36, 37) (*SI Appendix A: Complete Derivation of Final Time-Dependent Hamiltonian*).

- Then, to simulate the $|\mathbf{r}_n - \mathbf{r}_m|^{-\eta}$ dependence, we introduce a linear magnetic field gradient ∇B or linear ground-state energy shifts as described in *SI Appendix B: Proper Choice of Ground-State Energy Shifts in 2D Models*.
- Thus, as we did in the previous discussions, we introduce a strong pump field of amplitude Ω_0 together with N_d auxiliary fields Ω_α of detuning δ_α to cover all of the different separations $\mathbf{r}_{m,n}$. For example, to simulate a square lattice of $n_s \times n_s$ ($=N$) atomic spins, we can see that the number of different distances grows as $N_d = (n_s(n_s + 1) - 2)/2$, linearly proportional to the number of atoms $N_d \propto N$.
- Finally, the parameter θ that determines the ratio between ZZ and XY interaction can be controlled by using different pump intensities when doing the stroboscopic evolution.

SI Appendix F: Error Reduction and Analysis

Engineering a Two-Step Hamiltonian. As derived in *SI Appendix A: Complete Derivation of Final Time-Dependent Hamiltonian*, the resulting time-dependent couplings introduced by a multifrequency pump is $H(t) = \sum_p H_p e^{ip\delta t}$, where H_p represents the part in the Hamiltonian that oscillates with frequency $p\delta$. The time-dependent Hamiltonian has a period $T = 2\pi/\delta$, and it can be shown that the effective Hamiltonian that repeats every time period T ; that is, $e^{-iH_{\text{eff}}T}$, where the measurements would take place in an experiment, is given by the following (99):

$$H_{\text{eff},1} \approx H_0 + \frac{1}{\delta} \sum_p \frac{[H_p, H_{-p}]}{p} + \frac{1}{2\delta^2} \sum_p \frac{[[H_p, H_0], H_{-p}] + [[H_{-p}, H_0], H_p]}{p^2}. \quad [\text{S41}]$$

This means that, if we apply the multifrequency pumps just as we explained in the previous sections, the leading error would be on the order of J^2/δ , where J is the interaction strength that we want to simulate. However, we also observe that the leading error term $\sum_p [H_p, H_{-p}]/(p\delta)$ vanishes if $H_p = \pm H_{-p}$. In other words, first-order error vanishes if H_p is either symmetric or anti-symmetric under time reversal operation \mathcal{T} . Although the original Hamiltonian $H(t)$ does not necessarily possess such symmetry, it is possible to introduce a two-step periodic operation $H_{\text{2step}} = \{H, \mathcal{T}H, H, \mathcal{T}H, \dots\}$ to cancel the first-order error while keeping the time-independent part $H_{\text{2step},0} = H_0$ identical. This reduces the leading error to the order of J^3/δ^2 .

To achieve the time reversal operation, we must reverse the phase of the driving lasers, as well as the sign of the energy offsets between the atoms. Specifically, we can engineer the two-step Hamiltonian as follows:

- After applying a proper magnetic (or Stark shift) gradient to ensure a position-dependent energy shift, we apply sidebands using either frequency or amplitude modulations to engineer the Hamiltonian H_0 following Eq. S23.
- After a time $T = 2\pi/\delta$, we flip the sign of the gradient. In 1D, if $\omega_{g,n} - \omega_{g,m} = |n - m|\delta$, then we switch to $\omega_{g,n} - \omega_{g,m} = -|n - m|\delta$. Meanwhile, we also reverse the propagation direction of the Raman fields such that $X_\alpha \rightarrow X_\alpha^*$. As a result, all of the time-dependent Hamiltonians H_p , $\forall p \neq 0$, become H_{-p} in the second step; whereas the time-independent Hamiltonian H_0 remains identical. After holding for an evolution time $T = 2\pi/\delta$, we repeat the first step.

To formally prove that the above idea leads to smaller error, we can write our two-step periodic Hamiltonian as follows:

$$H_{\text{2step}}(t) = H(t)T(t) + H(-t)T(t-T), \quad [\text{S42}]$$

where $T(t)$ is a periodic square-wave envelope, controlling the on and off of $H(t)$ at time interval $[0, T]$ within a period $2T$. $T(t)$ can be expanded as follows:

$$T(t) = \frac{1}{2} + \frac{1}{\pi i} \sum_{m \text{ odd}} \frac{(e^{im\delta t/2} - e^{-im\delta t/2})}{m}, \quad [\text{S43}]$$

where $m = 1, 3, \dots$. Plugging the expansion $H(t) = \sum_p H_p e^{ip\delta t}$ into Eq. S42, we now have the following:

$$H_{\text{2step}}(t) = \frac{1}{2} \sum_p \left[H_p e^{ip\delta t} \left(1 + \frac{2}{\pi i} \sum_{m \text{ odd}} \frac{(e^{im\delta t/2} - e^{-im\delta t/2})}{m} \right) + H_p e^{-ip\delta t} \left(1 - \frac{2}{\pi i} \sum_{m \text{ odd}} \frac{(e^{im\delta t/2} - e^{-im\delta t/2})}{m} \right) \right]. \quad [\text{S44}]$$

Writing $H_{\text{2step}}(t) = \sum_p \tilde{H}_p e^{ip(\delta/2)t}$, the Fourier components \tilde{H}_p of the two-step periodic Hamiltonian are as follows:

$$\tilde{H}_{p(\text{even})} = \frac{1}{2} (H_{p/2} + H_{-p/2}), \quad [\text{S45}]$$

$$\tilde{H}_{p(\text{odd})} = \frac{1}{\pi i} \sum_{m \text{ odd}} \frac{1}{m} (H_{(p-m)/2} - H_{-(p-m)/2} + H_{(p+m)/2} - H_{-(p+m)/2}). \quad [\text{S46}]$$

So we have $\tilde{H}_p = (-1)^p \tilde{H}_{-p}$ and the leading order error in Eq. S41 vanishes. According to the Floquet theory, we arrive at an effective time-independent Hamiltonian $H_{\text{eff},2}$ at every time interval $T_2 = 4\pi/\delta$,

$$H_{\text{eff},2} = H_0 + H_{\text{err},2} \approx H_0 + \frac{4}{\delta^2} \sum_p (-1)^p \frac{[[\tilde{H}_p, H_0], \tilde{H}_p]}{p^2}. \quad [\text{S47}]$$

Time-Dependent Stark Shifts in the Error Analysis. In the previous discussions, we have dropped the contribution of the time-dependent Stark shifts:

$$H_{\text{ac}}(t) = - \sum_n \sum_{\alpha > \beta}^{m_p-1} \Re \left[\frac{\Omega_\alpha \Omega_\beta^*}{2\Delta} e^{i\tilde{\omega}_{\alpha\beta} t} \right] \sigma_{ss}^n, \quad [\text{S48}]$$

where $\tilde{\omega}_{\alpha\beta} = \tilde{\omega}_\alpha - \tilde{\omega}_\beta$. In the following, we discuss its role in the effective Hamiltonian, using the Floquet error analysis.[‡] The Fourier coefficients of the Stark shifts can be written as follows:

$$H_{\text{ac},p} = \sum_n A_p^n \sigma_{ss}^n, \quad [\text{S49}]$$

where the on-site amplitude

$$A_p^n = -\Delta \sum_{\alpha \neq \beta} X_\alpha X_\beta^* \delta(\tilde{\omega}_{\alpha\beta} - p\delta); \quad [\text{S50}]$$

A_p^n may be site dependent if the phase differences between the Raman fields Ω_α vary across sites. Comparing Eq. S50 with Eq. 8 of the main text, we see that $A_p^n \sim O(J\Delta/\tilde{J})$ may be even larger

[‡]Here, we discuss a special case where only $|s\rangle$ state is shifted. For a general case when both $|g\rangle$ and $|s\rangle$ states are shifted, see later discussion.

than the engineered interaction $J \equiv \max[J_{m,n}]$ if $\Delta \gtrsim \tilde{J}$. In the two-step driving scheme, we replace the amplitude A_p^n by \tilde{A}_p^n according to Eqs. S45 and S46.

As discussed in the previous section, with two-step driving, the leading Stark shift error contribution only appears in the second order:

$$H_{\text{err},2} \approx \frac{4}{\delta^2} \sum_p (-1)^p \frac{[[\tilde{H}_p + \tilde{H}_{\text{ac},p}, H_0], \tilde{H}_p + \tilde{H}_{\text{ac},p}]}{p^2}, \quad [\text{S51}]$$

where $\tilde{H}_{\text{ac},p}$ are the Fourier coefficients of the two-step Stark-shift Hamiltonian. Only the following nested commutators, $[[\tilde{H}_{\text{ac},p}, H_0], \tilde{H}_{\text{ac},p}]$, $[[\tilde{H}_{\text{ac},p}, H_0], \tilde{H}_p]$, and $[[\tilde{H}_p, H_0], \tilde{H}_{\text{ac},p}]$ are related to the time-dependent Stark shifts, and should be evaluated in various configurations as follows.

Generic Hamiltonians with translational invariance. By translational invariance, we mean that there are no site-dependent spin interactions, and the spin-exchange coefficients remain identical as we offset the spin index by one or more. This means that all components in the pump field should drive the system with uniform optical phases as in the Haldane-Shastry model discussed above. The resulting Fourier coefficients $\tilde{H}_{\text{ac},p} = \tilde{A}_p \sum_n \sigma_{ss}^n$ would have identical effect on all spins (\tilde{A}_p being a constant amplitude). As a result, the above-mentioned commutators vanish, suggesting that the error by $\tilde{H}_{\text{ac}}(t)$ averages out to zero in the Floquet picture. In the butterfly scheme, however, both $|g\rangle$ and $|s\rangle$ states are pumped and they may be shifted differently. This leads to slight modifications in the engineered XX and YY terms (see later discussion).

Models containing sublattices. For topological models that contain sublattices, as in our examples, the pump fields are not perfectly transverse and Stark shifts are site dependent, resulting in nonvanishing error. However, we also note that the coupling coefficients appearing in the commutators $[[\tilde{H}_{\text{ac},p}, H_0], \tilde{H}_{\text{ac},p}]$ and $[[\tilde{H}_p, H_0], \tilde{H}_{\text{ac},p}]$ ($[[\tilde{H}_{\text{ac},p}, H_0], \tilde{H}_p]$) are on the order of $J|\Omega|^4/\Delta^2$ and $J^2|\Omega|^2/\Delta$, respectively. For realistic PCW realizations, we may set $\tilde{J}/\Delta \gtrsim O(1)$. Because $A_p^n/J_{m,n} \sim O(\Delta/\tilde{J})$, the energy scales of the commutators are all on the order $\lesssim J^3$, and the energy scale in $H_{\text{err},2}$ will be $\lesssim J^3/\delta^2$. Therefore, for $\delta \gg J$, the Stark shift terms may be ignored.

Stark shift-dominated regime. It may be possible that our sublattice models be purposely driven with large-amplitude pumps such that $|\Omega|^2/\Delta \gtrsim \delta$. Stark shift contributions would become important in the resulting spin dynamics. However, if we choose a large pump detuning $\Delta > \tilde{J}$, the dominant error contribution [recall that $J \sim (\tilde{J}/\Delta)(|\Omega|^2/\Delta)$] comes from the $[[\tilde{H}_{\text{ac},p}, H_0], \tilde{H}_{\text{ac},p}]$ term, which can be written in the following simple form:

$$\begin{aligned} H_{\text{err},2} &\approx \frac{4}{\delta^2} \sum_p \frac{(-1)^p}{p^2} [[\tilde{H}_{\text{ac},p}, H_0], \tilde{H}_{\text{ac},p}] \\ &\approx \sum_{m,n} \tilde{A}_{m,n} (J_{m,n} \sigma_{gs}^m \sigma_{sg}^n + h.c.). \end{aligned} \quad [\text{S52}]$$

Here, the site-dependent Fourier coefficient is defined as $\tilde{H}_{\text{ac},p} \equiv \sum_n \tilde{A}_p^n \sigma_{ss}^n$ and $\tilde{A}_{m,n} = \sum_p ((4(-1)^{p+1})/\delta^2 p^2) (\tilde{A}_p^m - \tilde{A}_p^n)^2 \neq 0$ in general for interactions $J_{m,n}$ that are not translationally invariant. In a special case that only two sublattices are present, as in our examples, we note that $\tilde{A}_{m,n}$ may only depend on the distance $r_{m,n}$ and is site independent. This “error” term would then uniformly modify the XY coupling strengths to a modified value:

$$J_{m,n} = (1 + \tilde{A}_{m,n}) J_{m,n}. \quad [\text{S53}]$$

The next leading order errors are due to $[[\tilde{H}_p, H_0], \tilde{H}_{\text{ac},p}]/\delta^2$ and $[[\tilde{H}_{\text{ac},p}, H_0], \tilde{H}_p]/\delta^2$ terms, which are on the order of $J^2|\Omega|^2/(\Delta\delta^2)$ and are a factor of $\sim \tilde{J}/\Delta$ smaller than the leading Stark shift contribution. This suggests we can always increase the detuning Δ , while keeping $|\Omega|/\Delta$ constant, to reduce the error contribution.

Time-Dependent Stark Shifts in the Butterfly Scheme. We discuss the error contribution due to time-dependent Stark shifts in the butterfly scheme for independent control of XX or YY interactions (as well as ZZ interaction in stroboscopic evolution). The time-dependent Stark shift is as follows:

$$H_{\text{ac}}(t) = - \sum_n \sum_{\alpha > \beta}^{m_p-1} \Re \left[\frac{\Omega_{g,\alpha} \Omega_{s,\beta}^*}{2\Delta_g} e^{i\tilde{\omega}_{\alpha,\beta} t} \right] \sigma_{gg}^n - \Re \left[\frac{\Omega_{s,\alpha} \Omega_{s,\beta}^*}{2\Delta_s} e^{i\tilde{\omega}_{\alpha,\beta} t} \right] \sigma_{ss}^n, \quad [\text{S54}]$$

where $\tilde{\omega}_{\alpha,\beta} = \tilde{\omega}_\alpha - \tilde{\omega}_\beta$. The Fourier coefficients of the Stark shifts can be written as follows:

$$H_{\text{ac},p} = \sum_n \frac{A_p^n}{\Delta} (\Delta_g \sigma_{gg}^n + \Delta_s \sigma_{ss}^n), \quad [\text{S55}]$$

where $A_p^n = - \sum_{\alpha \neq \beta} (\Omega_{\alpha,\beta}^*/4\Delta) \delta(\tilde{\omega}_{\alpha,\beta} - p\delta)$, and we have used that fact that $|\Omega_{g,\alpha}|/\Delta_g = |\Omega_{s,\alpha}|/\Delta_s = |\Omega_\alpha|/\Delta$. In two-step driving, we replace A_p^n with \tilde{A}_p^n according to Eqs. S45 and S46. We note that states $|g\rangle$ and $|s\rangle$ can be driven differently when $\Delta_g \neq \Delta_s$. This leads to different error comparing to simple Raman driving only on one of the state.

In two-step driving, the leading Stark shift error contribution appears in the second order:

$$H_{\text{err},2} \approx \frac{4}{\delta^2} \sum_p (-1)^p \frac{[[\tilde{H}_p + \tilde{H}_{\text{ac},p}, H_0], \tilde{H}_p + \tilde{H}_{\text{ac},p}]}{p^2}, \quad [\text{S56}]$$

where $\tilde{H}_{\text{ac},p}$ are the Fourier coefficients of the two-step Stark shift Hamiltonian. To simplify the discussion, we discuss XX interaction with $\phi_{gs} = 0$ and the following:

$$H_0 = H_{XX,0} = \sum_{m,n > m}^N J_{m,n} (\sigma_{gs}^m + \sigma_{sg}^m) (\sigma_{sg}^n + \sigma_{gs}^n). \quad [\text{S57}]$$

For illustration, we evaluate the following nested commutators, $[[\tilde{H}_{\text{ac},p}, H_0], \tilde{H}_{\text{ac},p}]$, to access the error contribution due to time-dependent Stark shifts. We find the following:

$$\begin{aligned} [[\tilde{H}_{\text{ac},p}, H_0], \tilde{H}_{\text{ac},p}] &= - \sum_{m,n > m}^N \frac{J_{m,n}}{\Delta^2} (\Delta_g - \Delta_s)^2 \left[(\tilde{A}_p^m + \tilde{A}_p^n)^2 (\sigma_{gs}^m \sigma_{gs}^n \right. \\ &\quad \left. + \sigma_{sg}^m \sigma_{sg}^n) + (\tilde{A}_p^m - \tilde{A}_p^n)^2 (\sigma_{sg}^m \sigma_{gs}^n + \sigma_{gs}^m \sigma_{sg}^n) \right] \end{aligned} \quad [\text{S58}]$$

$$= - \sum_{m,n > m}^N \frac{J_{m,n}}{\Delta^2} (\Delta_g - \Delta_s)^2 \left\{ \left[(\tilde{A}_p^m)^2 + (\tilde{A}_p^n)^2 \right] \sigma_x^m \sigma_x^n - 2 \tilde{A}_p^m \tilde{A}_p^n \sigma_x^m \sigma_x^n \right\}. \quad [\text{S59}]$$

We therefore see that, as long as $\Delta_g = \Delta_s$, there is no error due to time-dependent Stark shifts as a result that both $|g\rangle$ and $|s\rangle$ states are shifted exactly the same way. However, one may find that the atomic-level structure for a butterfly scheme dictates that $\Delta_g \neq \Delta_s$. As a result, we find $[[\tilde{H}_{\text{ac},p}, H_0], \tilde{H}_{\text{ac},p}] \neq 0$ even for translational-invariant models, where $\tilde{A}_p^n \equiv \tilde{A}_p$ are independent of sites. This is in contrast to the case of XY Hamiltonians with the Raman field driving only one ground state. It is, however, still possible to minimize the error contribution by driving with $\tilde{J} > \Delta$ and $\delta \gg J$, as the criterion needed for sublattice models (see main text).

In the case of strong driving with $\Delta_g \neq \Delta_s$ and $\Delta > \tilde{J}$, the commutator $[[\tilde{H}_{ac,p}, H_0], \tilde{H}_{ac,p}]$ can be made as the dominant error contribution. Interestingly, as seen from Eq. S59, this error

term is in fact also driving XX and YY interactions. It is therefore desirable to take the Stark shift contribution into account while finding the proper pump fields to create the target Hamiltonians.

Atom–atom interactions around the band edge of a photonic crystal waveguide

Jonathan D. Hood^{a,b}, Akihisa Goban^{a,b,1}, Ana Asenjo-Garcia^{a,b}, Mingwu Lu^{a,b}, Su-Peng Yu^{a,b}, Darrick E. Chang^c, and H. J. Kimble^{a,b,2}

^aNorman Bridge Laboratory of Physics MC12-33, California Institute of Technology, Pasadena, CA 91125; ^bInstitute for Quantum Information and Matter, California Institute of Technology, Pasadena, CA 91125; and ^cInstitut de Ciències Fotoniques, The Barcelona Institute of Science and Technology, 08860 Barcelona, Spain

Contributed by H. Jeffrey Kimble, June 17, 2016 (sent for review March 7, 2016; reviewed by Eugene Polzik and Dan Stamper-Kurn)

Tailoring the interactions between quantum emitters and single photons constitutes one of the cornerstones of quantum optics. Coupling a quantum emitter to the band edge of a photonic crystal waveguide (PCW) provides a unique platform for tuning these interactions. In particular, the cross-over from propagating fields $E(x) \propto e^{\pm ik_x x}$ outside the bandgap to localized fields $E(x) \propto e^{-\kappa_x |x|}$ within the bandgap should be accompanied by a transition from largely dissipative atom–atom interactions to a regime where dispersive atom–atom interactions are dominant. Here, we experimentally observe this transition by shifting the band edge frequency of the PCW relative to the D₁ line of atomic cesium for $N = 3.0 \pm 0.5$ atoms trapped along the PCW. Our results are the initial demonstration of this paradigm for coherent atom–atom interactions with low dissipation into the guided mode.

quantum optics | nanophotonics | atomic physics

Recent years have witnessed a spark of interest in combining atoms and other quantum emitters with photonic nanostructures (1). Many efforts have focused on enhancing emission into preferred electromagnetic modes relative to vacuum emission, thereby establishing efficient quantum matter–light interfaces and enabling diverse protocols in quantum information processing (2). Photonic structures developed for this purpose include high-quality cavities (3–7), dielectric fibers (8–13), metallic waveguides (14–16), and superconducting circuits (17–19). Photonic crystal waveguides (PCWs) are of particular interest, because the periodicity of the dielectric structure drastically modifies the field propagation, yielding a set of Bloch bands for the guided modes (GMs) (20). For example, recent experiments have shown superradiant atomic emission because of a reduction in group velocity for an atomic frequency near a band edge of a PCW (21).

A quite different paradigm for atom–light interactions in photonic crystals was proposed in the works in refs. 22–25 but has yet to be experimentally explored. In particular, when an atomic transition frequency is situated within a bandgap of a PCW, an atom can no longer emit propagating waves into GMs of the structure. However, an evanescent wave surrounding the atoms can still form, resulting in the formation of atom–photon-bound states (26, 27). This phenomenon has attracted new interest recently as a means to realize dispersive interactions between atoms without dissipative decay into GMs. The spatial range of atom–atom interactions is tunable for 1D and 2D PCWs and set by the size of the photonic component of the bound state (28, 29). Many-body physics with large spin exchange energies and low dissipation can thereby be realized in a generalization of cavity quantum electrodynamics (CQED) arrays (30, 31). Fueled by such perspectives, there have been recent experimental observations with atoms (21, 32, 33) and quantum dots (34, 35) interacting through the GMs of PCWs, albeit in frequency regions outside the bandgap, where GMs are propagating fields.

In this manuscript, we report the observation of collective dispersive shifts of the atomic resonance around the band edge of a photonic crystal. Thermal tuning allows us to control the offset of

the band edge frequency (ν_{BE}) of the PCW relative to the frequency ν_{D1} of the D₁ line of cesium (Cs). In both the dispersive domain [i.e., ν_{D1} outside the bandgap with electric field $E(x) \propto e^{\pm ik_x x}$] and reactive regime [i.e., ν_{D1} inside the bandgap with $E(x) \propto e^{-\kappa_x |x|}$], we record transmission spectra for atoms trapped along the PCW, as illustrated in Fig. 1A.

To connect the features of the measured transmission spectra to underlying atom–atom radiative interactions, we have developed a formalism based on the electromagnetic Green’s function. The model allows us to infer the peak single-atom frequency shift of the atomic resonance $J_{1D}(\Delta_{BE})$ and GM decay rate $\Gamma_{1D}(\Delta_{BE})$ as functions of detuning $\Delta_{BE} = \nu_{D1} - \nu_{BE}$ between the atomic ν_{D1} and band edge ν_{BE} frequencies. From the observation of superradiant emission outside the bandgap, we infer the average number of trapped atoms to be $\bar{N} = 3.0 \pm 0.5$, as described in ref. 21 and *SI Text*. (*SI Text* has thorough descriptions of the design and characterization of the PCW, how to obtain the attenuation coefficient and the band edge position of the PCW, how to generate the atomic spectra fits, and the measurements of atomic decay.) For frequencies inside the bandgap ($\Delta_{BE} = 50$ GHz), the ratio of dissipative to coherent rates is $\mathcal{R} = \Gamma_{1D}/J_{1D} = 0.05 \pm 0.17$ because of the exponential localization of the atomic radiation in the bandgap. For comparison, the prediction for our system from CQED models alone is $\mathcal{R}_{CQED} = 0.30 \pm 0.04$. Other than yielding a more favorable ratio between coherent and dissipative GM rates, PCWs offer significant advantages compared with conventional cavities as

Significance

In recent years, there has been considerable effort to bring ultracold atoms into the realm of nanophotonics. Nanoscopic dielectric devices offer unprecedented opportunities to engineer novel capabilities for the control of atom–photon interactions. In particular, photonic crystals are periodic dielectric structures that display a photonic bandgap where light cannot propagate and provide a new setting for coherent photon-mediated interactions between atoms with tunable range. Here, we report the initial observation of cooperative atom–atom interactions around the band edge of a photonic crystal waveguide. Our experiment opens the door to fascinating scenarios, such as exploring many-body physics with large spin exchange energies and low dissipation.

Author contributions: J.D.H., A.G., S.-P.Y., and H.J.K. designed research; J.D.H., A.G., A.A.-G., M.L., S.-P.Y., D.E.C., and H.J.K. performed research; J.D.H., A.G., A.A.-G., S.-P.Y., and D.E.C. contributed new reagents/analytic tools; J.D.H., A.G., A.A.-G., M.L., and S.-P.Y. analyzed data; and J.D.H., A.A.-G., and H.J.K. wrote the paper.

Reviewers: E.P., Copenhagen University; and D.S.-K., University of California, Berkeley.

The authors declare no conflict of interest.

Freely available online through the PNAS open access option.

¹Present address: JILA, University of Colorado, Boulder, CO 80309.

²To whom correspondence should be addressed. Email: hkimble@caltech.edu.

This article contains supporting information online at www.pnas.org/lookup/suppl/doi:10.1073/pnas.1603788113/DCSupplemental.

platforms for atom–light interfaces. First, the range of interaction in a PCW is tunable, ranging from effectively infinite to nearest neighbor (28, 29, 36), in contrast to the fixed infinite range of a cavity. Second, because of the multimode nature of PCWs, one can use different GMs as different interaction channels to which the atoms simultaneously couple.

Alligator PCW

Fig. 1A provides an overview of our experiment with atoms trapped near and strongly interacting with the transverse-electric (TE) mode of an alligator PCW. The suspended silicon nitride (SiN) structure consists of $N_{\text{cells}} = 150$ nominally identical unit cells of lattice constant $a = 370$ nm and is terminated by 30 tapering cells on each side, as shown in the SEM images in Fig. 1B. The tapers mode-match the fields of the PCW to the fields of uncorrugated nanobeams for efficient input and output coupling. Design, fabrication, and characterization details are described in refs. 21, 32, and 33. Fig. 1C shows the nominal cell dispersion relations for the TE (polarized mainly along y) and transverse-magnetic (TM) modes (polarized mainly along z). After release of the SiN structure from the silicon (Si) substrate, a low-power CF_4 etch is used to align the lower “dielectric” TE band edge (ν_{BE}) to the Cs D₁ transition ($\nu_{\text{D}1}$). The TM mode has band edges far detuned from the both the Cs D₁ and D₂ lines. In our experiment, the TE mode is used to probe the atoms, whereas the TM mode with approximately linear dispersion serves to calibrate the density and trap properties.

To better understand atomic interactions with the PCW, it is helpful to visualize the spatial profile of the fields generated absent atoms, when light is input from one end. Fig. 2A shows the measured intensity along the length of the PCW as a function of probe detuning $\delta_{\text{BE}} = \nu_p - \nu_{\text{BE}}$ around the band edge, where ν_p is the

probe frequency. The intensity was measured by imaging weak scatterers along the length of the alligator PCW that, after calibration, serve as local probes of the intensity (SI Text). Fig. 2B shows the corresponding finite difference time domain (FDTD) simulated intensity (37). In both images, resonances appear at $\nu_p = \nu_{1,2,3}$ because of the weak cavity formed by the reflections of the tapers. The spatial modulation of the intensity at the resonances caused by the cavity effect is approximated by $|E(x)|^2 \approx \cos^2(\delta k_x x)$, where $\delta k_x = \pi/a - k_x$ is the effective wavevector near the band edge. The n th resonance at frequency ν_n is such that $\delta k_x = n\pi/L$, where L is the effective length of the PCW (including field penetration into the tapers). Fig. 2C shows a plot of $|E(x)|^2$ for a probe input at frequency $\nu_p = \nu_1$ at the first resonance. Inside the bandgap ($\Delta_{\text{BE}} > 0$), the field is evanescent, and $\delta k_x = ik_x$. Fig. 2D plots $|E(x)|^2$ for probe frequency $\nu_p = \nu_{\text{BG}}$ inside the bandgap and shows the exponential decay of the intensity. Using a model for the field in a finite photonic crystal (SI Text), we fit the measured intensity for each frequency in Fig. 2A and B and extract δk_x and κ_x , thereby obtaining the dispersion relations shown in Fig. 2E. Importantly, we determine the band edge frequency for the actual device to be $\nu_{\text{BE}} - \nu_1 = 133 \pm 9$ GHz relative to the readily measured first resonance at ν_1 , which is in good agreement with the FDTD-simulated result of 135 GHz.

Both ν_1 and ν_{BG} are relevant to our measurements of transmission spectra with trapped atoms. The presence of a “cavity” mode at ν_1 implies that the emission of an atom with transition frequency $\nu_{\text{D}1} = \nu_1$ will generate a field inside the PCW with an analogous spatial profile to that of the cavity mode, as shown in Fig. 2C. By contrast, atomic emission in the regime with $\nu_{\text{D}1} = \nu_{\text{BG}}$ within the bandgap will excite an exponentially localized mode centered around the atomic position x_A , as illustrated in Fig. 2F.

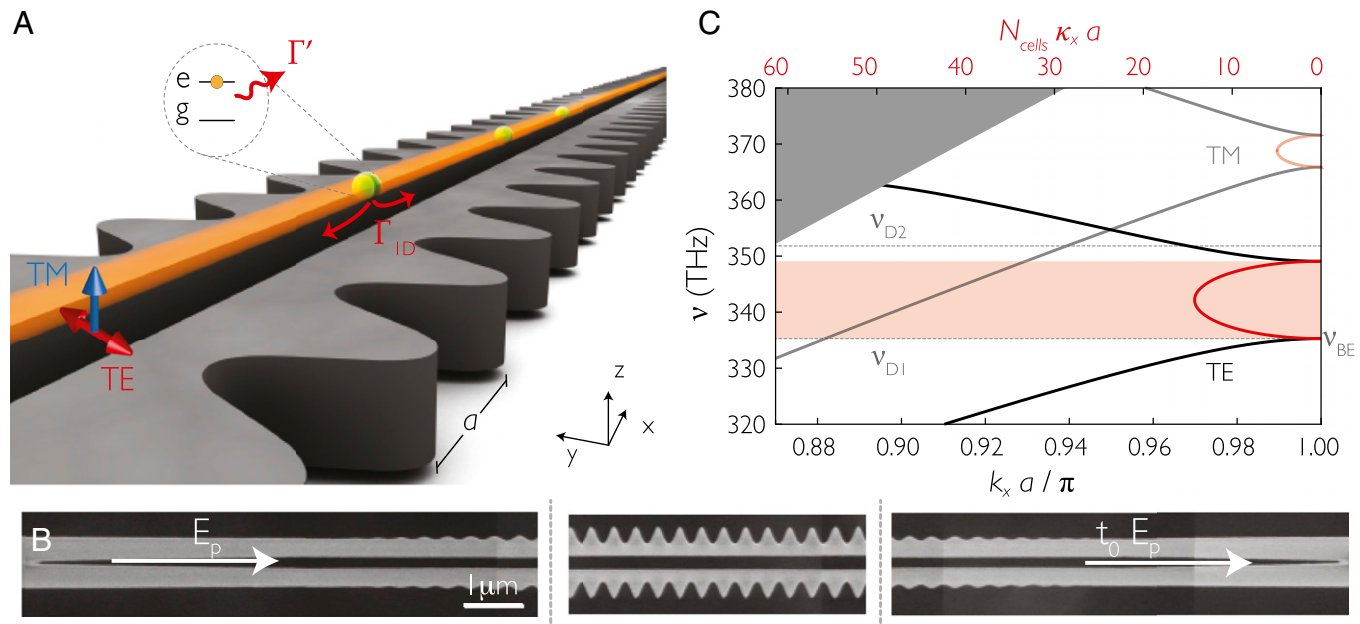


Fig. 1. Description of the alligator PCW. (A) Atoms are trapped above the PCW in an optical dipole trap formed by the reflection of a near-normal incidence external beam (21). The orange cylinder represents the confinement of the atoms, which is $\Delta x_A \simeq \pm 6 \mu\text{m}$ along the axis of the device and $\Delta y_A \simeq \Delta z_A \simeq \pm 30$ nm in the transverse directions (SI Text). The three green spheres represent trapped atoms that interact radiatively through the fundamental TE GM, polarized mainly along y . The decay rate for a single atom into the PCW is Γ_{10} (red arrows), and the decay rate into all other modes is Γ' (wavy red arrow). (B) SEM images of portions of the tapering and PCW sections. The suspended SiN device (gray) consists of 150 cells and 30 tapering cells on each side. The lattice constant is $a = 370$ nm, and thickness is 185 nm. (C) Calculated band structure of the fundamental TE (solid) and TM (translucent) modes using an eigenmode solver (38) and the measured SEM dimensions, which are modified within their uncertainty to match the measured bands. The black curves represent the Bloch wavevector k_x (lower axis). The red curves show the attenuation coefficient κ_x of the field for frequencies in the bandgap (upper axis) and are calculated by means of an analytical model (SI Text). The dotted lines mark the frequencies of the Cs D₁ ($\nu_{\text{D}1} = 335.1$ THz) and D₂ ($\nu_{\text{D}2} = 351.7$ THz) transitions. The dielectric band edge is indicated as ν_{BE} . The pink shaded area represents the TE bandgap. The gray shaded area represents the light cone.

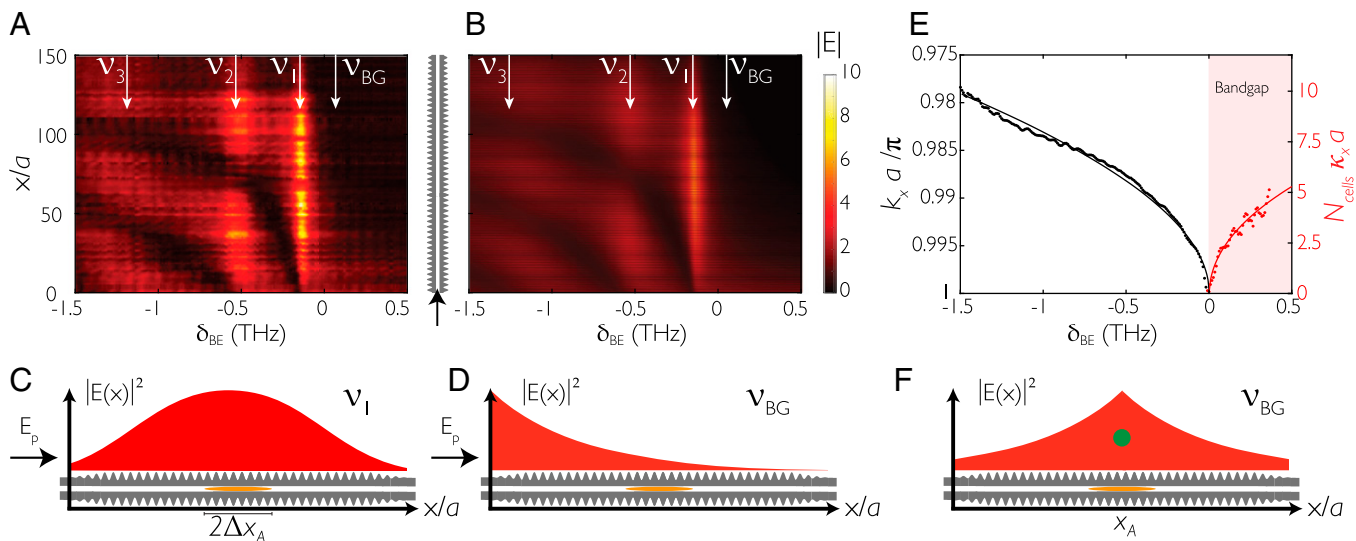


Fig. 2. Characterization of the alligator PCW. (A) Measured and (B) calculated electric field magnitudes along the PCW as functions of position x along the PCW and probe detuning $\delta_{\text{BE}} = \nu_p - \nu_{\text{BE}}$ relative to ν_{BE} for the dielectric band edge. (C and D) GM intensity $|E(x)|^2$ along PCW at two different frequencies: (C) ν_1 for the first cavity resonance showing a resonant “supermode” and (D) ν_{BG} inside the bandgap displaying exponential decay ($N_{\text{cells}}\kappa_x a = 2.0$ at ν_{BG}). For clarity, the number of cells of the nominal and tapering sections is decreased by a factor of five, and the Bloch periodicity ($a = 370$ nm), although present, is not shown in the intensity. The orange ovals represent the confinement of the atoms in the optical trap above the PCW, which is $\Delta x_A \simeq \pm 6$ μm along the x axis of the device and $\Delta y_A \simeq \pm 30$ nm, with a PCW gap width of 220 nm. (E) Dispersion relation for the projected wavevector k_x and attenuation constant κ_x vs. probe detuning δ_{BE} deduced for the PCW obtained by fitting the data in A to a model of the device (SI Text). The shaded pink area represents frequencies inside the bandgap. (F) Plot of the exponentially localized emission $e^{-2\kappa_x|x-x_A|}$ from an atom (green sphere) at position x_A with transition frequency $\nu_{\text{D1}} = \nu_{\text{BG}}$ inside the bandgap.

Experiment

Cs atoms are trapped above the surface of the alligator PCW, as shown in Fig. 1A, using a similar experimental setup to that reported in ref. 21. As described in more detail in ref. 21, the decay rate $\Gamma_{1\text{D}}$ into the GM is exponentially sensitive to the trap position above the surface of the alligator PCW. Our calculations and measurements of $\Gamma_{1\text{D}}$ agree with COMSOL simulations (38) of the trap position, and thus, we are able to determine that the Cs atoms are trapped 145 ± 15 nm above the surface of the alligator PCW. Atoms are cooled and trapped in a magneto-optical trap (MOT) around the PCW and then loaded into a dipole trap formed by the reflection from the device of a frequency red-detuned side illumination (SI) beam. The SI beam has a waist of 50 μm , and the polarization is aligned along the x axis for maximum reflection from the PCW. We measure a $1/e$ trap lifetime of ~ 30 ms, and we estimate an atom temperature of ~ 30 μK from time of flight measurements. From the trap simulations (details are in SI Text), we infer that the atoms are confined to a region 145 nm above the surface with dimensions $\Delta x_A \simeq \pm 6$ μm and $\Delta y_A \simeq \Delta z_A \simeq \pm 30$ nm. The simulations predict that more energetic atoms escape the trap and collide into the structure, because the weakest direction of the trap is along the diagonals of the y - z plane due to Casimir-Polder forces.

To estimate the average number of trapped atoms, we measure the superradiant atomic decay rate when the atom frequency ν_{D1} is tuned to the first resonance ν_1 of the PCW (Fig. 2C) (21). Because of the strong dissipative interactions between the atoms and with $J_{1\text{D}} \approx 0$, the collective decay rate is enhanced compared with the single-atom decay rate, and we infer an average atom number of $\bar{N} = 3.0 \pm 0.5$ (SI Text). In the low-density limit $\bar{N} \ll 1$, the measured decay rate corresponds to that of a single atom. We then measure a GM decay rate $\Gamma_{1\text{D}} = (1.5 \pm 0.2) \Gamma_0$, which is in good agreement with the FDTD simulations at the calculated trap location (SI Text).

After the atoms are loaded into the trap, we send a weak 5-ms probe beam E_p with frequency ν_p in either the TE or TM GM through the

PCW and record the transmitted intensity $|t(\nu_p) E_p(\nu_p)|^2$. The probe beam scans near the Cs $6S_{1/2}, F=3 \rightarrow 6P_{1/2}, F'=4$ transition. Each experimental cycle runs at a fixed detuning $\Delta_A = \nu_p - \nu_{\text{D1}}$

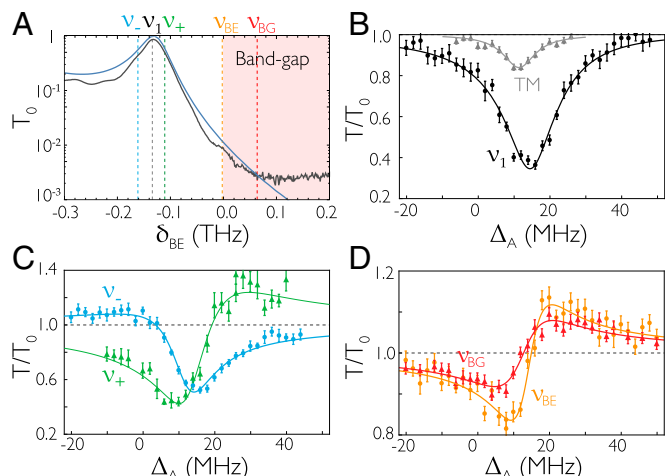


Fig. 3. Transmission spectra of the PCW (A) without and (B–D) with trapped atoms. (A) Measured (black) and FDTD-simulated (blue) transmission spectra of the PCW without atoms as a function of the probe detuning from the band edge frequency, $\delta_{\text{BE}} = \nu_p - \nu_{\text{BE}}$. There is a minimum extinction of 25 dB for the transmitted signal because of fabrication imperfections. (B–D) Transmission spectrum for $\bar{N} = 3.0 \pm 0.5$ trapped atoms vs. probe detuning $\Delta_A = \nu_p - \nu_{\text{D1}}$ at several frequencies around the band edge. The solid lines are fits using the transmission model in Eq. 4 averaged over atom positions and different atom numbers. In B, the Cs D₁ line is aligned to the first cavity resonance ν_1 , resulting in symmetric spectra for both the TE (black; ●) and TM (gray; ▲) modes. The TE spectra in C are for frequencies on the negative side (ν_- ; ●) and positive side (ν_+ ; ▲) of the ν_1 resonance. The TE spectra in D are taken at the band edge (ν_{BG} ; ●) and 60 GHz (ν_{BE} ; ▲) into the bandgap. The asymmetry of the line shapes in C and D implies a large ratio of coherent to dissipative interactions.

relative to the free space atomic transition frequency ν_{D1} . We observe little change of signal during the 5-ms probing time, suggesting that the atom number is approximately constant over this interval. The band edge of the PCW is tuned thermally by shining an external laser onto a corner of the chip, where its light is absorbed by the Si substrate. Hence, the Cs D₁ line can be aligned to be either outside or inside the bandgap with an uncertainty $\delta\nu \simeq 5$ GHz. The transmission for each data point is normalized by the transmission with no atoms ($|t_0 E_p|^2$), resulting in a measurement of $T/T_0 \equiv |t/t_0|^2$. The logarithm of the measured and simulated transmission spectra with no atoms $T_0 = |t_0(\nu_p)|^2$ is shown in Fig. 3A.

Examples of transmission spectra with atoms are shown in Fig. 3 B–D. Note that the spectra are shifted 12.5 MHz because of both the alternating current (AC) Stark shift of the dipole trap and the modified Lamb shift induced by the non-GMs of the PCW. Notably, the transmission spectra at the first cavity resonance ν_1 exhibit a characteristic Lorentzian “dip,” and they become more asymmetric as the frequency moves into the bandgap.

Transmission Model

We have developed a model to extract quantitative values for collective decay rates and frequency shifts from these atomic transmission spectra (39). Although the formalism of waveguide (40) and CQED (41) is well-suited for describing atoms coupled to uniform waveguides and cavities, it is not general enough to capture the rich physics of atomic interactions in the vicinity of a PCW. Instead, we describe our system by using a spin model in terms of the classical electromagnetic Green’s function, in which the atoms (or “pseudospins” for ground and excited states) interact through the emission and reabsorption of guided photons (42–44).

The electromagnetic Green’s tensor $\mathbf{G}(\mathbf{r}, \mathbf{r}_i, \omega)$ is related to the electric field $\mathbf{E}(\mathbf{r}, \omega)$ emitted by a dipole \mathbf{p}_i oscillating at frequency ω at position \mathbf{r}_i by $\mathbf{E}(\mathbf{r}, \omega) = \mu_0 \omega^2 \mathbf{G}(\mathbf{r}, \mathbf{r}_i, \omega) \cdot \mathbf{p}_i$ (43, 45). The dipole moment operator for atom i is decomposed into $\hat{\mathbf{p}}_i = \mathbf{d}_i \hat{\sigma}_{ge}^i + \mathbf{d}_i^* \hat{\sigma}_{eg}^i$, where \mathbf{d}_i is the dipole matrix element and $\hat{\sigma}_{ge}^i = |\mathbf{g}\rangle \langle \mathbf{e}|$ is the atomic coherence operator between the ground and excited states. The spin model describes a system of N atoms coupled to and driven by a GM of the PCW. In the low-saturation and steady-state regime, expectation values for the atomic coherences ($\sigma_{ge}^i = \langle \hat{\sigma}_{ge}^i \rangle$) are described by a linear system of equations (39) (SI Text):

$$\left(\tilde{\Delta}_A + i \frac{\Gamma'}{2} \right) \sigma_{ge}^i + \sum_{j=1}^N g_{ij} \sigma_{ge}^j = -\Omega_i, \quad [1]$$

where $\tilde{\Delta}_A = 2\pi\Delta_A = 2\pi(\nu_p - \nu_{D1})$ is the detuning between the probe and the atomic angular frequencies, Ω_i is the classical drive (Rabi frequency) for the i th atom due to the GM input field, and $g_{ij} = J_{1D}^{ij} + i\Gamma_{1D}^{ij}/2$, where $J_{1D}^{ij} = \mu_0 \omega_p^2 / \hbar \mathbf{d}_i^* \cdot \mathbf{R} \mathbf{E}(\mathbf{r}_i, \mathbf{r}_j, \omega_p) \cdot \mathbf{d}_j$ and $\Gamma_{1D}^{ij} = 2\mu_0 \omega_p^2 / \hbar \mathbf{d}_i^* \cdot \text{Im } \mathbf{G}(\mathbf{r}_i, \mathbf{r}_j, \omega_p) \cdot \mathbf{d}_j$. Each atom can also decay into non-GMs, including free space, with a decay rate Γ' . The appearance of the real and imaginary parts of the Green’s function in the coherent and dissipative terms has the classical analog that the in-phase and out-of-phase components of a field with respect to an oscillating dipole store time-averaged energy and perform time-averaged work, respectively. Because the first term in Eq. 1 is diagonal, the atomic coherences can be understood in terms of the eigenvalues $\{\lambda_\xi\}$ for $\xi = \{1, \dots, N\}$ and the eigenfunctions of the matrix \mathbf{g} , which has elements that are g_{ij} ; the real and imaginary parts of $\{\lambda_\xi\}$ correspond to frequency shifts and GM decay rates, respectively, of the collective atomic mode ξ .

The transmission spectrum can be expressed in terms of the eigenvalues of \mathbf{g} as (39) (SI Text)

$$\frac{t(\tilde{\Delta}_A, N)}{t_0(\tilde{\Delta}_A)} = \prod_{\xi=1}^N \left(\frac{\tilde{\Delta}_A + i\Gamma'/2}{\tilde{\Delta}_A + i\Gamma'/2 + \lambda_\xi} \right), \quad [2]$$

where $t_0(\tilde{\Delta}_A)$ is the transmission without atoms. In the case of a single atom i , the only eigenvalue is proportional to the self-Green’s function, $\lambda_\xi = g_{ii}$, which implies that the transmission spectrum is a direct measurement of the self-Green’s function at the atom’s position. For noninteracting atoms, the off-diagonal elements of \mathbf{g} are zero, and thus, the eigenvalues are single-atom quantities, $\lambda_\xi = g_{ii}$, because there is no cooperative response.

In contrast, for interacting atoms, the off-diagonal elements are nonnegligible, and there is a cooperative response. In particular, for the atomic frequency inside the bandgap of a photonic crystal, the elements g_{ij} are well-approximated by (28)

$$g_{ij} = \left(J_{1D} + \frac{i\Gamma_{1D}}{2} \right) \cos\left(\frac{\pi x_i}{a}\right) \cos\left(\frac{\pi x_j}{a}\right) e^{-\kappa_x |x_i - x_j|}, \quad [3]$$

where the cosine factors arise from the Bloch mode, and the decay length $1/\kappa_x$ is caused by the exponential decay of the field and results in a finite range of interaction. For an infinite photonic crystal, $\Gamma_{1D} = 0$, because the light is localized, and there is no dissipation through the GM. However, for a finite PCW of length L , the GM dissipation $\Gamma_{1D} \sim e^{-\kappa_x L}$ is finite because of leakage of the mode out of the edges of the structure.

In the limit where the interaction range $1/\kappa_x$ is much larger than the separation $\delta x_{ij} = |x_i - x_j|$ of the atoms, $\kappa_x \delta x_{ij} \lesssim \kappa_x \Delta x_A \ll 1$, the GM input field couples predominantly to a single collective “bright” mode of the system with eigenvalue $\lambda_B = \sum_{i=1}^N g_{ii} = \sum_{i=1}^N (J_{1D}^{ii} + i\Gamma_{1D}^{ii}/2)$. Formally, when $\kappa_x = 0$, the matrix \mathbf{g} is separable [$g_{ij} = u_i u_j$ with $u_i \propto \cos(\pi x_i/a)$] and therefore, only has one nonzero eigenvalue. In this single bright mode approximation, the transmission spectrum is given by

$$\frac{t(\tilde{\Delta}_A, N)}{t_0(\tilde{\Delta}_A)} = \frac{\tilde{\Delta}_A + i\Gamma'/2}{\left(\tilde{\Delta}_A + \sum_{i=1}^N J_{1D}^{ii} \right) + i \left(\Gamma' + \sum_{i=1}^N \Gamma_{1D}^{ii} \right) / 2}. \quad [4]$$

We have confirmed numerically that this single bright mode picture is valid within the limits of our uncertainties for the range of frequencies of the measured spectra in Fig. 3. In particular, at the largest detuning into the bandgap $\Delta_{BE} = 60$ GHz, we have $\kappa_x \Delta x_A \simeq 0.2$. However, for atomic frequencies farther away from the band edge, this approximation eventually breaks down (e.g., at the bandgap center, $\kappa_x \Delta x_A \simeq 1.5$).

The single bright mode approximation is also valid in conventional CQED. The Green’s function matrix is then given by $g_{ij} = (J_{1D} + i\Gamma_{1D}/2) \cos(k_c x_i) \cos(k_c x_j)$, where k_c is the wavevector of the standing wave cavity. In this case, $J_{1D} \propto \Delta_c / (1 + \Delta_c^2 / \gamma_c^2)$ and $\Gamma_{1D} \propto \gamma_c / (1 + \Delta_c^2 / \gamma_c^2)$, where Δ_c is the detuning from the cavity resonance and γ_c is the cavity linewidth. Importantly, the ratio of the imaginary dissipative coupling rate to the real coherent coupling rate falls off with inverse detuning, $R_{\text{CQED}} = \Gamma_{1D} / J_{1D} = \gamma_c / \Delta_c$ for large Δ_c , whereas in a PCW bandgap, the fall off is exponential with detuning from the band edge.

Analysis of Measured Spectra

Eq. 4 provides a direct mapping between the observed transmission spectra in Fig. 3 B–D and the electromagnetic Green’s function of the PCW. In particular, the line shape is Lorentzian for purely dissipative dynamics ($J_{1D}^{ii} = 0$). This line shape is precisely what occurs at the frequency of the first cavity mode ν_1 , as shown in Fig. 3B. When the GM band edge frequency is moved toward the atomic resonance ν_{D1} , the dispersive interactions are switched on, and the transmission line shape becomes asymmetric, displaying

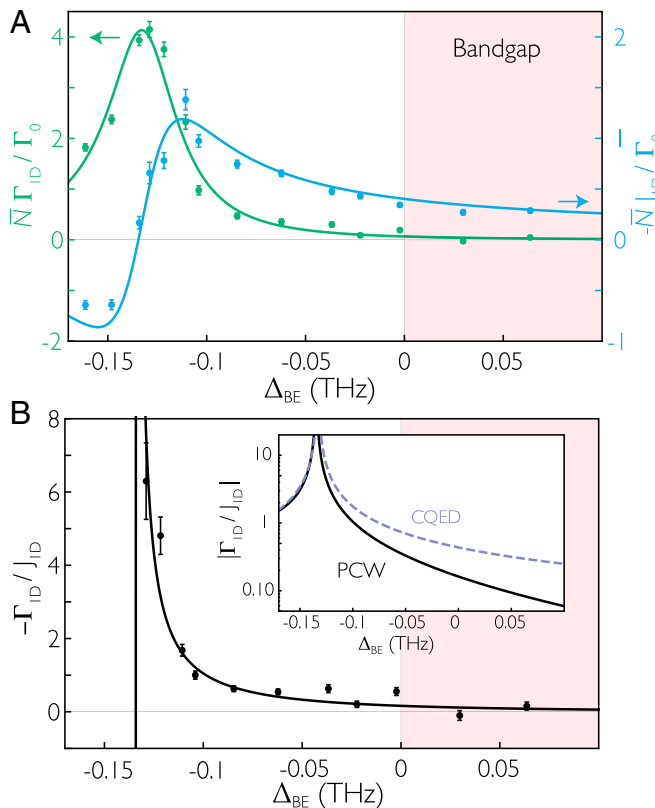


Fig. 4. (A) Peak dissipative interaction rate $\bar{N}\Gamma_{1D}$ (green) and coherent rate $\bar{N}J_{1D}$ (blue) around the band edge. With \bar{N} determined from independent decay rate measurements, the values for Γ_{1D} , J_{1D} are found from fits of the transmission model in Eq. 4 to the measured atomic spectra and normalized by the free space decay rate $\Gamma_0 = 2\pi \times 4.56$ MHz for the Cs D_1 line. The lines are the predictions from a numerical model based on 1D transfer matrices. (B) The measured and calculated ratios $\mathcal{R} = \Gamma_{1D}/J_{1D}$. The average of the two points in the bandgap gives a ratio of the dissipative to coherent coupling rate $\mathcal{R} = 0.05 \pm 0.17$. *B*, Inset is a comparison of \mathcal{R} for the PCW calculation (solid line) and CQED model (dashed line). From the measured linewidth of the first cavity resonance, $\gamma_c = 60 \pm 8$ GHz, CQED predicts that $\mathcal{R}_{\text{CQED}} = \gamma_c/\Delta_c$, where $\Delta_c = (\nu_p - \nu_1)$. Note that $-J_{1D}$ is plotted to more readily compare Γ_{1D} and J_{1D} as the band edge is approached.

a Fano-like resonance (46), which can be observed in Fig. 3 C and D. The appearance of an asymmetry in the atomic spectra directly reveals a significant coherent coupling rate J_{1D} , which is evident for frequencies that are in the bandgap region.

For all relevant frequencies, the spectra for the TM GM are approximately symmetric, since $J_{1D}^{\text{TM}} \ll \Gamma_{1D}^{\text{TM}} \ll \Gamma'$ for this GM polarization. An example of a TM spectrum is shown as the gray curve in Fig. 3B. Because the TM bandgap is so far detuned, the TM spectra are insensitive to Δ_{BE} and serve as a calibration signal. Using a waveguide transmission model, we fit the TM transmission spectra and extract a TM GM decay rate of $\Gamma_{1D}^{\text{TM}} = (0.045 \pm .01) \Gamma_0$. This rate is ~ 30 times smaller than the TE GM decay rate Γ_{1D} at the first resonance ν_1 . The ratio $\Gamma_{1D}^{\text{TE}}/\Gamma_{1D}^{\text{TM}} \approx 30$ is explained well by the expected slow-light and cavity enhancement of the PCW described in ref. 21 and *SI Text*. From the TM fits, we also measure $\Gamma' = 2\pi \times 9.1$ MHz, which because of inhomogeneous broadening, is larger than the value $\Gamma' = 2\pi \times 5.0$ MHz predicted from FDTD numerical calculations (*SI Text*). While tuning the band edge to move the atomic frequency ν_{D1} into the bandgap, TM spectra are measured to confirm *in situ* that the average atom number is approximately constant over the course of the measurements of TE spectra.

To obtain quantitative values for the collective frequency shifts and decay rates by fitting the TE atomic spectra to the spin model, we must account for the fluctuations in atom number and position along the x axis. As depicted in Figs. 1A and 2C, trapped atoms are approximately free to move along the axis of the device (*SI Text*). Their coupling rates are thus modulated by the fast oscillation of the Bloch function, which near the band edge, is approximately given by Eq. 3, $\Gamma_{1D}^{\text{II}}(x_i) = \Gamma_{1D} \cos^2(x_i\pi/a)$, and $J_{1D}^{\text{II}}(x_i) = J_{1D} \cos^2(x_i\pi/a)$. Here, Γ_{1D} and J_{1D} are the peak values. Furthermore, although we know the average atom number $\bar{N} = 3.0 \pm 0.5$ atoms from independent decay rate measurements (*SI Text*), the atom number for each experiment follows an unknown distribution. To model the experimental transmission spectra, such as in Fig. 3, we average the expression in Eq. 4 over the atom positions $\{x_i\}$ along the Bloch function and assume a Poisson distribution $P_{\bar{N}}(N)$ for the atom number N . We extract peak values Γ_{1D} and J_{1D} and plot the resulting cooperative rates $\bar{N}\Gamma_{1D}$ and $\bar{N}J_{1D}$ in Fig. 4A. In particular, at the first resonance ν_1 , the fitted single-atom GM decay rate is $\Gamma_{1D} = (1.4 \pm 0.2) \Gamma_0$, which is in good agreement with the decay time measurements $\Gamma_{1D} = (1.5 \pm 0.2) \Gamma_0$. More generally, we find good agreement between our measurements and our model for the transmission, as shown in Fig. 3.

The ratio $\mathcal{R} = \Gamma_{1D}/J_{1D}$ is shown in Fig. 4B. Because of the evanescent nature of the field in the bandgap, \mathcal{R} decays exponentially with increasing detuning into the bandgap, $\mathcal{R} \sim e^{-\kappa_x L}$, where $\kappa_x \propto \sqrt{\Delta_{BE}}$ (28). As displayed in Fig. 4B, *Inset*, the ratio between the GM decay rate Γ_{1D} to the GM frequency shift J_{1D} diminishes much faster than would be the case in traditional settings, such as CQED, for which $\mathcal{R}_{\text{CQED}} = \gamma_c/\Delta_c$, where γ_c is the cavity linewidth and Δ_c is the detuning from the cavity resonance. Indeed, by performing an average of the last two measured frequencies in the bandgap, we obtain $\mathcal{R} = 0.05 \pm 0.17$, whereas $\mathcal{R}_{\text{CQED}} = 0.30 \pm 0.04$, where we have taken the cavity linewidth to be a value consistent with the linewidth of the first cavity mode of the PCW ($\gamma_c = 60 \pm 8$ GHz). We can then infer that the ratio of dispersive to dissipative rates for GM atom–atom interactions (i.e., $1/\mathcal{R}$) is significantly larger than is the case in conventional optical physics (e.g., CQED).

Beyond the detailed modeling involving Eq. 4 averaged over fluctuations in atom number and position, we also fit the spectra with a generic transmission model with no averaging, as shown in *SI Text*. We find that the effective values for the GM decay rate and frequency shift are related to $\bar{N}\Gamma_{1D}$ and $\bar{N}J_{1D}$ in Fig. 4A by a simple scale factor related to the averaging of the Bloch function $\cos^2(\pi x/a)$.

Despite favorable scaling between the collective frequency shifts and the GM decay rates, there is still one obstacle to overcome toward purely dispersive atomic interactions, namely atomic emission into non-GMs (characterized by Γ'). For this PCW structure, the FDTD-simulated value of this decay rate is $\Gamma' \simeq 1.1 \Gamma_0$ (21) for the relevant frequencies of our experiment. Fortunately, it has been shown that suitable engineering of a wide variety of nanophotonic structures can lead to significant reductions in Γ'/Γ_0 (47). For example, ref. 1 reviews possibilities to achieve $\Gamma' \simeq 0.1\Gamma_0$.

Concluding Remarks and Outlook

In conclusion, we report the initial observation of cooperative atom interactions in the bandgap of a PCW. By tuning the band edge frequency of the PCW, we are able to modify the interactions between the atoms that are trapped close to the device, reducing the dissipative relative to coherent coupling for frequencies inside the bandgap of the PCW. Equipped with a theoretical model based on the electromagnetic Green's function of the alligator PCW, we infer quantitative values for the collective frequency shifts and decay rates experienced by the atoms. Moreover, we infer a suppression of the dissipative interactions with respect to the coherent ones several times larger than is customarily obtained in atomic physics. This measurement provides the first stepping stone toward the realization of quantum many-body physics in bandgap systems.

Moreover, near-term extensions of our experiment open the door to exploring new physical scenarios by using atoms coupled to PCWs. By trapping the atoms at the center of the device with GMs (47), we expect a sixfold increase to both coupling strengths J_{1D} and Γ_{1D} relative to Γ' . Moreover, by probing the atoms with the Cs D₂ line tuned to the upper band edge, where the intensity at the position of the atoms is larger, we expect a further improvement by a factor of two. Combining these two effects, we expect a significant enhancement of interactions through GMs compared with conventional free space interactions, namely $J_{1D}, \Gamma_{1D} > 10 \times \Gamma'$. This improvement could enable investigations of new paradigms for atom-photon interactions (28, 29, 36), including the recently proposed multiphoton dressed states (26, 27).

Note. After the submission of this manuscript, ref. 48 reported measurements of transmission spectra for a superconducting qubit placed within the bandgap of a microwave photonic crystal.

1. Lodahl P, Mahmoodian S, Stobbe S (2015) Interfacing single photons and single quantum dots with photonic nanostructures. *Rev Mod Phys* 87(2):347.

2. Kimble HJ (2008) The quantum internet. *Nature* 453(7198):1023–1030.

3. Vuckovic J, Yamamoto Y (2003) Photonic crystal microcavities for cavity quantum electrodynamics with a single quantum dot. *Appl Phys Lett* 82(15):2374–2376.

4. Yoshie T, et al. (2004) Vacuum Rabi splitting with a single quantum dot in a photonic crystal nanocavity. *Nature* 432(7014):200–203.

5. Aoki T, et al. (2006) Observation of strong coupling between one atom and a monolithic microresonator. *Nature* 443(7112):671–674.

6. Hennessy K, et al. (2007) Quantum nature of a strongly coupled single quantum dot-cavity system. *Nature* 445(7130):896–899.

7. Thompson JD, et al. (2013) Coupling a single trapped atom to a nanoscale optical cavity. *Science* 340(6137):1202–1205.

8. Bajcsy M, et al. (2009) Efficient all-optical switching using slow light within a hollow fiber. *Phys Rev Lett* 102(20):203902.

9. Balykin VI, Hakuta K, Kien FL, Liang JQ, Morinaga M (2004) Atom trapping and guiding with a subwavelength-diameter optical fiber. *Phys Rev A* 70(1):011401.

10. Londero P, Venkataraman V, Bhagwat AR, Slepnev AD, Gaeta AL (2009) Ultralow-power four-wave mixing with Rb in a hollow-core photonic band-gap fiber. *Phys Rev Lett* 103(4):043602.

11. Vetsch E, et al. (2010) Optical interface created by laser-cooled atoms trapped in the evanescent field surrounding an optical nanofiber. *Phys Rev Lett* 104(20):203603.

12. Goban A, et al. (2012) Demonstration of a state-insensitive, compensated nanofiber trap. *Phys Rev Lett* 109(3):033603.

13. Sørensen HL, et al. (2016) Coherent backscattering of light off one-dimensional atomic strings. arXiv:1601.04869.

14. Chang DE, Sørensen AS, Demler EA, Lukin MD (2007) A single-photon transistor using nanoscale surface plasmons. *Nat Phys* 3(11):807–812.

15. Akimov AV, et al. (2007) Generation of single optical plasmons in metallic nanowires coupled to quantum dots. *Nature* 450(7168):402–406.

16. Huck A, Kumar S, Shakoor A, Andersen UL (2011) Controlled coupling of a single nitrogen-vacancy center to a silver nanowire. *Phys Rev Lett* 106(9):096801.

17. Wallraff A, et al. (2004) Strong coupling of a single photon to a superconducting qubit using circuit quantum electrodynamics. *Nature* 431(7005):162–167.

18. van Loo AF, et al. (2013) Photon-mediated interactions between distant artificial atoms. *Science* 342(6165):1494–1496.

19. Devoret MH, Schoelkopf RJ (2013) Superconducting circuits for quantum information: An outlook. *Science* 339(6124):1169–1174.

20. Joannopoulos JD, Meade RD, Winn JN (1995) *Photonic Crystals: Molding the Flow of Light* (Princeton Univ Press, Singapore).

21. Goban A, et al. (2015) Superradiance for atoms trapped along a photonic crystal waveguide. *Phys Rev Lett* 115(6):063601.

22. Yablonovitch E (1987) Inhibited spontaneous emission in solid-state physics and electronics. *Phys Rev Lett* 58(20):2059–2062.

23. John S (1987) Strong localization of photons in certain disordered dielectric superlattices. *Phys Rev Lett* 58(23):2486–2489.

24. John S, Wang J (1990) Quantum electrodynamics near a photonic band gap: Photon bound states and dressed atoms. *Phys Rev Lett* 64(20):2418–2421.

25. Kurizki G (1990) Two-atom resonant radiative coupling in photonic band structures. *Phys Rev A* 42(5):2915–2924.

26. Shi T, Wu YH, Gonzalez-Tudela A, Cirac JI (2016) Bound states in boson impurity models. *Phys Rev X* 6(2):021027.

27. Calajó G, Ciccarello F, Chang DE, Rabl P (2016) Atom-field dressed states in slow-light waveguide QED. *Phys Rev A* 93(3):033833.

28. Douglas JS, et al. (2015) Quantum many-body models with cold atoms coupled to photonic crystals. *Nat Photonics* 9(5):326–331.

29. González-Tudela A, Hung CL, Chang DE, Cirac JI, Kimble HJ (2015) Subwavelength vacuum lattices and atom-atom interactions in two-dimensional photonic crystals. *Nat Photonics* 9(5):320–325.

30. Hartmann MJ, Brandao FGSL, Plenio MB (2006) Strongly interacting polaritons in coupled arrays of cavities. *Nat Phys* 2(12):849–855.

31. Greentree AD, Tahan C, Cole JH, Hollenberg LCL (2006) Quantum phase transitions of light. *Nat Commun* 2(12):856–861.

32. Goban A, et al. (2014) Atom-light interactions in photonic crystals. *Nat Commun* 5:3808.

33. Yu SP, et al. (2014) Nanowire photonic crystal waveguides for single-atom trapping and strong light-matter interactions. *Appl Phys Lett* 104(11):111103.

34. Lund-Hansen T, et al. (2008) Experimental realization of highly efficient broadband coupling of single quantum dots to a photonic crystal waveguide. *Phys Rev Lett* 101(11):113903.

35. Young AB, et al. (2015) Polarization engineering in photonic crystal waveguides for spin-photon entanglers. *Phys Rev Lett* 115(15):153901.

36. Hung CL, González-Tudela A, Cirac JI, Kimble HJ (2016) Quantum spin dynamics with pairwise-tunable, long-range interactions. *Proc Natl Acad Sci USA* 113(34):E4946–E4955.

37. Lumerical Solutions, Inc. (2015) Version 8.12. <http://www.lumerical.com/tcad-products/fdtd/>.

38. COMSOL Inc. (2009) COMSOL Multiphysics (COMSOL AB, Stockholm), Version 3.5a.

39. Asenjo-Garcia A, Hood JD, Chang DE, Kimble HJ (2016) Atom-light interactions in quasi-1D dielectrics: A Green's function perspective. arXiv:1606.04977.

40. Shen JT, Fan S (2005) Coherent photon transport from spontaneous emission in one-dimensional waveguides. *Opt Lett* 30(15):2001–2003.

41. Gardiner CW, Collett MJ (1985) Input and output in damped quantum systems: Quantum stochastic differential equations and the master equation. *Phys Rev A Gen Phys* 31(6):3761–3774.

42. Dung HT, Knöll L, Welsch DG (2002) Resonant dipole-dipole interaction in the presence of dispersing and absorbing surroundings. *Phys Rev A* 66(6):063810.

43. Buhmann SY, Welsch DG (2007) Dispersion forces in macroscopic quantum electrodynamics. *Prog Quantum Electron* 31(2):51–130.

44. Dzotjan D, Sørensen AS, Fleischhauer M (2010) Quantum emitters coupled to surface plasmons of a nanowire: A Green's function approach. *Phys Rev B* 82(7):075427.

45. Novotny L, Hecht B (2006) *Principles of Nano-Optics* (Cambridge Univ Press, New York).

46. Fano U (1961) Effects of configuration interaction on intensities and phase shifts. *Phys Rev* 124(6):1866–1878.

47. Hung CL, Meenehan SM, Chang DE, Painter O, Kimble HJ (2013) Trapped atoms in one-dimensional photonic crystals. *New J Phys* 15(8):083026.

48. Liu Y, Houck AA (August 1, 2016) Quantum electrodynamics near a photonic band gap. *Nat Phys*, 10.1038/nphys3834.

49. Tuchendler C, Lance AM, Browaeys A, Sortais YRP, Grangier P (2008) Energy distribution and cooling of a single atom in an optical tweezer. *Phys Rev A* 78(3):033425.

ACKNOWLEDGMENTS. We acknowledge the contributions of O. J. Painter and his group, including for fabrication and clean room facilities. We also acknowledge A. Burgers, C.-L. Hung, J. Laurat, M. J. Martin, A. C. McClung, J. A. Muniz, and L. Peng. Funding was provided by National Science Foundation (NSF) Grant PHY 1205729; by the Air Force Office of Scientific Research Multidisciplinary University Research Initiative (MURI) for Quantum Memories in Photon-Atomic Solid-State Systems (QuMPASS); by the Institute for Quantum Information and Matter (IQIM), NSF Physics Frontiers Center with support of the Moore Foundation; by the Office of Naval Research (ONR) Award N00014-16-1-2399; by the ONR MURI for Quantum Opto-Mechanics with Atoms and Nanostructured Diamond (QOMAND); and by the Department of Defense National Security Science and Engineering Faculty Fellowship (NSSEFF) Program. A.G. was supported by the Nakajima Foundation. A.A.-G. and M.L. were supported by the IQIM Postdoctoral Fellowship. A.A.-G. also acknowledges support from Global Marie Curie Fellowship LANTERN 655701. S.-P.Y. acknowledges support from the International Fulbright Science and Technology Award. D.E.C. acknowledges support from Fundacio Privada Cellex Barcelona, Marie Curie CIG ATOMNANO, MINECO Severo Ochoa Grant SEV-2015-0522, and ERC Starting Grant FoQAL.

Supporting Information

Hood et al. 10.1073/pnas.1603788113

SI Text

In our results in the main text, we measure collective frequency shifts and decay rates for atoms trapped near a PCW. In our previous work in ref. 21, we trapped multiple atoms in an optical dipole force trap above the PCW. We operated with the atomic frequency outside the bandgap in a regime with large decay rate Γ_{1D} and small coherent coupling rate J_{1D} . By varying the density and observing the superradiant decay of the atoms $\Gamma_{tot}^{(N)} = \Gamma_{SR}(\bar{N}) + \Gamma_{1D} + \Gamma'$, we inferred the single-atom GM decay rate Γ_{1D} and the average number of atoms \bar{N} . Importantly, this measured single-atom decay rate Γ_{1D} agreed well with the FDTD simulations at the calculated trap location. This good agreement is in part because of the nanometer-scale accuracy in which the alligator PCWs are fabricated, which is required for both the band edge alignment and the device quality.

In our paper, the band edge of the PCW is tuned around the resonance frequency of the atoms, and we observe the dominance of the GM-coherent coupling rates J_{1D} over the dissipative coupling rates Γ_{1D} , which is associated with atomic radiative processes for operation within the bandgap. To extract quantitative values for these parameters from our measurements of transmission spectra for atoms trapped along a PCW, we have developed theoretical techniques based on Green's functions for the PCW, which are new to atomic physics. As in ref. 21, the average number of atoms \bar{N} is measured by way of transient decay. Our principal finding relates to the turning off of the GM decay rate Γ_{1D} , which in the bandgap, is predicted to be exponentially suppressed, while nonetheless, retaining appreciable coherent processes described by J_{1D} .

For the spectra in our paper, the transmission through the device decreases exponentially in the bandgap, and more time is required to measure the transmission spectra compared with our work in ref. 21. Unfortunately, Cs slowly coats the PCW during the measurement, both degrading the device quality and shifting the band edge out of the thermal tuning range. As a result, each device only has a limited lifetime for making transmission measurements. For our experiment, we first repeated superradiance measurements outside the bandgap at the first resonance ν_1 of the PCW to determine the average number of atoms \bar{N} and the single-atom GM decay rate Γ_{1D} and show that the atoms behave as a collective emitter. Then, with an average number of $\bar{N} \simeq 3$, we measured transmission spectra as the atomic frequency is shifted into the bandgap. We simultaneously measured the TM spectra to verify that the atom number is constant over the course of the measurements of the TE spectra.

1. Alligator PCW Design and Fabrication. The schematic of the device is shown in Fig. S1A. Light is coupled into and out of the device by mode-matching the output of an optical fiber to that of a terminated rectangular-shaped waveguide on both sides of the device (33). The fibers are glued permanently in etched v grooves at optimized coupling positions. The design and fabrication of the alligator PCW are detailed in ref. 33. The PCW is fabricated on a 200- μm Si chip coated with a 200-nm-thick SiN film. The SiN device is suspended across a 2-mm-wide window after the Si substrate beneath it is removed, as shown in the image in Fig. S1B. The window allows optical access for the trapping and cooling of atoms around the device.

The dielectric TE mode band edge (ν_{BE}) is aligned to within 200 GHz of the Cs D₁ line ($\nu_{D1} = 335.12$ THz) by a low-power inductively coupled reactive ion CF₄ etch. The directional etch thins the SiN layer at a rate of 3 nm/min until a transmission measurement confirms alignment of the band edge. The final geometric dimensions of the device used in the text are given in Fig. S1C.

For the experiment, the chip is placed at the center of an ultrahigh vacuum chamber, and the optical fibers exit through Teflon fiber feedthroughs. We measure the transmission through a device using a superluminescent diode as the source and an optical spectrum analyzer as the detector. The measured transmission and reflection spectra are shown in Fig. S2A. The transmission spectra near the lower (dielectric) and upper (air) band edges are compared with an FDTD simulation in Fig. S2 B and C.

2. Alligator Dispersion Relation from Scattering Images. Here, we describe the analysis performed for the PCW dispersion relations in Fig. 2E. We send a single-frequency laser beam through the device and image the scattered light with a microscope. We integrate the image over the width of the PCW to produce a single plot of intensity vs. position. Then, we scan the laser frequency around the lower band edge to produce a 2D plot of scattered intensity as a function of position x along the device and frequency ν of the input light.

The weak scattered light comes from small fabrication imperfections or intrinsic material defects and serves as a probe of the local intensity. Because each scatterer emits light at a different rate, we have to normalize the scattered light by a reference intensity spectrum in which the intensity of the device is known. For this reference spectrum, we average over the intensities for frequencies far from the band edge, where the PCW behaves like a waveguide and the local intensity in the device is approximately constant. The normalized data are shown in Fig. S3, and a zoomed-in version is in Fig. 2A.

In the FDTD simulation described above, we calculate the intensity along the center of the device for frequencies around the band edge. Taking the maximum intensity in each unit cell and normalizing by the intensity in the waveguide regime, we produce Fig. 2B.

Next, we fit the intensity spectrum at a given frequency to a model to extract the wavevector for that frequency. Near the band edge, the field in an infinite PCW is well-approximated by $E(x) \propto \cos(\chi\pi/a)e^{i\delta k_x x}$, where $\delta k_x = \pi/a - k_x$ in the propagating band ($\Delta_{BE} < 0$) and $\delta k_x = ik_x$ inside the bandgap ($\Delta_{BE} > 0$). The edges of a finite photonic crystal reflect with R_t because of a large group index mismatch between the waveguide section and the PCW. The resonances of the weak cavity result in the cavity-like intensity profiles seen at frequencies $\nu_{1,2,3,4,5}$ in Fig. S3. The intensity at a point x along a finite photonic crystal of length L is well-approximated by a model based on the intensity in a cavity with two mirrors of reflectivity R_t :

$$|E(x)|^2 = I_1 |e^{i\delta k_x x} - R_t e^{2i\delta k_x L} e^{-i\delta k_x x}|^2, \quad [S1]$$

where I_1 is related to the overall intensity. This expression ignores the fast oscillations of the Bloch function, which go as $\cos^2(\chi\pi/a)$. Note that in the bandgap (when $\kappa_x L \gg 1$), the intensity model reduces to an exponential decay: $|E(x)|^2 \approx I_1 e^{-2\kappa_x x}$. Interestingly, at the band edge ($\delta k_x \rightarrow 0$ and $R_t \rightarrow 1$), the intensity displays a quadratic dependence on the position: $|E(x)|^2 \propto (L - x)^2$.

For each frequency, we fit the intensity along the nominal cells with Eq. S1 and extract δk_x . This procedure allows us to map out the dispersion relation $\delta k_x(\Delta_{BE})$, which we show in Fig. 2E for the measured and simulated data. From the simulated fits, we find that the effective length of the cavity is 162 cells, which is slightly longer than the 150 nominal cells and is expected due to the leakage of the cavity field into the tapering sections. We use this length for the fits of the measured data. Examples of the measured and simulated intensities are shown in Fig. S4. The fluctuation of the intensity, even after the normalization, is most likely caused by the spatial profile of Bloch mode. The normalization

trace is taken by averaging data for excitation frequencies farther away from the band edge where the Bloch mode contrast is reduced, whereas the data closer to the band edge have a large Bloch mode fringe visibility. However, the fluctuations do not affect the statistical fits at the level of accuracy required for the dispersion relation in this work.

The frequency for which $\delta k_x = 0$ is defined as the band edge frequency ν_{BE} . To extract this frequency and the curvature of the dispersion relation near the band edge, we fit the measured and simulated dispersion relations with a dispersion model (21),

$$\delta k_x(\nu) = \frac{2\pi}{a} \sqrt{\frac{(\nu_{\text{BE}2} - \nu)(\nu_{\text{BE}} - \nu)}{4\zeta^2 - (\nu_{\text{BE}2} - \nu_{\text{BE}})^2}}, \quad [\text{S2}]$$

where ν_{BE} ($\nu_{\text{BE}2}$) is the lower (upper) band edge frequency, and ζ is a frequency related to the curvature of the band near the band edge. From the measured data fits, the distance between the first resonance and band edge is $\nu_{\text{BE}} - \nu_1 = 133 \pm 9$ GHz and $\zeta = 227 \pm 3$ THz. The simulated data give $\nu_{\text{BE}} - \nu_1 = 135.0$ GHz, and the curvature parameter is $\zeta = 226.0$ THz. These values are in good agreement with the dispersion relation from the eigenmode simulation of the infinite PCW in Fig. 1C, which gives $\zeta = 229.1$ THz.

3. SI Trap. In Fig. S5A, we show a schematic of the SI trap. The SI beam is nearly perpendicular to the axis of the device, has a 50-μm diameter, and has a polarization aligned to the axis of the device (Fig. S5A). The orange areas in Fig. S5A represent the approximate localization of the atoms along x, y . By time of flight measurements of atoms in the dipole trap, we estimate an atomic temperature of ~ 30 μK. From the beam waist and atom temperature, we can infer that the atoms are localized to $2\Delta x_A = 12$ μm along the x axis.

Simulations of the SI trap potential are shown in Fig. S5 B–D. The simulations are performed for the infinite structure with COMSOL. The trap depth is calibrated with the 12-MHz AC Stark shift measured from the atomic spectra. Fig. S5B shows the trap potential in the y – z plane. Atoms that are significantly hotter than ~ 100 μK are expected to crash into the device along the diagonal directions because of Casimir–Polder forces. Fig. S5C shows the trapping potential along the z axis. Atoms are trapped at $z = 240$ nm. Fig. S5D shows the trap along the x axis. Because of the photonic crystal, the trap modulates by ~ 10 μK along the x axis, which is significantly smaller than the estimated trap temperature.

In addition to the results in Fig. S5, we have also carried out numerical modeling of the optical trap using Lumerical simulations (37) of the actual finite length PCW and tapers shown in Fig. S1. We have as well included Casimir–Polder potentials as in ref. 47. More details of the trap are discussed in ref. 21.

4. Transmission Model and Atomic Spectra Fits. Here, we give a more detailed description of the transmission model in the text, which follows the derivation given in ref. 39. A system of N atoms coupled to a radiation field can be described using formalism based on the classical Green's function (42, 43). In the Markovian limit, the field can be eliminated to obtain a master equation that describes the interactions between the atoms: $\dot{\hat{\rho}}_A = -i/\hbar[H, \hat{\rho}_A] + \mathcal{L}[\hat{\rho}_A]$. Here, the Hamiltonian H gives the coherent evolution of the system:

$$H = -\hbar \sum_{j=1}^N \tilde{\Delta}_A \hat{\sigma}_{ee}^j - \hbar \sum_{j,i=1}^N J_{1\text{D}}^{ji} \hat{\sigma}_{eg}^j \hat{\sigma}_{ge}^i - \hbar \sum_{j=1}^N \left(\Omega_j \hat{\sigma}_{eg}^j + \Omega_j^* \hat{\sigma}_{ge}^j \right), \quad [\text{S3}]$$

and the Lindblad operator $\mathcal{L}[\hat{\rho}_A]$ gives the dissipation of the system:

$$\begin{aligned} \mathcal{L}[\hat{\rho}_A] = & \sum_{j,i=1}^N \frac{\Gamma' \delta_{ji} + \Gamma_{1\text{D}}^{ji}}{2} \\ & \times (2\hat{\sigma}_{ge}^j \hat{\rho}_A \hat{\sigma}_{eg}^i - \hat{\sigma}_{eg}^j \hat{\sigma}_{ge}^i - \hat{\rho}_A \hat{\sigma}_{eg}^j \hat{\sigma}_{ge}^i). \end{aligned} \quad [\text{S4}]$$

The Hamiltonian and the Lindblad are expressed in terms of the atomic coherence operator $\hat{\sigma}_{ge}^j = |g\rangle\langle e|$ between the ground and excited states of atom j . The Hamiltonian contains terms for the free-atom evolution, the coherent atom–atom interactions, and the classical drive, respectively; $\tilde{\Delta}_A = 2\pi\Delta_A = 2\pi(\nu_p - \nu_{\text{D}1})$ is the detuning between the probe and the atomic angular frequencies, and Ω_j is the Rabi frequency for atom j caused by the GM field. The atom–atom spin exchange rate $J_{1\text{D}}^{ji}$ is expressed in terms of the real part of the GM Green's function as

$$J_{1\text{D}}^{ji} = \left(\frac{\mu_0 \omega_p^2}{\hbar} \right) \mathbf{d}_j^* \cdot \text{Re } \mathbf{G}(\mathbf{r}_j, \mathbf{r}_i, \omega_p) \cdot \mathbf{d}_i, \quad [\text{S5}]$$

where $\omega_p = 2\pi\nu_p$, and \mathbf{d}_j is the dipole matrix element of atom j . The Lindblad term is responsible for the dissipative interactions in the system, which include atomic decay into non-GMs (Γ') and GMs ($\Gamma_{1\text{D}}^{ji}$). The decay rate into the GM is written in terms of the imaginary part of the Green's function as

$$\Gamma_{1\text{D}}^{ji} = 2 \left(\frac{\mu_0 \omega_p^2}{\hbar} \right) \mathbf{d}_j^* \cdot \text{Im } \mathbf{G}(\mathbf{r}_j, \mathbf{r}_i, \omega_p) \cdot \mathbf{d}_i. \quad [\text{S6}]$$

For low atomic density along the PCW, the nonguided emission rate Γ' is not cooperative and is described here as a single-atom effect, with δ_{ji} as the Kronecker delta.

In the low saturation regime, the Heisenberg equations for the expectation value of the atomic coherences ($\langle \hat{\sigma}_{eg} \rangle = \sigma_{eg}$) can be solved for with the master equation leading to

$$\dot{\sigma}_{ge}^j = i \left(\tilde{\Delta}_A + i \frac{\Gamma'}{2} \right) \sigma_{ge}^j + i \Omega_j + i \sum_{i=1}^N g_{ji} \sigma_{ge}^i, \quad [\text{S7}]$$

where the complex coupling rate is

$$g_{ij} = J_{1\text{D}}^{ij} + \frac{i\Gamma_{1\text{D}}^{ij}}{2} = \left(\frac{\mu_0 \omega_p^2}{\hbar} \right) \mathbf{d}_i^* \cdot \mathbf{G}(\mathbf{r}_i, \mathbf{r}_j, \omega_p) \cdot \mathbf{d}_j, \quad [\text{S8}]$$

which is the Green's function between atoms i and j projected onto the respective dipole matrix elements. In the steady-state solution, the time derivative is set to zero, and the result is the linear system of equations for the atomic coherences given in the text.

The electric field in the system can be expressed in terms of the input probe field $\mathbf{E}^+(\mathbf{r}, \omega_p)$ and solutions for the atomic coherences (39):

$$\mathbf{E}^+(\mathbf{r}, \omega_p) = \mathbf{E}_p^+(\mathbf{r}, \omega_p) + \mu_0 \omega_p^2 \sum_{j=1}^N \mathbf{G}(\mathbf{r}, \mathbf{r}_j, \omega_p) \cdot \mathbf{d}_j \sigma_{ge}^j. \quad [\text{S9}]$$

An expression for the transmission through a quasi-1D structure can be derived by solving the steady-state system of equations in Eq. S7 for the atomic coherences σ_{ge}^j and substituting them into Eq. S9. The expression can then be simplified in the case where the dipole moments are real, in which case \mathbf{g} is a complex symmetric matrix with eigenvectors and eigenvalues $\mathbf{g} \mathbf{u}_\xi = \lambda_\xi \mathbf{u}_\xi$, and where the Green's function is well-represented by a 1D Green's function. The final result is (37)

$$\frac{t(\tilde{\Delta}_A, N)}{t_0(\tilde{\Delta}_A)} = \prod_{\xi=1}^N \left(\frac{\tilde{\Delta}_A + i\Gamma'/2}{\tilde{\Delta}_A + i\Gamma'/2 + \lambda_\xi} \right), \quad [\text{S10}]$$

where $t_0(\tilde{\Delta}_A)$ is the transmission without atoms.

In the bandgap, the matrix \mathbf{g} of elements g_{ij} is well-approximated by

$$g_{ij} = \left(J_{1D} + \frac{i\Gamma_{1D}}{2} \right) \cos\left(\frac{\pi x_i}{a}\right) \cos\left(\frac{\pi x_j}{a}\right) e^{-\kappa_x |x_i - x_j|}. \quad [\text{S11}]$$

As discussed in the text, when the interaction range $1/\kappa_x$ is much larger than the separation distance ($\kappa_x |x_i - x_j| \ll 1$), there is only a single atomic bright mode for which the frequency shift and GM decay rate are given by $\sum_{i=1}^N J_{1D}^i$ and $\sum_{i=1}^N \Gamma_{1D}^i$. The transmission spectrum for N atoms in the single bright mode approximation is given by

$$T(\Delta_A, N) = T_0(\Delta_A) \left| \frac{\tilde{\Delta}_A + i\Gamma'/2}{\tilde{\Delta}_A + i\Gamma'/2 + \sum_i (J_{1D}^i + i\Gamma_{1D}^i/2)} \right|^2, \quad [\text{S12}]$$

where $\tilde{\Delta}_A = 2\pi\Delta_A = 2\pi(\nu_p - \nu_{D1})$ is the detuning between the pump and the atomic frequency, and $T_0(\Delta_A)$ is the device transmission when no atoms are present.

Explicitly accounting for the atoms' positions by substituting Eq. S11 into Eq. S12, we find that the transmission is given by

$$T(\Delta_A, N; x_1, \dots, x_N) / T_0(\Delta_A) = \left| \frac{\Delta'_A + i\Gamma'/2}{\Delta'_A + i\Gamma'/2 + \sum_{j=1}^N (J_{1D} + i\Gamma_{1D}/2) \cos^2\left(\frac{x_j \pi}{a}\right)} \right|^2. \quad [\text{S13}]$$

We have defined $\Delta'_A \equiv \tilde{\Delta}_A + \Delta_0$ to account for the AC Stark shift Δ_0 of the atoms because of the dipole trap.

To accurately model the experimental conditions, we average the transmission model over atom positions and atom number. During a single measurement, the atoms are free to move along the length of the device over the range $2\Delta x_A$ as in Fig. S5A, evenly sampling the Bloch function. We let $\langle T(\Delta_A, N; x_1, \dots, x_N) \rangle_x$ be an average over all positions, that is,

$$\langle T(\Delta_A, N; x_1, \dots, x_N) \rangle_x = T_0(\Delta_A) \int_0^a dx_1 \dots dx_N \left| \frac{\Delta'_A + i\Gamma'/2}{\Delta'_A + i\Gamma'/2 + \sum_{j=1}^N (J_{1D} + i\Gamma_{1D}/2) \cos^2\left(\frac{x_j \pi}{a}\right)} \right|^2.$$

We repeat the measurement multiple times for each frequency Δ_A . Each experiment can have a different number of atoms, and therefore, we average the transmission expression over a Poisson distribution $P_{\bar{N}}(N)$, which is a function of the average atom number \bar{N} . The transmission model averaged over both atom positions and atom numbers is given by

$$\begin{aligned} \langle T(\Delta_A, N; x_1, \dots, x_N) \rangle_{x,N} &= T_0(\Delta_A) \sum_N P_{\bar{N}}(N) \langle T(\Delta_A, N; x_1, \dots, x_N) \rangle_x. \end{aligned} \quad [\text{S14}]$$

This expression is the final form of the transmission model that we use to fit the atomic spectra.

Assuming $\bar{N} = 3.0$, which is obtained from the atom decay rate measurement, we fit the TE atomic spectra with Eq. S14 and extract Γ_{1D} , J_{1D} , Γ' , and Δ_0 for each frequency. We show the values of Γ_{1D} and J_{1D} in Fig. 4A. We show the AC Stark shift and nonguided decay rate in Fig. S6.

The average of the nonguided decay rate Γ' for the TE data outside the bandgap is $\Gamma' = 2\pi \times 9.1$ MHz, which is significantly larger than the expected value from the FDTD simulation, $\Gamma' = 2\pi \times 5.0$ MHz. This additional inhomogeneous broadening could be caused by finite temperature of the trapped atoms, vector shifts from circular light in the SI beam, atom density-dependent collisional broadening, stray magnetic fields, and electric fields from charges in the dielectric. We estimate the contributions individually and find that they likely do not explain the extraneous broadening. We note that the estimate of temperature of trapped atoms could be improved in the future (49), and it may help shed light on our excess broadening.

Interestingly, the fitted Γ' increases in the bandgap and is as high as $\Gamma' = 2\pi \times 16$ MHz for the last measured point. One possible explanation is that this is because of the breakdown of the single bright mode approximation, because coupling to multiple collective atomic modes should result in a broadened linewidth. Another possibility is that, because there is a large extinction of the TE mode in the bandgap, there might be some mixing between the TE and TM modes.

We also measure transmission spectra for the TM mode, which have band edges that are far-detuned from the Cs transitions. The transmission in this waveguide regime is described by an optical depth (OD) model

$$\frac{T}{T_0} = \exp \left[\frac{-\text{OD}}{1 + \left(\frac{2\Delta'_A}{\Gamma_{1D}^{\text{TM}} + \Gamma'} \right)^2} \right], \quad [\text{S15}]$$

where the resonant OD is given by $\text{OD} = 2\bar{N}\Gamma_{1D}^{\text{TM}}/\tilde{\Gamma}'$. We fit the TM spectra with this model and extract Γ' , Δ_0 , and Γ_{1D}^{TM} (assuming $\bar{N} = 3$). The values of Γ' and Δ_0 are shown with the TE data in Fig. S6. The averaged Γ_{1D}^{TM} value is $0.044 \Gamma_0$, which is ~ 30 times smaller than Γ_{1D} for the TE mode at the first resonance ν_1 and clearly shows the enhanced interaction because of the PCW.

5. Simple Transmission Model. In the text, we fit atomic transmission spectra with the averaged transmission model from Eq. S14 to extract the peak GM decay rate Γ_{1D} and frequency shift J_{1D} . In this section, we fit the spectra with a transmission model that involves no averaging, and we extract an effective decay rate Γ_{1D}^{eff} and frequency shift J_{1D}^{eff} , which will be smaller than the corresponding peak values because of the averaging of the $\cos^2(\pi x/a)$ Bloch function as the atoms move along the x axis of the trap. In the single bright mode approximation discussed in the text, the transmission for a single collective mode with total decay rate A and frequency shift B is given by

$$\frac{T(\Delta_A)}{T_0(\Delta_A)} = \left| \frac{\Delta'_A + i\Gamma'/2}{\Delta'_A + B + i(\Gamma' + A)/2} \right|^2. \quad [\text{S16}]$$

Here, the detuning Δ'_A includes the AC Stark shift $\Delta'_A = \Delta_A + \Delta_0$. Because the average number of atoms $\bar{N} \approx 3$ is measured independently in a decay rate measurement, the collective rates A and B are related to the effective rates by $A = \bar{N}\Gamma_{1D}^{\text{eff}}$ and $B = \bar{N}J_{1D}^{\text{eff}}$. Examples of the fitted spectra for atoms outside and inside the band gap are shown in Fig. S7. The translucent lines in Fig. S7 are the expected signals for average atom numbers of $\bar{N} = 1$ and $\bar{N} = 9$.

The fitted values of A and B are plotted for each detuning from the band edge Δ_{BE} in Fig. S8A. The results are qualitatively similar to the corresponding plot in Fig. 4A, except that the effective rates $A = \bar{N}\Gamma_{\text{1D}}^{\text{eff}}$ and $B = \bar{N}\Gamma_{\text{1D}}^{\text{eff}}$ are scaled down by $\eta = 0.42$ because of the modulation of the Bloch function $\cos^2(\pi x/a)$. The solid lines in Fig. S8A are the same theoretical curves as in Fig. 4A, except that they are scaled by $\eta = 0.42$.

The ratio of $A/B = \Gamma_{\text{1D}}^{\text{eff}}/\Gamma_{\text{1D}}$ is plotted in Fig. S8B. Because the scale factors η cancel, the result is in good agreement with the corresponding plot of $\mathcal{R} = \Gamma_{\text{1D}}/J_{\text{1D}}$ in Fig. 4B. The black theory curve in Fig. S8B is the same as in Fig. 4B. Whereas the peak decay rate and frequency shift are sensitive to the specific model, the ratio of dissipative to coherent coupling is mostly model insensitive.

6. Atom Decay Measurement. We exploit the superradiance of atoms trapped near the alligator PCW to determine the mean atom number \bar{N} and the peak atom decay rate Γ_{1D} (at ν_1) into the GMs.

As established in ref. 21, the total exponential decay rate of the atoms is $\bar{\Gamma}_{\text{tot}}(N) = \bar{\Gamma}_{\text{SR}}(N) + \bar{\Gamma}_{\text{tot}}^{(1)}$, where $\bar{\Gamma}_{\text{SR}}$ is the \bar{N} -dependent superradiance decay rate, and $\bar{\Gamma}_{\text{tot}}^{(1)}$ is the observed single-atom decay rate. We note that, when $\bar{N} \ll 1$, $\bar{\Gamma}_{\text{tot}} \sim \bar{\Gamma}_{\text{tot}}^{(1)} = \bar{\Gamma}_{\text{1D}} + \Gamma'$, because only the single-atom decay rates $\bar{\Gamma}_{\text{1D}}$ into the GM and Γ' into the environment remain; Γ' is numerically calculated to be $2\pi \times 5.0$ MHz for the Cs D₁ line at the trapping site near the PCW (21).

We excite the atoms with a weak resonant light pulse through the GM, whereas the first resonance ν_1 near the band edge is aligned with the Cs D₁ line. Pulse properties are as in ref. 21. The subsequent fluorescence decay rates $\bar{\Gamma}_{\text{tot}}$ are determined through exponential fits. By varying the trap holding time t_{m} after loading, the mean atom numbers for the decay measurements are varied. The decay rates are empirically fitted in an exponential form as a function of holding time t_{m} (21) : $\bar{\Gamma}_{\text{tot}}(t_{\text{m}}) = \bar{\Gamma}_{\text{SR}} e^{-t_{\text{m}}/\tau_{\text{SR}}} + \bar{\Gamma}_{\text{tot}}^{(1)}$, as shown in Fig. S9. From the fitted asymptotic value of the decay

rates, we deduce that the apparent single-atom decay rate is $\bar{\Gamma}_{\text{1D}} = (1.12 \pm 0.14)\Gamma'$.

Because the atoms are randomly distributed along the x direction in the trap, the observed decay curves are results after spatially averaging the coupling rates $\Gamma_{\text{1D}}(x)$. Assuming a uniform distribution of N atoms around the center of the PCW, a more detailed model specifies the form of fluorescence intensity decay as (21)

$$\mathcal{I}_N(t) = \gamma^2 e^{-(N\gamma + \Gamma')t} \cdot I_0(\gamma t)^{N-2} \cdot \left[\frac{N(N+1)}{4} I_0(\gamma t)^2 - \left(\frac{N}{4\gamma t} + \frac{N^2}{2} \right) I_0(\gamma t) I_1(\gamma t) + \frac{N(N-1)}{4} I_1(\gamma t)^2 \right], \quad [\text{S17}]$$

where $\gamma = \bar{\Gamma}_{\text{1D}}/2$, and I_k is the modified Bessel function. Numerically simulating the decay of single atoms in the trap by using $\mathcal{I}_1(t)$, we compare between the exponentially fitted value $\bar{\Gamma}_{\text{1D}}$ and the value of Γ_{1D} used for $\mathcal{I}_1(t)$, which yields a ratio of $\bar{\Gamma}_{\text{1D}}/\Gamma_{\text{1D}} = 0.81$. This ratio is consistent with the ratio of 0.8 ± 0.3 from measurement at long hold time $t_{\text{m}} = 94$ ms, when single-atom decay predominates (shown as the asymptote in Fig. S9). Based on the values of $\bar{\Gamma}_{\text{1D}}$ deduced above, we conclude that $\Gamma_{\text{1D}} = (1.4 \pm 0.2)\Gamma'$.

At early holding times, the atom number N noticeably fluctuates around some mean values $\bar{N} \gtrsim 1$. To capture this \bar{N} -dependent variation, we fit the decay curves by averaging $\mathcal{I}_N(t)$ with weight function of Poisson distribution probability $P_{\bar{N}}(N)$ (21). The fitting parameter here is \bar{N} , whereas we fix the value of Γ_{1D} in Eq. S17. The fit is consistent with $\bar{N} = 3.0 \pm 0.5$ at $t_{\text{m}} = 4$ ms when we carry out the transmission spectra measurement. Based on the trap lifetime $\tau = 30$ ms, we further deduce that $\bar{N} \sim 0.1$ at $t_{\text{m}} = 94$ ms.

The linear \bar{N} dependence of superradiance is given by $\bar{\Gamma}_{\text{SR}} = \eta \cdot \bar{N} \cdot \Gamma_{\text{1D}}$, where $\eta = 0.36 \pm 0.06$ is some linear coefficient that has a value is consistent with that reported in ref. 21.

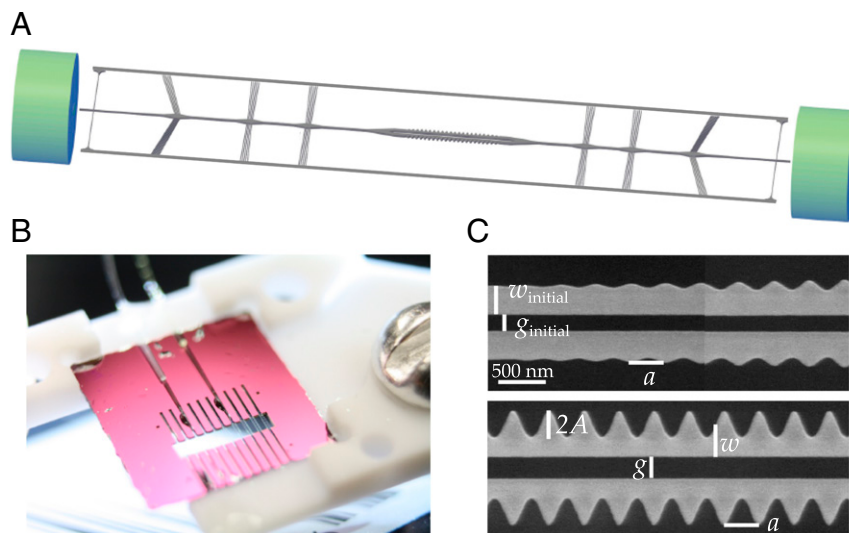


Fig. S1. Alligator PCW chip and device overview. (A) Schematic of the entire device. The alligator PCW is at the center. Optical fibers (green) on both ends couple light into and out of the waveguide. The waveguide is surrounded by supporting and cooling structures. (B) Image of a 10 × 10-mm PCW chip. Multiple waveguides stretch across the window of the chip, with the PCWs at the center of the window. The window provides optical access for trapping and cooling atoms around the device. Reproduced from ref. 33, with the permission of AIP Publishing. (C) Overview of device variables. The lattice constant for the entire device is $a = 370$ nm. The device dimensions are measured with an SEM and calibrated to the lattice constant. The device dimensions are $w = 310 \pm 10$ nm, $2A = 262 \pm 10$ nm, $g = 220 \pm 10$ nm, $w_{\text{initial}} = 268 \pm 15$ nm, and $g_{\text{initial}} = 165 \pm 10$ nm. The thickness of the SiN is 185 ± 5 nm. The index of refraction for Si_3N_4 is $n = 2.0$ around our frequencies of interest.

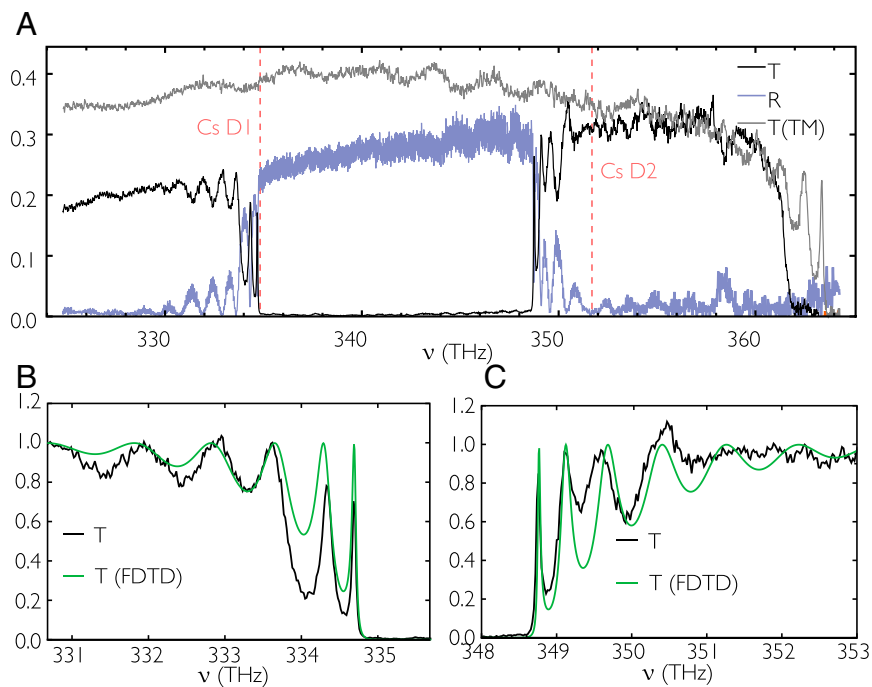


Fig. S2. Measured and simulated transmission and reflection spectra. (A) Transmission (black) and reflection (blue) spectra through the entire chip for the TE mode (polarization in the plane of the device). The red dashed lines are the Cs D₁ (335.1 THz) and D₂ (351.7 THz) lines. The TE transmission efficiency through the entire device near the dielectric band edge is $\sim 23\%$, indicating that the single-pass efficiency from the fiber to device is approximately 49%. Most of the loss is caused by the waveguide to fiber coupling section. The gray line is the TM transmission (polarization perpendicular to the plane of the device). Note that the lower band edge of the TM mode is visible at around 365 THz but far detuned from both Cs D_{1,2} transitions. (B and C) TE transmission data are normalized and compared with an FDTD simulation (37). The simulation uses the measured device parameters in Fig. S1 that are adjusted within the uncertainty of the measurements so that the positions of the first resonances match those in the measured spectra.

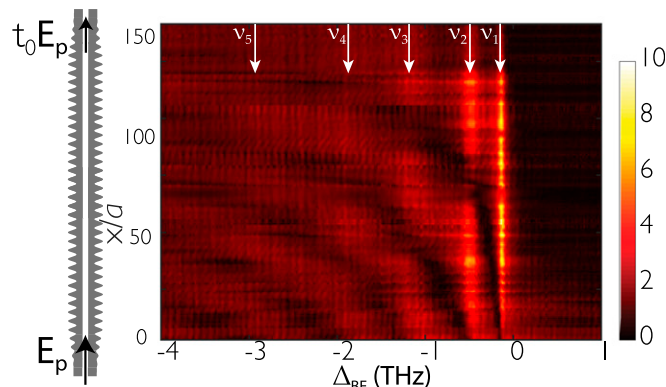


Fig. S3. Normalized magnitude of the scattered electric field of the PCW for frequencies $\Delta_{BE} = \nu_p - \nu_{BE}$ around the band edge. The schematic in Left shows the PCW with the number of unit cells reduced by five.

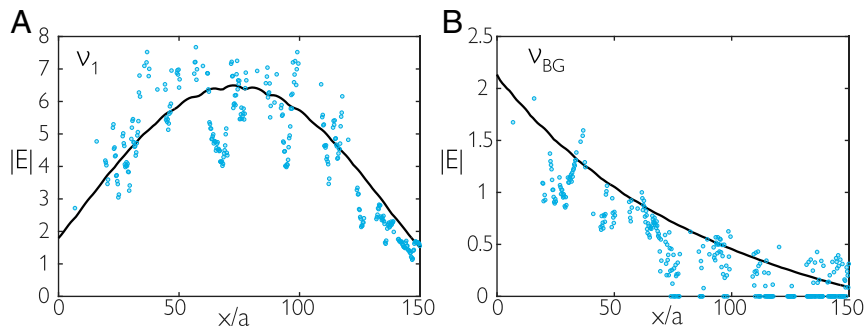


Fig. S4. The electric field magnitude in (A) the PCW at the first resonance ν_1 and (B) the bandgap $\nu_{BG} = \nu_{BE} + 60$ GHz. The points show measured data, and the black lines are from an FDTD simulation. The electric field magnitude $|E|$ is normalized by the electric field magnitude far from the band edge; thus, these plots give the enhancement of $|E|$ relative to the waveguide regime.

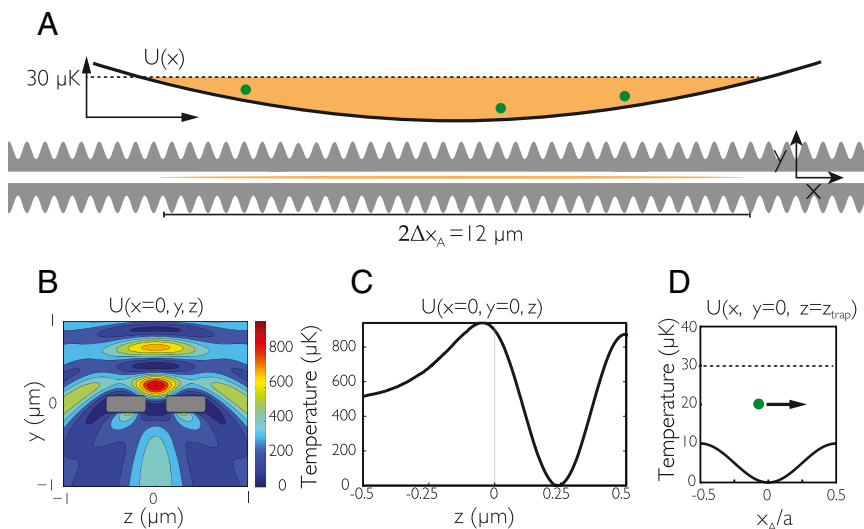


Fig. S5. (A) Schematic of the atoms in the SI trap. Given the estimated atom temperature of 30 μK , we infer that the atoms are confined to a length of $2\Delta x_A = 12$ μm along the x axis. (B–D) Far-off-resonance optical trap (FORT) potentials for the SI trap simulation (B) in the y – z plane (21), (C) along the z axis, and (D) along the x axis.

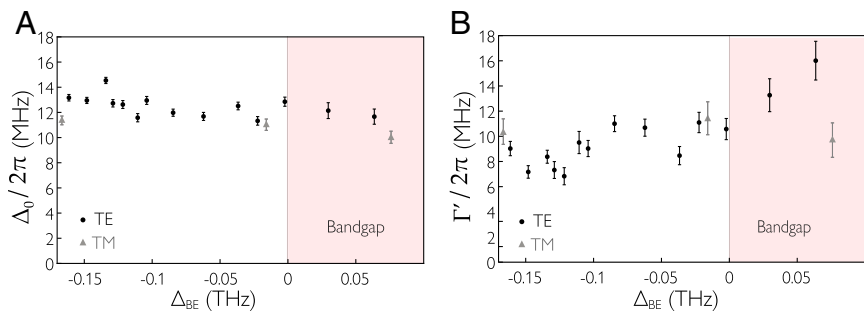


Fig. S6. Fitted values from the averaged transmission model for TE (black circles) and TM (gray triangles) spectra. (A) Fitted AC Stark shift Δ_0 . (B) Fitted Γ' .

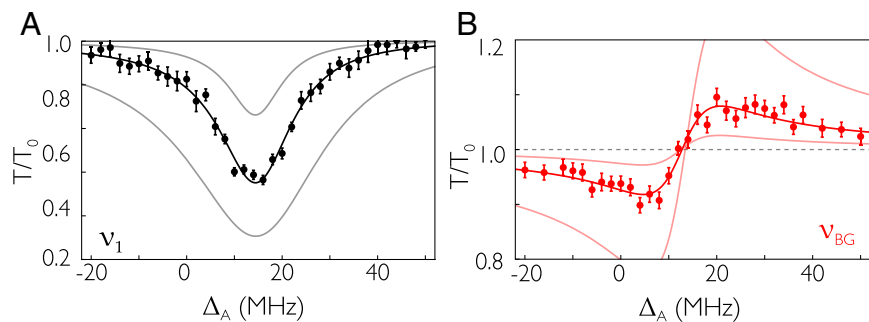


Fig. S7. Fits of transmission spectra with the model in Eq. S16 for when the atomic resonance frequency is aligned to (A) the first resonance and (B) in the bandgap. From the decay rate measurement, the average number of atoms is $\bar{N} \approx 3$ for the full (central) curves in A and B, while the translucent curves give the expected spectra for $\bar{N} = 1$ and $\bar{N} = 9$ atoms.

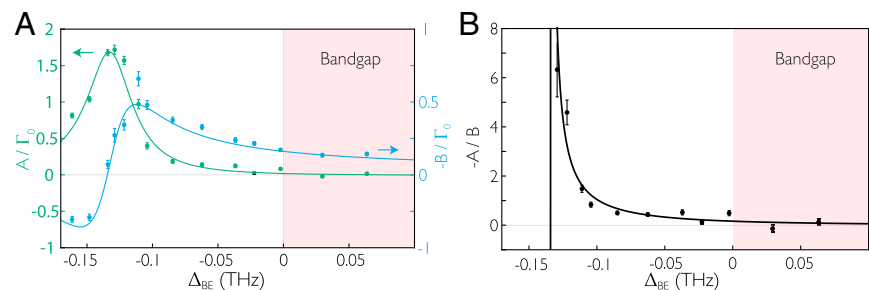


Fig. S8. (A) Fitted values for the effective collective decay rates A and frequency shifts B for various detunings from the band edge Δ_{BE} . The solid lines are the expected results for the peak values as in Fig. 4A, except scaled down by $\eta = 0.42$. (B) Ratio $A/B = \Gamma_{1D}^{\text{eff}}/\Gamma_{1D}^{\text{eff}}$ along with the theoretical prediction for the peak ratio Γ_{1D}/J_{1D} from Fig. 4B.

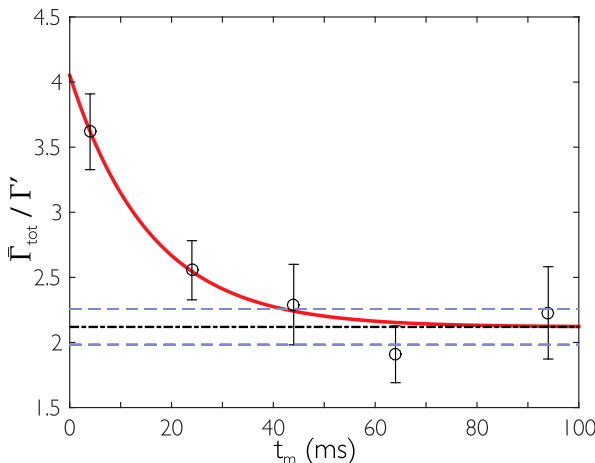


Fig. S9. Total decay rates as a function of holding time t_m . The red solid curve is the empirical fit, and the dash-dot line represents the fitted asymptotic total decay rate at very long times. The blue dashed lines specify fitted error boundaries. The fit yields $\tau_{SR} = 16$ ms, $\bar{\Gamma}_{SR} = 1.5\Gamma'$, and the asymptote $\bar{\Gamma}_{tot}/\Gamma' = 2.12 \pm 0.14$.